12-2015

Characterizing the Effective Bandwidth of Nonlinear Vibratory Energy Harvesters Possessing Multiple Stable Equilibria

Meghashyam Panyam Mohan Ram
Clemson University, mpanyam@g.clemson.edu

Characterizing the Effective Bandwidth of Nonlinear Vibratory Energy Harvesters Possessing Multiple Stable Equilibria

---

A Dissertation
Presented to
the Graduate School of
Clemson University

In Partial Fulfillment
of the Requirements for the Degree
Doctor of Philosophy
Mechanical Engineering

---

by
Meghashyam Panyam Mohan Ram
December 2015

Accepted by:
Dr. Mohammed F. Daqaq, Committee Chair
Dr. Ardalan Vahidi
Dr. Gang Li
Dr. Phanindra Tallapragada

Abstract

In the last few years, advances in micro-fabrication technologies have lead to the development of low-power electronic devices spanning critical fields related to sensing, data transmission, and medical implants. Unfortunately, effective utilization of these devices is currently hindered by their reliance on batteries. In many of these applications, batteries may not be a viable choice as they have a fixed storage capacity and need to be constantly replaced or recharged. In light of such challenges, several novel concepts for micro-power generation have been recently introduced to harness, otherwise, wasted ambient energy from the environment and maintain these low-power devices. Vibratory energy harvesting is one such concept which has received significant attention in recent years.

While linear vibratory energy harvesters have been well studied in the literature and their performance metrics have been established, recent research has focused on deliberate introduction of stiffness nonlinearities into the design of these devices. It has been shown that, nonlinear energy harvesters have a wider steady-state frequency bandwidth as compared to their linear counterparts, leading to the premise that they can used to improve performance, and decrease sensitivity to variations in the design and excitation parameters. This dissertation aims to investigate this premise by developing an analytical framework to study the influence of stiffness nonlinearities on the performance and effective bandwidth of nonlinear vibratory energy harvesters.

To achieve this goal, the dissertation is divided into three parts. The first part investigates the performance of bi-stable energy harvesters possessing a symmetric quartic potential energy function under harmonic excitations and carries out a detailed analysis to define their effective frequency bandwidth. The second part investigates the relative performance of mono- and bi-stable energy harvesters under optimal electric loading conditions. The third part investigates the response and performance of tri-stable energy harvesters possessing a symmetric hexic potential function under

harmonic excitations and provides a detailed analysis to approximate their effective frequency bandwidth. As a platform to achieve these objectives, a piezoelectric nonlinear energy harvester consisting of a uni-morph cantilever beam is considered. Stiffness nonlinearities are introduced into the harvesters design by applying a static magnetic field near the tip of the beam. Experimental studies performed on the proposed harvester are presented to validate some of the theoretical findings.

Since nonlinear energy harvesters exhibit complex and non-unique responses, it is demonstrated that a careful choice of the design parameters namely, the shape of the potential function and the electromechanical coupling is necessary to widen their effective frequency bandwidth. Specifically, it is shown that, decreasing the electromechanical coupling and/or designing the potential energy function to have shallow wells, widens the effective frequency bandwidth for a given excitation level. However, this comes at the expense of the output power which decreases under these design conditions. It is also shown that the ratio between the mechanical period and time constant of the harvesting circuit has negligible influence on the effective frequency bandwidth but has considerable effect on the associated magnitude of the output power.

Dedication

This dissertation is dedicated to God, my father, who now lives with Him, and to my mother, sister, and wife, with all my love and respect.

Acknowledgments

This work will not be complete without acknowledging the people who have been a constant source of encouragement, guidance, support and love.

Above all, I would like to express my deepest gratitude to my advisor, Dr. Mohammed Daqaq for his invaluable guidance, undying faith in me, and constant support without which this dissertation would not be possible. He is a gem of a person and I consider myself lucky to have a friend and mentor like him. I thank him for believing in me and patiently guiding me through the setbacks during the course of this research. His mentorship has instilled confidence in me and enabled me to improve personally and professionally.

I would like to extend my sincere gratitude to my committee members Dr. Ardalan Vahidi, Dr. Gang Li, and Dr. Phanindra Tallapragada for being accommodative and giving me constructive feedback. I would also like to thank the professors I have taken courses with: Dr. Imtiaz Haque, Dr. Mohammed Daqaq, Dr. Ardalan Vahidi, Dr. Beshah Ayalew, and Dr. Gang Li.

My sincere thanks to the staff members and technicians: Ms. Gwen Dockins, Mr. Jamie Cole, Mr. Michael Justice, Mr. Stephen Bass, and Mr. David Moline for their endless help which has played an important role in the completion of this work.

I extend special thanks to my colleagues and office mates: Dr. Ravindra Masana, Clodoaldo Silva, Dr. Amin Bibo, Saad Alazemi, Abdraouf Abusoua, Ali Alhadidi, Dr. Yousef Qaroush, Dr. James Gibert, Dr. Gregory Batt, Qifan He, Yuhao Wang, Raveen Kumar, Wen-an Jiang, and Yawen Xu for all the help and enjoyable discussions.

There are several friends who have made this journey an enjoyable one. I would like to thank Dr. Nitendra Nath, Dr. Parth Bhavsar, Dr. Sriram Venkatraman, Dr. Judhajit Roy, and several others for making my stay at Clemson a memorable one. Thanks to all my childhood friends for their constant support and help.

This work would be impossible without my family's love and support. I cannot express enough gratitude towards my brothers, Harsha and Dr. Vikram Munikoti, and my uncle and aunt, Vasanth and Padma Munikoti, for their constant support and love. Special thanks to my aunts Anu Visveswar, Saraswati, Sudha and Anitha for their encouragement and support. My sincere gratitude to my in-laws, Mr. Baburao, Mrs. Anuradha, and Ragavendra for their encouragement and blessings. I would also like to thank Mr. And Mrs. Praful Domadia for their encouragement and support.

I am truly blessed to have a mother like Mythily Mohan Ram and I would not be here if not for her unconditional love and support. I admire her for enduring several sacrifices to help me achieve my goals. I would not have contemplated taking up this endeavour if not for my sister, Manasi's support and love, or my brother-in-law Nagabhushan's encouragement.

Finally and most importantly, the one other person who has helped me see this work through to completion is my lovely wife, Swetha. Her support, encouragement, patience, and love have been a great source of strength for me.

Table of Contents

List of Tables

List of Figures

Chapter 1

Introduction

1.1 Motivations

Significant advances in electronics and related fields of technology has led to the development of low cost and low power-consumption electonic devices. Structural health monitoring sensors [9, 10], medical health monitoring devices such as pace makers [11], spinal stimulators [12], electric pain relievers [13], wireless sensors [14, 15, 16], and micro-electromechanical systems [17, 18] are a few examples among many other devices that can effectively function at power levels in the order of micro-watts. For instance, Wireless Integrated Network Sensor (WINS) systems used in radio communications, consist of distributed sensors and micro-controllers that have an average power consumption of about 300 μW [19]. A wireless transponder for data transmission is capable of operating efficiently with less than 1 mW of power [20, 21]. These devices and sensors, however, rely on batteries as their primary power source, which inhibits their effective usage and operation. Batteries are known to have a fixed storage capacity and low energy density [22]. Additionally, they need to be replaced or recharged which can be very expensive and cumbersome.

In light of such challenges, many research studies have focused on the development of scalable energy harvesters to power and maintain these devices. The primary objective of these devices is to scavenge, otherwise wasted ambient energy to produce enough electrical power to replace or recharge batteries in order to power sensors and systems deployed in remote and inaccessible locations.

Traditional sources of ambient energy such as solar, wind, thermal, etc., have been employed extensively for various applications [23, 24, 25, 26]. In addition to these common sources, vibrations

has recently flourished as a major source of energy for micro-power generation. Several novel devices and ideas have been developed to transform ambient vibrations directly into electricity [14, 27, 28].

Vibratory energy harvesters (VEHs) exploit the ability of active materials (e.g., piezoelectric and magnetostrictive) and electromechanical transduction mechanisms (e.g., electrostatic, and electromagnetic) to generate electric potential in response to external vibrations and/or mechanical stimuli [14, 27, 28, 29]. Vibratory energy harvesters are currently finding applications in different critical areas, especially in health monitoring of structures, vehicles, and machines. For instance, today, wireless health-monitoring sensor networks have become an integral part of systems deployed to predict and prevent catastrophic failure in different structures because of their cost effectiveness and efficiency [20]. These sensor networks require a constant source of power and it has been demonstrated that, energy harvested from vibrations caused by traffic flow over bridges, motion of trains, swaying of buildings among other mechanisms, is feasible to power such systems [30, 31, 32, 33]. With the critical advances in technologies pertaining to these sensor networks and other low-power consumption devices, there is an ever increasing need to design compact and scalable VEHs that can harvest minute amounts of energy to run and maintain them.

1.1.1 Vibratory Energy Harvesters: Basic Concept

The simplest and most commonly available VEH consists of a cantilever beam with piezoelectric patches attached near its clamped end as shown in Fig. 1.1. When subjected to external environmental excitations, $a_b(t)$, beam oscillations result in large strains near the clamped end, thereby straining the piezoelectric patches and producing a voltage, V, across an electric load which can be used to represent the device to be powered.

Figure 1.1: Schematic of a piezoelectric energy harvester.

In general, irrespective of the transduction mechanism, traditional VEHs including the one

shown in Fig. 1.1, have a critical drawback in their operating principle which limits their efficacy. Specifically, these devices operate based on the principle of linear resonance, which results in maximum energy transduction from the environment to the electric load in a narrow frequency bandwidth around their natural frequency. Any deviations in the excitation frequency away from the harvester's fundamental frequency cause the already small energy output to drop significantly, making the energy harvesting process highly inefficient.

The issue of frequency matching becomes even more pressing when one recognizes that most external excitation sources have broadband or time-dependent frequency characteristics. As such, most realistic excitation sources such as structural vibrations and swaying of buildings among others have their energy distributed over a wide spectrum of frequencies or their amplitude and frequency vary with time. Thus, tuning a linear VEH to an excitation frequency becomes challenging and usually yields very low energy transduction efficiency.

Several research studies have focused on modeling and analyzing VEHs in response to harmonic and random excitations in an attempt to improve their performance by maximizing the output power and more importantly, achieve large output power levels over a broader frequency range. Initial design approaches incorporated passive/active frequency tuning mechanisms in order to alter the fundamental frequency of the harvester to match the dominant frequency of excitation [34, 35, 36, 37]. However, it was demonstrated that, these tunable designs are not efficient under random or rapidly varying frequency inputs [34]. Additionally, harvesters with tuning mechanisms require external power or complex design means to function efficiently which outweighs their power harvesting ability.

More recently, deliberate introduction of stiffness nonlinearities into the design of VEHs has been a topic which received wide attention. Driven by the ability of the nonlinearity to extend the coupling between the harvester's response and the excitation to a wider range of frequencies, many research studies have demonstrated that nonlinearities can be used to decrease sensitivity to parameters' uncertainties and to enhance performance under random and non-stationary excitations commonly encountered in realistic environments [1, 3, 4, 5, 7, 38, 39, 40, 41, 42, 43, 44, 45, 46, 47, 48, 49]. The most common approach to the design of nonlinear VEHs is the introduction of a nonlinear restoring force usually by an external means, using, for example, magnetic or mechanical forces [2, 6, 50, 51]. Two classes of these nonlinear VEHs have been studied extensively. The first class of VEHs exhibit hardening/softening type nonlinear resonant behavior similar to a *mono-stable*

duffing oscillator. Such harvesters exhibit one stable equilibrium point also known as a node and their oscillations are confined to single global potential well as shown in Fig.1.2(a). If the associated restoring force increases with the displacement, it said to be of the hardening type. On the other hand, if it decreases with an increase in displacement, it is said to be of the softening type as depicted in Fig.1.2(b).

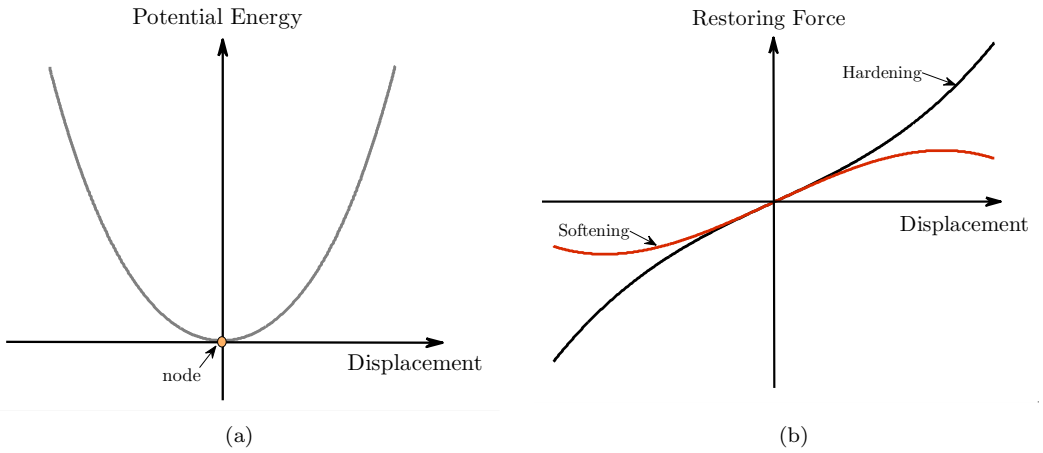

Figure 1.2: Potential energy function and restoring force of nonlinear mono-stable VEHs

For such devices, the nonlinearity can be introduced using several design means [1, 2, 9]. For instance, Barton et. al [1] proposed an electromagnetic mono-stable VEH with a tip magnet attached to the end of a cantilever beam, as shown in Fig. 1.3(a). The hardening type nonlinear restoring force is created by the magnetic potential between the magnets and a ferrous stator. When the beam is set into motion, the magnets move relative to the coil wound around an iron core generating a current as per Faraday's law. In another demonstration, Mann and Sims [2] proposed a magnetically-levitated inductive energy harvester similar to the one shown in Fig. 1.3(b). The harvester consists of a fluctuating central iron core that is levitated by two outer magnets. The nonlinearity is introduced in the form of the magnetic restoring force. Energy is generated when there is relative motion between the core and the coil. In a third demonstration of mono-stable VEHs, Masana and Daqaq [6] proposed an axially-loaded clamped-clamped beam type piezoelectric harvester. They showed that, when the axial load is below the critical buckling load, the harvester exhibits a mono-stable Duffing type behavior with a cubic nonlinearity whose magnitude and nature depends on the magnitude of the axial load.

The second class of nonlinear harvesters is designed to have a two-well potential energy

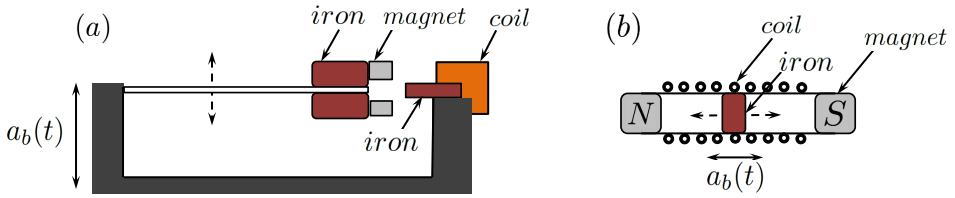

Figure 1.3: Schematics of a mono-stable energy harvesters. (a) Inductive energy harvester by Barton et. al [1], and (b) Inductive energy harvester proposed by Mann and Sims [2]

function and exhibits the response of a *bi-stable duffing oscillator*. In these devices, the nonlinearity produces a potential energy function with two minima (stable nodes) separated by a local maximum (unstable saddle) also known as a potential barrier as shown in Fig. 1.4(a). The depth and separation distance between these potential wells depend on the degree of nonlinearity. In this case, the restoring force increases with the displacement as shown in Fig.1.4(b).

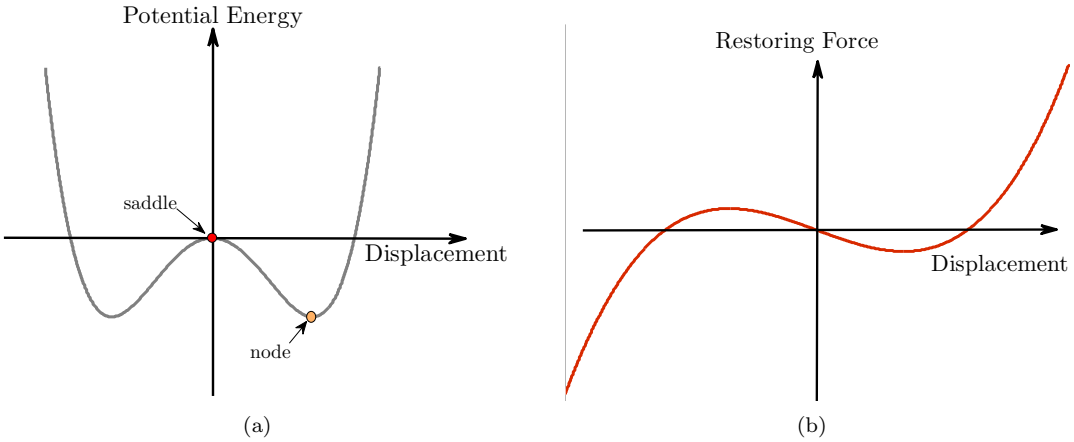

Figure 1.4: Potential energy function and restoring force of bi-stable VEHs

The concept of bi-stable VEHs was initally introduced by Cottone et. al [40] and later studied by several researchers [1, 3, 4, 5]. These initial designs were based on the bi-stable magneto-elastic structure by Moon and Holmes [52] and their main concept of operation is very similar. As shown in Fig. 1.5(a), the bi-stable harvester consists of piezoelectric cantilever beam with a ferroelectric tip oscillating between two magnets. For a certain separation distance between the two magnets, the system becomes bi-stable. More recently, Masana and Daqaq [6, 7] also proposed a bi-stable harvester which consisted of a clamped-clamped piezoelectric beam subjected to an axial load,

as shown in Fig. 1.5(b). When the axial load applied is larger than the critical buckling load of the beam, the harvester becomes bi-stable in nature. It has been shown that, under certain conditions in which the inter-well dynamics are activated, these types of harvesters can yield a broadband output power under harmonic excitations [3, 5, 7].

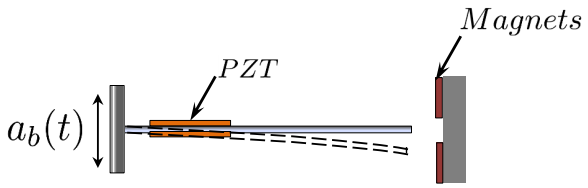

(a)

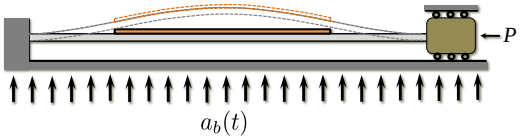

(b)

Figure 1.5: Schematic of bi-stable piezolectric energy harvesters using (a) Magnets as implemented in Ref. [1, 3, 4, 5] and (b) Axial load as implemented in Ref. [6, 7].

More recently, the concept of incorporating higher-order nonlinearities into the design of VEHs such that they possess a *tri-stable* potential energy function has been proposed [8, 53]. In their demonstration, Zhou et.al [8] propose a piezoelectric energy harvester which consists of a cantilever beam with a tip magnet oscillating between two stationary magnets as shown in Fig. 1.6(a). They show that, at a certain angular orientation and separation distance between the stationary magnets, the harvester possesses a tri-stable potential energy function with three minima that represent the stable equilibria (nodes) and two local maxima (saddles) as shown in Fig. 1.6(b). Through numerical simulations and preliminary experimental studies, they show that tristable VEHs produce higher broadband output voltages in the low frequency range as compared to their bi-stable counterparts.

1.2 Performance of Nonlinear Vibratory Energy Harvesters

In general, introduction of nonlinearities has been shown to improve the broadband output capabilities of energy harvesters and enhance their performance. Nonetheless, the complexity of the

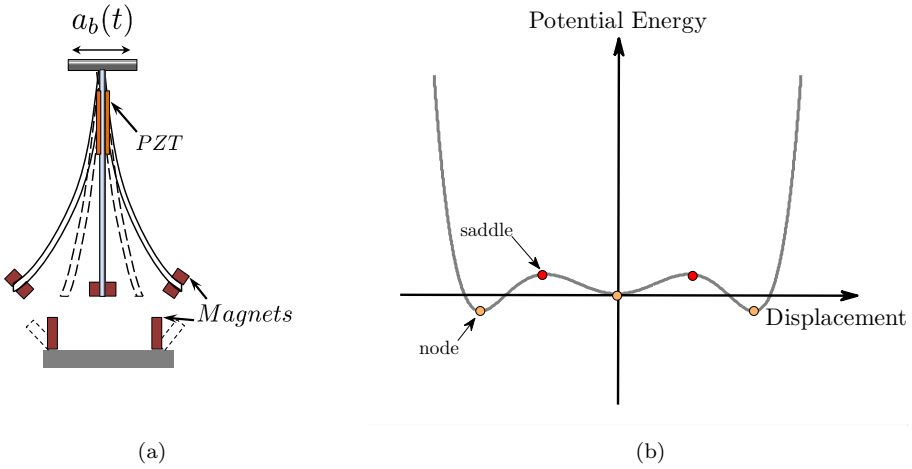

(a) (b)

Figure 1.6: (a) Schematic of a tri-stable VEH [8]. (b) Associated potential energy function.

response behavior of nonlinear VEHs as compared to their linear counterparts introduces additional challenges that complicates the full characterization of their response, thereby reducing our ability to reap their full benefits. Nonlinear VEHs have been shown to exhibit different behaviors that are not seen in linear systems including sub-harmonic, super-harmonic, quasi-periodic, and chaotic responses. They can also undergo different bifurcations in the parameter space which yield sudden jumps in the response amplitude and/or switching in its period (doubling/halving) [3, 4, 7, 40, 41, 42]. Mono-stable VEHs exhibit nonlinear (hardening/softening) hysteretic behavior and their performance depends primarily on the excitation level and type of nonlinearity. On the other hand, due to the presence of two or three potential wells, the performance of bi- and tri-stable VEHs is dependent on the excitation's level; if the excitation level is too small to activate the inter-well oscillations, the dynamics remain confined to one potential well producing small-amplitude responses that are not particularly favorable for energy harvesting. When the excitation is large enough to allow the desired large-amplitude inter-well oscillations, the harvester can perform complex non-unique dynamic responses including inter- and intra-well chaos as well as periodic responses at the excitation frequency or fraction integers of it [54].

Due to these complex responses, many researchers have pointed to the difficulty of not only achieving an optimal design of multi-stable VEHs [3, 55], but also comparing their relative performance to mono-stable ones [7]. Firstly, without prior knowledge of the intensity of the excitation source, the harvester potential can be designed to be too shallow for the multi-stability to be use-

ful or too deep for the dynamic trajectories to escape a single potential well [7]. Secondly, even when the potential function is properly designed for the excitation level, the large-orbit branch of inter-well periodic motion is not always unique and can be accompanied by a chaotic attractor and small branches of less desirable intra-well oscillations [5, 41, 49]. In fact, it has been demonstrated through numerical simulations that the bandwidth of frequencies where the desirable large-orbit branch of periodic solutions is unique has a complex dependence on the design parameters including the potential shape, the electromechanical coupling, the effective damping, and most importantly the level of excitation. This complex dependence cannot be resolved by depending solely on numerical simulations or sets of experimental data. Analytical and semi-analytical approaches[1] have been recently proposed by [60, 61, 62, 63] in an attempt to delineate this dependence. *However, there is a need to construct more accurate analytical tools to capture the qualitative variations in the dynamics and propose techniques to possibly expand this effective bandwidth.*

Many studies have characterized the response behavior of the mono- and bi-stable type of nonlinear VEHs separately, but very few of them have actually compared their performance relative to one another. In one study, Masana and Daqaq [7] compared the output voltage of clamped-clamped axially-loaded energy harvester in both configurations across an *arbitrarily* chosen electric load and found that the output voltage depends on the magnitude of base acceleration and the shape of the potential function. However, the choice of an arbitrary electric load in the comparative performance analysis of nonlinear VEHs can yield inaccurate conclusions regarding their output power. As such, it is essential to optimize the electric load in order to deduce accurate conclusions about the relative performance. Some studies have already addressed maximization of output power of VEHs by optimizing the electric load and/or the design parameters or by designing additional circuits [64, 65, 66, 67, 68]. For the most part, however, the models considered for the optimization problem are either linear, device specific, or do not draw a comparison of the relative power output of mono- and bi-stable VEHs. *As of today, there are no studies comparing the relative performance of nonlinear VEHs under optimal loading conditions.*

Despite novel ideas that have provided significant performance enhancements to nonlinear VEHs, the complexity of their dynamic behavior poses a great challenge in achieving practical designs for a more robust broadband performance, especially when the nature of excitation is unknown. This

[1] Approximate analytical methods for bi-stable systems outside the scope of energy harvesting were originally established in [56, 57, 58, 59].

has driven researchers to explore newer concepts in the design of VEHs to increase the transduction efficiency and make them less sensitive to parameter and excitation uncertainties. Zhou et. al [8] have demonstrated that the idea of tri-stability can be utilized to design VEHs with shallow enough potential wells for low ambient excitation to activate large-amplitude output responses and sustain these responses over a wide frequency range. *However, as of today there are no analytical and/or rigorous experimental studies to elucidate the role of the nonlinearities or design parameters on the performance of such devices.*

1.3 Dissertation Objectives

While significant strides have been taken to improve the performance of nonlinear VEHs, some outstanding issues, as described in the previous section, particularly pertaining to the lack of analytical tools to understand their effective bandwidth, relative performance under optimal loading conditions and, more robust performance are yet to be resolved. The dissertation contributions towards resolving the aforedescribed issues can be outlined as follows:

- **Obtaining analytical solutions to define the effective frequency bandwidth of bi-stable VEHs in response to harmonic base excitations**. To achieve this goal, a nonlinear lumped-parameter model of a generic nonlinear VEH capable of operating in *mono-* as well as *bi-stable* configurations is used. By using perturbation methods, namely the method of multiple scales, analytical expressions that describe the amplitude and stability of the *intra-* and *inter-well* dynamics of the bi-stable configuration are constructed. Using these solutions, *i*) the presence of non-unique electric responses with competing basins of attractions are highlighted, *ii*) critical qualitative variations in the dynamics also known as bifurcations in the parameters' space are identified and, *iii*) the loci of these bifurcations are used to define an effective frequency bandwidth of a bi-stable VEH. *iv*) The influence of three critical design parameters, namely, the time constant ratio (ratio between the period of the mechanical system and the time constant of the harvesting circuit), the electromechanical coupling, and the shape of the potential function, on the effective frequency bandwidth is analyzed. Results are presented to elucidate the essential role which the design parameters, specifically the potential shape, and the electromechanical coupling, and the forcing level play towards optimizing the design and enhancing performance of bi-stable VEHs.

- **Comparing the relative performance of electrically optimized nonlinear energy harvesters**. Generally both *mono-* and *bi-stable* VEHs exhibit very complex dynamic responses which poses a great challenge when trying to accurately analyze their performance relative to one another. This dissertation compares the performance of these two classes in response to harmonic fixed-frequency excitations under optimal electric loading conditions. Towards this end, the model used in the first task along with the solutions are used to obtain analytical expressions for the steady-state output power. These expressions are utilized to optimize the power (*for both configurations*) with respect to the time-constant ratio which represents a direct measure of the electric load. The resulting expressions are then used to delineate the influence of the potential shape and the magnitude of excitation on the relative performance of the two configurations under optimal electric loading.

- **Investigating the response of a tri-stable nonlinear VEH for energy harvesting under harmonic base excitations**. This task is very similar in structure to the first task addressed in this dissertation with the main difference that the mathematical model used in the first task is modified to include higher-order nonlinearities. Recent research on utilizing a nonlinear oscillator with a three-well (tri-stable) potential function as a solution to further enhancing the response bandwidth is limited to numerical simulations and some experimental studies that do not provide a complete understanding of the qualitative dynamics and complex responses involved. To fill this gap in the literature, the generic mathematical model of a nonlinear VEH used in the first task is modified to incorporate quintic nonlinearities to produce a tri-stable potential energy function. A numerical investigation is carried out to gain a qualitative understanding of the effect of the higher order nonlinearities on the response behavior. The method of multiple scales is then utilized to construct analytical expressions for the steady-state periodic deflection and electric quantity of the harvester. These expressions are utilized to assess the stability of the steady-state responses and identify key bifurcations in the parameters space. The loci of these bifurcations are used to demarcate regions in the force-frequency space facilitating the approximation of the effective bandwidth of tri-stable VEHs. The influence of the electric parameters namely, the time constant ratio and the electromechanical coupling on the bandwidth of the harvester are studied. Finally, an experimental study is conducted to demonstrate the capability of the model to capture the qualitative behavior of

tri-stable nonlinear VEHs.

1.4 Dissertation Outline

The rest of the manuscript is organized as follows: Chapter 2 proposes a lumped-parameter nonlinear electromechanical model and uses it to classify the different types of nonlinear VEHs. Chapter 3 presents analytical solutions that govern the steady-state intra- and inter-well oscillations of a bi-stable VEH. Based on these solutions, key bifurcations are identified and several maps are constructed to define the effective bandwidth. Chapter 4 presents analytical expressions for the output power of mono- and bi-stable harvesters and compares their performance under optimal electric loading conditions. Chapter 5 investigates the response characteristics of a tri-stable VEH. A lumped-parameters electromechanical model with cubic and quintic nonlinearities is considered and used to obtain approximate analytical solutions governing the steady-state amplitude and electric responses of the harvester. The solutions are validated against numerical findings and an experimental case study is presented to validate the theoretical findings. Finally, Chapter 6 presents the main conclusions of this research and directions for future work.

Chapter 2

Nonlinear Energy Harvesters: Classification and Modeling

In this chapter, a basic mathematical model of a generic nonlinear VEH is presented and a classification of the various types of nonlinear VEHs is discussed.

2.1 Mathematical Model

Several lumped and distributed-parameter models have been developed to describe the dynamics of VEHs [6, 69]. For the most part, these models are device specific and not very well suited to develop a qualitative understanding of the response behavior. In order to gain the insights necessary for a more general understanding, we consider a canonical model consisting of a mechanical oscillator coupled to an electric circuit through an electromechanical coupling mechanism as shown in Fig. 2.1. The circuit can be a first order RC circuit representing a capacitive transduction mechanism (e.g., piezoelectric harvester), Fig. 2.1 (a); or a first-order RL circuit representing an inductive transduction mechanism (e.g., electromagnetic harvester), Fig. 2.1 (b). For both cases, the equations governing the motion can be written in the following general form:

$$m\ddot{\bar{x}} + c\dot{\bar{x}} + \frac{d\bar{U}(\bar{x})}{d\bar{x}} + \theta\bar{y} = \bar{F}\cos(\bar{\Omega}\tau), \tag{2.1a}$$

$$C_p\dot{\bar{y}} + \frac{\bar{y}}{R} = \theta\dot{\bar{x}} \text{ (piezoelectric)}, \qquad L\dot{\bar{y}} + R\bar{y} = \theta\dot{\bar{x}} \text{ (inductive)}, \tag{2.1b}$$

where the overdot represents a derivative with respect to time, τ. The variable $\bar{x}$ represents

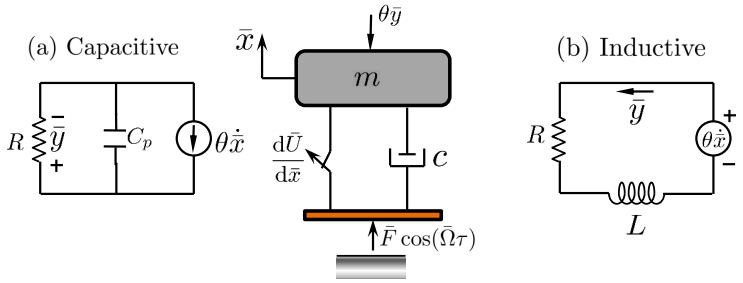

Figure 2.1: A simplified representation of a generic vibratory energy harvester.

the displacement of the oscillator mass m; c is the linear viscous damping coefficient; θ is the electromechanical coupling coefficient; C_p is the capacitance of the piezoelectric element; L is the inductance of the harvesting coil; and $\bar{y}$ is the electric quantity representing the induced voltage in capacitive VEHs and the induced current in inductive ones. Here, R represents the equivalent resistive load across which the electric quantity is measured. The term $\bar{F}\cos(\bar{\Omega}\tau)$ represents the external base excitation; where $\bar{F}$ is the amplitude, and $\bar{\Omega}$ is the frequency. The function $\bar{U}(\bar{x})$ is the potential energy of the mechanical subsystem and can be written in the the following general form:

$$\bar{U}(\bar{x}) = \frac{1}{2}k_1(1-r)\bar{x}^2 + \frac{1}{4}k_2\bar{x}^4 + \frac{1}{6}k_3\bar{x}^6, \tag{2.2}$$

where k_1, k_2 and k_3 represent the linear and nonlinear stiffness coefficients, and r is introduced to allow for variations in the stiffness around its nominal value. In the analysis of physically realizable nonlinear VEHs, the introduction of this constant is necessary to reflect the fact that the nonlinear stiffness coefficients cannot be changed without altering the linear stiffness.

Equation (2.1) can be further non-dimensionalized by introducing the following dimensionless quantities:

$$x = \frac{\bar{x}}{l_c}, \qquad t = \tau\omega_n, \qquad y = \frac{C_p}{\theta l_c}\bar{y} \text{ (piezoelectric)}, \qquad y = \frac{L}{\theta l_c}\bar{y} \text{ (inductive)}, \tag{2.3}$$

where l_c is a length scale, and $\omega_n = \sqrt{k_1/m}$ is the nominal short-circuit frequency when $r = 0$. This

yields the following nondimensional equations:

$$\ddot{x} + 2\zeta\dot{x} + (1-r)x + \delta x^3 + \gamma x^5 + \kappa^2 y = \mathcal{F}\cos(\Omega t), \tag{2.4a}$$

$$\dot{y} + \alpha y = \dot{x}, \tag{2.4b}$$

where,

$$\zeta = \frac{c}{2\sqrt{k_1 m}}, \qquad \delta = \frac{k_2 l_c^2}{k_1}, \qquad \gamma = \frac{k_3 l_c^4}{k_1} \qquad \mathcal{F} = \frac{\bar{F}}{k_1 l_c},$$

and

$$\kappa^2 = \frac{\theta^2}{k_1 C_p}, \qquad \alpha = \frac{1}{RC_p\omega_n} \text{ (piezolectric)}, \qquad \kappa^2 = \frac{\theta^2}{k_1 L}, \qquad \alpha = \frac{R}{L\omega_n} \text{ (inductive)}.$$

Here ζ represents the mechanical damping ratio, κ is a linear dimensionless electromechanical coupling coefficient, δ is the coefficient of cubic nonlinearity, γ is the coefficient of quintic nonlinearity, α is the ratio between the mechanical and electrical time constants of the harvester. For an inductive circuit, the time constant is L/R and for a capacitive circuit, it is RC. Also, $F\cos(\Omega t)$ represents the non-dimensionalized external base excitation term where $\mathcal{F}$ is the amplitude, and Ω is the frequency of excitation. The form of Equations (2.4) permits the classification of nonlinear VEHs into three major categories as shown in Fig. 2.2:

- Mono-stable ($r \leq 1$, $\delta \neq 0$ and $\gamma = 0$): In this case, the harvester exhibits one stable equilibrium point given by the trivial solution, $x_s = 0$. The oscillations of the harvester are confined to a single global potential as shown in Fig. 2.2(a). When $\delta > 0$, the restoring force increases with the displacement and is said to be of the hardening type. On the other hand, when $\delta < 0$, the restoring force decreases with displacement and is said to be of the softening type.

- Bi-stable ($r > 1$, $\delta > 0$ and $\gamma = 0$): In such a scenario, the trivial solution, ($x_s = 0$), becomes an unstable saddle and two nontrivial stable nodes, $x_s = \pm\sqrt{\frac{(r-1)}{\delta}}$ are born causing the harvester to become of the bi-stable type as shown in Fig. 2.2(a). When δ is increased, the separation distance between the wells which is defined by the location of the static equilibria, decreases.

- Tri-stable ($r < 1$, $\delta < 0$ and $\gamma > 0$): In this configuration, the potential energy function consists

of three stable nodes and two unstable saddles as shown in Fig. 2.2(a). These equilibria are given by $x_s = 0$ and $x_s = \pm\sqrt{\frac{-\delta \pm \sqrt{\delta^2 - 4(1-r)\gamma}}{2\gamma}}$. Note that when $\delta^2 - 4(1-r)\gamma < 0$, only the trivial solution exists.

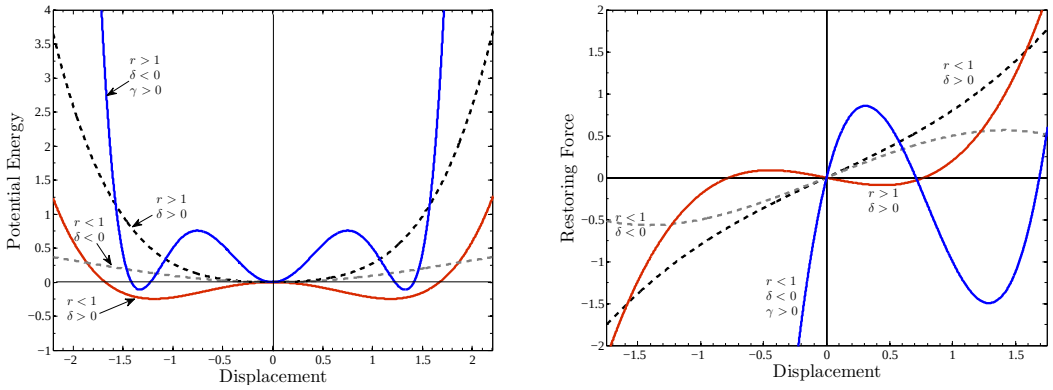

(a) (b)

Figure 2.2: Potential energies and restoring forces of different nonlinear VEHs.

Chapter 3

Effective Frequency Bandwidth of Bi-stable Vibratory Energy Harvesters

Due to the double-well potential function, bi-stable VEHs exhibit complex non-unique dynamic responses which are dependent on the depth of the potential wells, level of excitation, frequency of excitation and the design parameters. In this chapter, we aim to provide a basic qualitative insight into the response behavior of bi-stable VEHs and quantify an effective frequency bandwidth favorable for energy harvesting.

3.1 Model

Since this analysis is focused on determining the effective bandwidth of bi-stable harvesters, we consider the case when $\gamma = 0$ in Equation (2.4) to obtain,

$$\ddot{x} + 2\zeta\dot{x} + (1 - r)x + \delta x^3 + \kappa^2 y = \mathcal{F}\cos(\Omega t), \tag{3.1a}$$

$$\dot{y} + \alpha y = \dot{x}, \tag{3.1b}$$

The constant terms in Equations (3.1) are as described in chapter 2. Since this study is focused on the analysis of bi-stable VEHs, we limit our attention to the case when $r > 1$, and $\delta > 0$. In such a scenario, as shown in Fig. 3.1, the quartic potential energy function is bi-stable with the following three extrema:

$$x_s = 0, \qquad x_s = \pm\sqrt{\frac{(r-1)}{\delta}}, \tag{3.2}$$

where the maximum occurring at $x_s = 0$, represents an unstable saddle, while the global minima, $x_s = \pm\sqrt{\frac{(r-1)}{\delta}}$, represent stable equilibrium solutions (nodes).

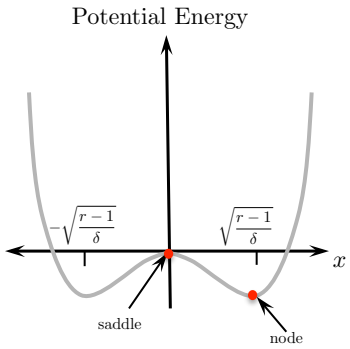

Figure 3.1: Schematic of a bi-stable potential energy function.

3.2 Response to Harmonic Fixed-Frequency Excitations

Bi-stable VEHs are capable of producing large amplitude responses over certain frequency ranges under harmonic excitations [3]. These responses occur when the excitation amplitude is large enough to permit the dynamic trajectories to escape the basin of attraction of a single stable node allowing the harvester to perform inter-well motions. Unfortunately, these desired motions cannot be uniquely realized over a large frequency bandwidth and are often accompanied with other, less desirable, small amplitude intra-well responses. To further illustrate this issue, Equations (3.1a) and (3.1b) are numerically integrated to construct a bifurcation diagram of the frequency response for different excitation amplitudes as depicted in Fig. 3.2.

When the normalized excitation amplitude is relatively small, $\mathcal{F} = 0.045$, as shown in Fig. 3.2(a), the dynamic trajectories remain confined to a single potential well because the excitation is not large enough for them to overcome the potential barrier (the saddle) and escape from the well. As such, the harvester cannot perform the large-amplitude inter-well oscillations desired for energy

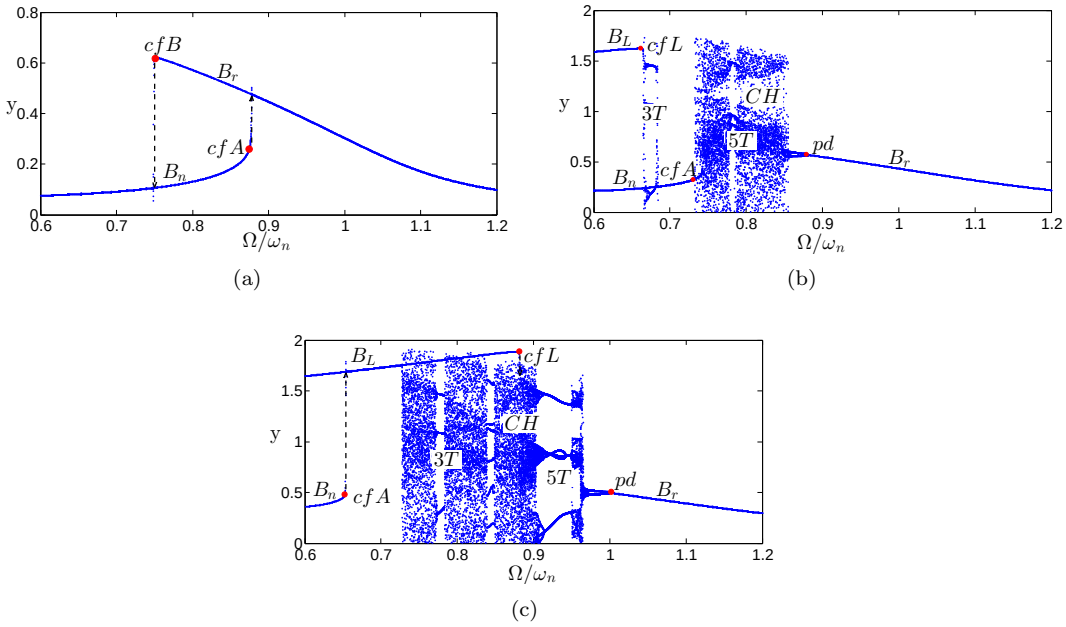

Figure 3.2: Frequency-response curves for a bi-stable harvester at three different excitation levels. Results are obtained for Equation (3.1) with $\zeta = 0.05$, $\delta = 0.5$, $r = 1.5$, $\kappa^2 = 0.01$, $\alpha = 0.1$, and a base excitation of normalized amplitude (a) $\mathcal{F} = 0.045$, (b) $\mathcal{F} = 0.11$ and (c) $\mathcal{F} = 0.165$

harvesting. The frequency-response curve appears to be of the softening nature with the large amplitude resonant oscillations, B_r, occurring at frequencies smaller than the resonance frequency. The response curve undergoes two bifurcations: The first occurs as the frequency is decreased and the resonant branch, B_r, loses stability through a cyclic-fold bifurcation, cfB, giving way to the smaller non-resonant branch, B_n. The second occurs when the frequency is increased and the branch, B_n, undergoes another cyclic-fold bifurcation, cfA, giving way to the resonant branch, B_r.

As shown in Fig. 3.2(b), when the excitation is increased to $\mathcal{F} = 0.11$, another large-amplitude branch of solutions, B_L, appears near the lower end of the frequency range. This branch represents the large-amplitude periodic inter-well responses desirable for energy harvesting. It can be clearly seen that, for the range of frequencies considered, this large amplitude branch quickly disappears in a cyclic-fold bifurcation, cfL, and gives way to more complex $3-period$ periodic responses that represent a mixture of inter- and intra-well motions. On the other hand, as the frequency is decreased from higher to lower values, it is noted that the cyclic fold bifurcation, cfB, occurring on the resonant intra-well branch, B_r, disappears and is replaced by the period doubling bifurcation, pd. As the frequency is decreased further, a cascade of period doubling bifurcations

occur leading to a window of inter-well chaotic motions, CH, which disappears in a boundary crisis near cfA.

When the excitation is increased further to the higher level, $\mathcal{F} = 0.165$, as observed in Fig. 3.2(c), three distinct behaviors are noted. Firstly, the cfL bifurcation occurs at a higher value of the excitation frequency meaning that the desired large-orbit inter-well oscillation branch now extends over a wider frequency; secondly, the period doubling bifurcation, *pd*, of the resonant branch is activated at a higher value of the frequency, meaning that complex responses can now be initiated at larger excitation frequencies; and thirdly, the cyclic-fold bifurcation cfA occurs at lower values of the frequency meaning that the jump to the desired large-amplitude oscillations can now occur at lower frequency values.

The previous numerical analysis indicates that there are three critical bifurcations in the frequency-response curves for the electric quantity, y, that can help better define the effective bandwidth of bi-stable energy harvesters for a given forcing. These bifurcations are,

1. The cyclic fold bifurcation, cfL. This bifurcation defines how far the large amplitude inter-well motion extends in the frequency domain. The larger the value of the frequency at which cfL occurs, the further the large-amplitude branch of solutions extends. If the frequency at which cfL occurs is smaller than that associated with cfA, the large amplitude inter-well responses can never be unique in the frequency domain. Furthermore, if the frequency at which cfL occurs is larger than *pd*, there is a larger chance that the harvester performs unique inter-well motions, or inter-well motions accompanied by aperiodic motions.

2. The cyclic fold bifurcation, cfA. This bifurcation defines how far the small branch of non-resonant intra-well motion, B_n, extends in the frequency domain. For energy harvesting applications, the smaller cfA is, the better.

3. The period-doubling bifurcation, *pd*. This bifurcation represents the minimum value of the excitation frequency for which the resonant branch of intra-well solutions, B_r is periodic. Below this value, more complex inter-well dynamic responses can be initiated. The larger the value of the frequency at which *pd* occurs, the larger the bandwidth of inter-well motions can be.

The loci of the aforementioned bifurcations in the force-frequency space can be used as an approximate measure of the effective frequency bandwidth wherein the harvester can produce large amplitude electric responses. As such, deriving approximate expressions for these bifurcations can

serve as an initial step in the design of efficient bi-stable harvesters for a given excitation. In what follows, we use perturbation methods to obtain several approximations for these bifurcations and show how they can be utilized to define the effective bandwidth of bi-stable harvesters.

3.3 Approximate Analytical Solutions

We first analyze the local intra-well dynamics, i.e. within a single potential well and develop analytical expressions to predict the occurrence of the cyclic-fold and period-doubling bifurcations (cfA, cfB, and pd) of the harvester. We then consider the global inter-well oscillations and approximate the cyclic-fold bifurcation point, cfL.

3.3.1 Intra-well Oscillations of the Bi-stable Harvester

To study the dynamics within a single potential well of the harvester, we expand the dynamics about the stable nodes by introducing $x_t = x - x_s$ where $x_s = \pm\sqrt{\frac{(r-1)}{\delta}}$ in Equations (3.1a) and (3.1b) and expanding up to cubic terms we obtain

$$\ddot{x}_t + 2\zeta\dot{x}_t + \omega_n^2 x_t + \tau x_t^2 + \delta x_t^3 + \kappa^2 y = \mathcal{F}\cos(\Omega t), \tag{3.3a}$$

$$\dot{y} + \alpha y = \dot{x}_t, \tag{3.3b}$$

where, $\omega_n = \sqrt{2(r-1)}$ represents the linearized oscillation frequency within a single potential well, $\tau = 3\sqrt{(r-1)\delta}$ is the coefficient of quadratic nonlinearity, and x_t represents the dynamic trajectories around the non-trivial equilibria. It is worth noting that the expanded equations now include a quadratic term to capture the asymmetric nature of the response within a single potential well.

Utilizing the method of multiple scales [70], a uniform approximate analytical solution of Equations (3.3a) and (3.3b) is obtained next. Towards that end, the time dependence is expanded into multiple time scales in the form:

$$T_n = \epsilon^n t, \tag{3.4}$$

where ϵ is a book keeping parameter. With this definition of the time scales, the time derivative can

be expressed as:

$$\frac{d}{dt} = \sum_{n=0}^{m} \epsilon^n D_n, \tag{3.5}$$

where $D_n = \frac{\partial}{\partial T_n}$. Furthermore, x_t and y can be expanded in the following form:

$$x_t(t,\epsilon) = \sum_{n=0}^{m} \epsilon^n x_n(T_0, T_1, \ldots, T_n), \qquad y(t,\epsilon) = \sum_{n=0}^{m} \epsilon^n y_n(T_0, T_1, \ldots, T_n) \tag{3.6}$$

The constant parameters in the equations are also scaled such that the effect of viscous damping appears at the same order of the perturbation problem as the cubic nonlinearity, forcing, and electromechanical coupling. In other words, we let

$$\zeta = \epsilon^2\zeta, \quad \mathcal{F} = \epsilon^2\mathcal{F}, \quad \tau = \epsilon\tau, \quad \delta = \epsilon^2\delta, \quad \kappa^2 = \epsilon^2\kappa^2. \tag{3.7}$$

To express the nearness of the excitation frequency, Ω, to the first modal frequency of the harvester within a single potential well, we let

$$\Omega = \omega_n + \epsilon^2\sigma, \tag{3.8}$$

where σ is a small detuning parameter. Substituting Equations (3.5)-(3.8) back into Equations (3.3a) and (3.3b), truncating at order ϵ^2 and collecting terms of equal powers of ϵ yields

$O(\epsilon^0)$:

$$D_0^2 x_0 + \omega_n^2 x_0 = 0, \tag{3.9a}$$

$$D_0 y_0 + \alpha y_0 = D_0 x_0. \tag{3.9b}$$

$O(\epsilon^1)$:

$$D_0^2 x_1 + \omega_n^2 x_1 = -2D_0 D_1 x_0 - \tau x_0^2, \tag{3.10a}$$

$$D_0 y_1 + \alpha y_1 = D_0 x_1 + D_1 x_0 - D_1 y_0. \tag{3.10b}$$

$O(\epsilon^2)$:

$$D_0^2 x_2 + \omega_n^2 x_2 = -2D_0 D_1 x_1 - D_1^2 x_0 - 2D_0 D_2 x_0 - 2\zeta D_0 x_0 - \tau x_0 x_1 - \delta x_0^3$$
$$-\kappa^2 y_0 + F\cos(\Omega t), \tag{3.11a}$$

$$D_0 y_2 + \alpha y_2 = D_0 x_2 + D_1 x_1 + D_2 x_0 - D_1 y_1 - D_2 y_0. \tag{3.11b}$$

The solution of the zeroth order perturbation problem, Equations (3.9a) and (3.9b), can be written as:

$$x_0 = A(T_1, T_2)e^{i\omega_n T_0} + cc, \tag{3.12a}$$

$$y_0 = ZA(T_1, T_2)e^{i\omega_n T_0} + cc. \tag{3.12b}$$

where cc is the complex conjugate, $A(T_1, T_2)$ is a complex valued function to be determined at a later stage of the analysis, and $Z = \frac{\omega_n^2 + i\omega_n\alpha}{\alpha^2+\omega_n^2}$. Substituting Equations (3.12a) and (3.12b) into Equations (3.10a) and (3.10b), and eliminating the secular terms, terms that have the coefficient $e^{\pm i\omega_n T_0}$, yields,

$$D_1 A(T_1, T_2) = 0 \Longrightarrow A = A(T_2). \tag{3.13}$$

With this result, the solution of the first order Equations (3.10a) and (3.10b) can be written as:

$$x_1 = \frac{\tau}{\omega_n^2}\left(\frac{1}{3}A^2 e^{i2\omega_n T_0} - 2A\bar{A}\right) + cc, \tag{3.14a}$$

$$y_1 = Z_1 \frac{\tau}{3\omega_n^2} A^2 e^{i2\omega_n T_0} + cc, \tag{3.14b}$$

where $\bar{A}$ is the complex conjugate of A and $Z_1 = \frac{4\omega_n^2 + 2i\omega_n\alpha}{\alpha^2+4\omega_n^2}$. Now, to obtain the unknown function A, we substitute Equations (3.12a), (3.12b), and (3.14a) into Equation (3.11a), then eliminate the secular terms to obtain the following nonlinear first order differential equation for the unknown A:

$$-2i\omega_n D_2 A - i\omega_n 2\zeta A - Z\kappa^2 A + \left[\frac{10}{3}\left(\frac{\tau}{\omega_n}\right)^2 - 3\delta\right]A^2\bar{A} + \frac{\mathcal{F}}{2}e^{i\sigma T_2} = 0. \tag{3.15}$$

To find the solution of Equation (3.15), we express the complex valued function, A, in the polar form

$$A(T_2) = \frac{1}{2}a(T_2)e^{i\psi(T_2)}, \qquad \bar{A}(T_2) = \frac{1}{2}a(T_2)e^{-i\psi(T_2)}. \tag{3.16}$$

Substituting Equation (3.16) into Equation (3.15), and separating the real and imaginary parts of the outcome, we obtain

$$D_2 a = -\Big(\zeta + \zeta_e\Big)a + \tfrac{\mathcal{F}}{2\omega_n}\sin\beta, \tag{3.17a}$$

$$aD_2\beta = (\sigma - \gamma_s)a - N_{eff}a^3 + \tfrac{\mathcal{F}}{2\omega_n}\cos\beta, \tag{3.17b}$$

where $\beta = \sigma T_2 - \psi$, $\zeta_e = \frac{\kappa^2\alpha}{2(\alpha^2+\omega_n^2)}$ represents the electric damping, $N_{eff} = \frac{1}{\omega_n}\left[\frac{3}{8}\delta - \frac{5}{12}\frac{\tau^2}{\omega_n^2}\right]$ represents the effective nonlinearity coefficient, and $\gamma_s = \frac{\kappa^2\omega_n}{2(\alpha^2+\omega_n^2)}$ represents a linear shift in the system's natural frequency as a result of the electric coupling.

In the case of energy harvesting, we are interested in investigating the steady-state response. To that end, we set the time derivatives in Equations (3.17a) and (3.17b) to zero, square and add the resulting equations to obtain

$$\zeta_{eff}^2 a_0^2 + \Big[(\sigma - \gamma_s)a_0 - N_{eff}a_0^3\Big]^2 = \frac{\mathcal{F}^2}{4\omega_n^2}. \tag{3.18}$$

where $\zeta_{eff} = \zeta + \zeta_e$ represents the effective damping and a_0 represents the steady-state amplitude. Equation (3.18) is a nonlinear frequency-response equation, which can be solved analytically for the steady-state amplitude for any given forcing, $\mathcal{F}$. Depending on the forcing and the excitation frequency, there exists one or three positive real valued solutions. The stability of these equilibria can be determined by assessing the eigenvalues of the associated Jacobian matrix. The steady-state solutions can then be expressed in the following form:

$$x_t(t) = a_0\cos(\Omega t - \beta_0) + \tfrac{\tau}{2\omega_n^2}(-a_0^2 + \tfrac{1}{3}a_0^2\cos(2\Omega t - 2\beta_0)) + \tfrac{\delta}{32\omega_n^2}a_0^3\cos(3\Omega t - 3\beta_0), \tag{3.19a}$$

$$\begin{aligned} y(t) = {} & \tfrac{\omega_n}{\sqrt{\alpha^2+\omega_n^2}}a_0\cos(\Omega t - \beta_0 + \psi_1) + \tfrac{\tau}{3\omega_n\sqrt{\alpha^2+4\omega_n^2}}a_0^2\cos(2\Omega t - 2\beta_0 + \psi_2) \\ & + \tfrac{3\delta}{32\omega_n\sqrt{\alpha^2+9\omega_n^2}}a_0^3\cos(3\Omega t - 3\beta_0 + \psi_3), \end{aligned} \tag{3.19b}$$

$$\text{where,} \qquad \beta_0 = \tan^{-1}\left(\tfrac{\zeta_{eff}}{(\sigma-\gamma_s) - N_{eff}a_0^2}\right), \qquad \psi_n = \tan^{-1}\left(\tfrac{\alpha}{n\omega_n}\right).$$

3.3.2 Bifurcation Points

3.3.2.1 Cyclic-Fold Bifurcations

We are interested in determining the cyclic-fold bifurcations of the resonant and non-resonant branches of intra-well oscillations. These points, also known as the turning points, represent the value of frequency at which the slope of the frequency-response curve approaches infinity. This yields the following relation for the loci of the bifurcation points in the space of σ and a:

$$a_b^2 = \frac{2(\sigma_b - \gamma_s) \pm \sqrt{(\sigma_b - \gamma_s)^2 - \zeta_{eff}^2}}{3N_{eff}} \tag{3.20}$$

where a_b and σ_b represent the amplitude of oscillation and detuning parameter values at the bifurcation point. Depending on the value of σ_b, Equation (3.20) can have two positive real-valued solutions which represent the amplitudes at which the cyclic-fold bifurcations of the resonant and non-resonant branch of intra-well oscillations occur. The loci of these bifurcations in the space of $\mathcal{F}$ and normalized excitation frequency Ω/ω_n, can then be obtained by substituting a_b and σ_b in Equation (3.18) and solving the resulting equations for $\mathcal{F}$. A sample curve is shown in Fig. 3.3 illustrating how, below a critical forcing, the cyclic-fold bifurcations collide with each other and disappear. In such a scenario, the harvester performs linear oscillations within a single well. As the forcing amplitude is increased, the separation between the frequencies at which the cyclic-fold bifurcations occur increases and the softening nonlinearity becomes more apparent in the frequency response.

3.3.2.2 Period Doubling Bifurcation

To determine the points of period doubling bifurcation in the parameter space, we examine the stability of the approximate steady-state periodic solutions for the deflection and electric quantity by introducing small perturbations in the form,

$$\tilde{x} = x_t(t) + \nu_1(t), \qquad \tilde{y} = y(t) + \nu_2(t). \tag{3.21}$$

where $\nu_1(t)$ and $\nu_2(t)$ are time-dependent perturbations of the deflection and electric quantity, respectively. Substituting Equation (3.21) in Equation (3.1a), then linearizing for small perturbations,

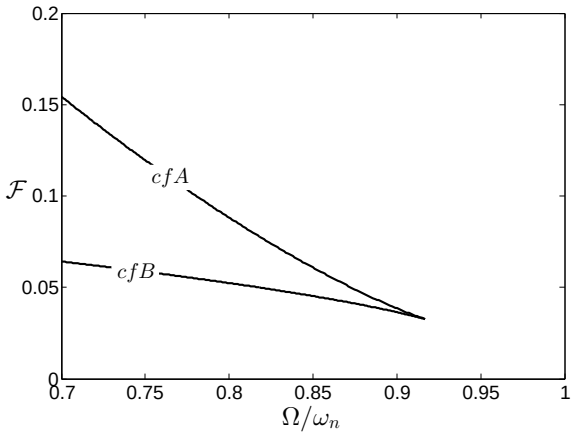

Figure 3.3: Loci of the cyclic-fold bifurcations in the force frequency parameter space. Results are obtained for $\zeta = 0.05$, $\delta = 0.5$, $r = 1.5$, $\kappa^2 = 0.01$, and $\alpha = 0.1$.

we obtain the following variational equations governing the evolution of the perturbation dynamics

$$\ddot{\nu}_1 + 2\zeta\dot{\nu}_1 + [\lambda_0 + \lambda_1\cos(\theta) + \lambda_2\cos(2\theta) + \lambda_3\cos(3\theta)]\nu_1 + \kappa^2\nu_2 = 0, \tag{3.22a}$$

$$\dot{\nu}_2 + \alpha\nu_2 = \dot{\nu}_1, \tag{3.22b}$$

where,

$$\lambda_0 = \omega_n^2 + \frac{3\delta\tau^2 a_0^2}{2\omega_n^2}\left[\frac{\omega_n^2}{\tau^2} - \frac{2}{3\delta} + \frac{a_0^2}{2\omega_n^2}\left(\frac{a_0^2\tau^2}{512}\left(\frac{2}{3\omega_n^2} + \frac{\delta}{\tau^2}\right)^2 + \frac{19}{18}\right)\right],$$
$$\lambda_1 = 2\tau a_0 + \frac{\delta\tau a_0^3}{2\omega_n^2}\left[\frac{a_0^2}{32\omega_n^2}\left(\frac{2\tau^2}{3\omega_n^2} + \delta\right) - 5\right],$$
$$\lambda_2 = \tau^2 a_0^2\left[\frac{1}{3\omega_n^2} + \delta\left(\frac{3}{2\tau^2} - \frac{5a_0^2}{16\omega_n^4} + \frac{3\delta a_0^4}{32\omega_n^2\tau^2}\right)\right],$$
$$\lambda_3 = \frac{\tau^3 a_0^3}{2\omega_n^2}\left[\frac{1}{12\omega_n^2} + \frac{\delta}{\tau^2}\left(\frac{9}{8} - \frac{3a_0^2}{16\omega_n^2} - \frac{a_0^2\tau^2}{8\omega_n^4}\right)\right],$$

and $\theta = \Omega t + \beta$. Equation (3.22a) represents a Hill's type differential equation with three parametric-type excitations; $\lambda_1\cos(\theta)$, $\lambda_2\cos(2\theta)$, and $\lambda_3\cos(3\theta)$ with the first being the most dominant. Each of these terms produce parametric resonances at half their frequency components which translates to a loss of stability of the solution in the frequency domain. Since the response exhibits frequency components that are half of their existing values after a period-doubling bifurcation, we seek a

particular solution of Equation (3.22a) in the form, [71]

$$\nu_1 = e^{\epsilon t}\left(S_1 \cos\frac{\theta}{2} + S_2 \sin\frac{\theta}{2}\right), \qquad \nu_2 = e^{\epsilon t}\left(T_1 \cos\frac{\theta}{2} + T_2 \sin\frac{\theta}{2}\right). \tag{3.23}$$

where $\epsilon = 0$ at the bifurcation point. Substituting Equation (3.23) into Equation (3.22a) and 3.22b), then equating the coefficients of $\cos\frac{\theta}{2}$ and $\sin\frac{\theta}{2}$ to zero separately yields four simultaneous algebraic equations in the unknowns S_1, S_2, T_1 and T_2. Setting the characteristic determinant of these equations to zero, yields the following polynomial equation for Ω at the period doubling bifurcation:

$$\begin{aligned}\frac{\Omega^6}{64} + \left(\alpha^2 + 4\zeta^2 - 2\kappa^2 - \lambda_0\right)\frac{\Omega^4}{16} + \Bigg(16\alpha^2\zeta^2 + 16\kappa^2\alpha\zeta - 8\alpha^2\lambda_0 + 8\kappa^2\lambda_0 \\ + 4\kappa^2 + 4\lambda_0^2 - \lambda_1^2\Bigg)\frac{\Omega^2}{16} + \alpha^2\left(\lambda_0^2 - \frac{\lambda_1^2}{4}\right) = 0\end{aligned} \tag{3.24}$$

For a given a_0 associated with some excitation magnitude, Equation (3.24) can be solved for the

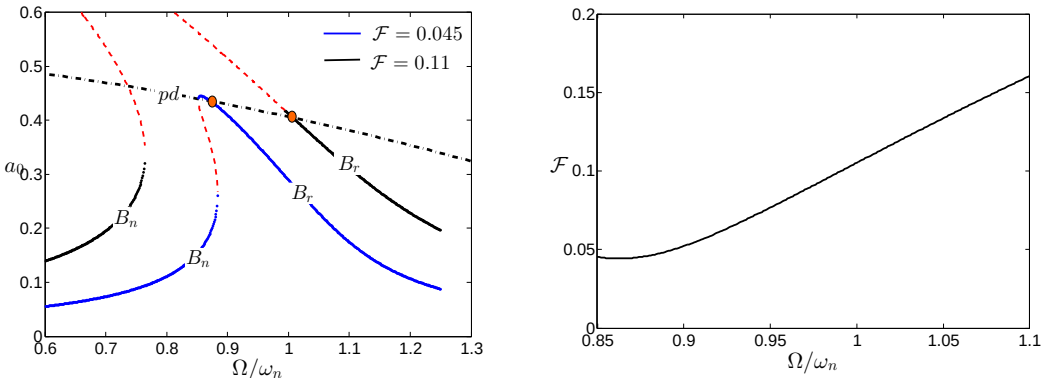

(a) (b)

Figure 3.4: (a) Intersection of the period-doubling instability curve with the frequency-response curve. (b) Loci of the *pd* bifurcations in the force-frequency parameter space. Results are obtained for $\zeta = 0.05$, $\delta = 0.5$, $r = 1.5$, $\kappa^2 = 0.01$, and $\alpha = 0.1$.

corresponding Ω at the *pd* bifurcation. Out of the resulting solutions, the one associated with the principle resonance is used to approximate the *pd* bifurcation point. Figure 3.4(a) depicts the period-doubling bifurcation which is defined by the intersection of the resonant branch of solution, B_r, obtained from Equation (3.18) with that obtained by solving Equation (3.24) for the excitation frequency, Ω, at a given forcing, $\mathcal{F}$, and for a given amplitude a_0 (dashed lines represent unstable

solutions). By repeating this process for different values of the forcing, loci of the *pd* bifurcations in the force-frequency parameter space can be established as depicted in Fig. 3.4(b). Results clearly illustrate how the frequency at which the *pd* bifurcation occurs, increases with the forcing level.

3.3.3 Inter-well Oscillations of the Bi-stable Harvester

Next, we analyze the global inter-well oscillations. Since, in this case, the effective local stiffness about the unstable saddle is negative ($r > 1$), it is very difficult to implement perturbation methods in the traditional sense. To overcome this issue, we first scale the damping, coupling, and external excitation at order ϵ as implemented in [56]; this yields,

$$\ddot{x} + (1 - r)x + \delta x^3 = O(\epsilon), \tag{3.25}$$

Next, we assume that the first order harmonic solution $x = \bar{A}\cos(\Omega t)$, is an approximate solution of Equation (3.25), which upon substitution in Equation (3.25) yields

$$(-\Omega^2 x + (1 - r)x + \delta x^3) = O(\epsilon) \tag{3.26}$$

This implies that the left-hand side of the previous equation can be scaled at order ϵ. Adding and subtracting the term $\Omega^2 x$ to the left-hand side of Equation (3.1a) and using the scaling of Equation (3.25), we can write

$$\begin{gathered} \ddot{x} + 2\epsilon\zeta\dot{x} + \Omega^2 x + \epsilon(-\Omega^2 x + (1 - r)x + \delta x^3) + \epsilon\kappa^2 y = \epsilon\mathcal{F}\cos(\Omega t), \\ \dot{y} + \alpha y = \dot{x}. \end{gathered} \tag{3.27}$$

Now the method of multiple scales can be implemented in the traditional way. Substituting Equations (3.5), (3.6) into Equation (3.27), truncating at the order of ϵ, and collecting terms of equal powers of ϵ, we obtain

$O(\epsilon^0)$:

$$D_0^2 x_0 + \Omega^2 x_0 = 0, \tag{3.28a}$$

$$D_0 y_0 + \alpha y_0 = D_0 x_0, \tag{3.28b}$$

$O(\epsilon)$:

$$D_0^2 x_1 + \Omega^2 x_1 = -2D_0 D_1 x_0 - 2\zeta D_0 x_0 - (-\Omega^2 x_0 + (1-r)x_0 + \delta x_0^3)$$
$$+F\cos(\Omega t) - \kappa^2 y_0, \tag{3.29a}$$
$$D_0 y_1 + \alpha y_1 = D_0 x_1 + D_1 x_0 - D_1 y_0. \tag{3.29b}$$

The solutions of Equations (3.28a) and (3.28b) can be written as

$$\begin{aligned} x_0 &= A(T_1)e^{i\Omega T_0} + cc, \\ y_0 &= ZA(T_1)e^{i\Omega T_0} + cc, \quad \text{where} \quad Z = \frac{\Omega^2 + i\alpha\Omega}{\Omega^2 + \alpha^2} \end{aligned} \tag{3.30}$$

Similar to the method employed in section (3.3.1), we substitute the solutions given by Equation (3.30) into Equation (3.29a), eliminate the secular terms, and express the complex valued function, A, in the polar form which results in the response amplitude and phase modulation equations. These equations are then used to obtain the following nonlinear frequency response equation:

$$\zeta_{eff}^2 a_0^2 + \left[(\Omega^2 - (1-r) - \gamma_s)\frac{a_0}{2\Omega} - \frac{3\delta}{8\Omega}a_0^3\right]^2 = \frac{\mathcal{F}^2}{4\Omega^2}, \tag{3.31}$$

where, $\zeta_{eff} = (\zeta + \zeta_e)$, $\zeta_e = \kappa^2\alpha/2(\alpha^2+\Omega^2)$ and $\gamma_s = \kappa^2\Omega^2/(\alpha^2+\Omega^2)$. Upon eliminating the secular terms in Equation (3.29a), the equation becomes

$$D_0^2 x_1 + \Omega^2 x_1 = -\frac{\delta a^3}{8} e^{3i(\Omega T_0 + \phi)} + cc, \tag{3.32}$$

for which the particular solution can be written as

$$x_1 = \frac{\delta a^3}{64\Omega^2} e^{3i(\Omega T_0 + \phi)} + cc, \tag{3.33}$$

and

$$y_1 = Z_2 \frac{\delta a^3}{64\Omega^2} e^{3i(\Omega T_0 + \phi)} + cc, \quad \text{where} \quad Z_2 = \frac{9\Omega^2 + 3i\alpha\Omega}{\alpha^2 + 9\Omega^2}, \tag{3.34}$$

Substituting the zeroth and first-order solutions back into the assumed expansion, Equation (3.6), the total analytical solution for the inter-well deflection and electric responses of the bi-stable harvester can be written as

$$x(t) = a_0 \cos(\Omega t + \phi_0) + \tfrac{\delta a_0^3}{32\Omega^2} \cos(3\Omega t + 3\phi_0), \tag{3.35a}$$

$$y(t) = \tfrac{a_0 \Omega}{\sqrt{\alpha^2+\Omega^2}} \cos(\Omega t + \phi_0 + \psi_1) + \tfrac{3\delta a_0^3}{32\Omega\sqrt{\alpha^2+9\Omega^2}} \cos(3\Omega t + 3\phi_0 + \psi_3), \tag{3.35b}$$

$$\text{where,} \qquad \phi_0 = \tan^{-1}\left(\tfrac{8\zeta_{eff}\Omega}{4(\Omega^2-(1-r)-\gamma_s)-3\delta a_0^2}\right), \qquad \psi_n = \tan^{-1}(\alpha/n\Omega).$$

3.3.3.1 Cyclic-Fold Bifurcation

In the case of inter-well oscillations, we are interested in determining the cyclic-fold bifurcation point, cfL, which corresponds to the value of frequency at which the stable and unstable large-orbit solutions coalesce. As shown in section 3.3.2.1, we find the cyclic-fold bifurcation point by determining the value of frequency at which the slope of the frequency-response curve for inter-well oscillations approaches infinity. Towards that end, we utilize the condition $\frac{d\Omega}{da_0}\big|_{a_b,\Omega_b} = 0$ in Equation (3.31) to obtain

$$27\delta^2 a_b^4 - 48\delta(\Omega_b^2 - (1-r) - \gamma_s)a_b^2 + 16(\Omega_b^2 - (1-r) - \gamma_s)^2 + 64\Omega_b^2\zeta_{eff}^2 = 0 \tag{3.36}$$

a_b and Ω_b represent the amplitude and frequency of the response at the bifurcation point. Depending on the value of Ω_b, Equation (3.36) has two positive real-valued solutions out of which the one with the large amplitude represents inter-well oscillations. The locus of the cyclic fold bifurcation in the $\mathcal{F}$ - Ω space is then obtained by substituting a_b and the corresponding Ω_b into Equation (3.31) and solving the resulting equations for the critical forcing, $\mathcal{F}$.

Figure 3.5 depicts the locus of the cyclic-fold bifurcation of the inter-well oscillation branch in the force-frequency parameter space clearly illustrating how the frequency at which the cfL occurs increases as the magnitude of the forcing increases, thereby extending the desirable bandwidth of the harvester.

3.3.4 Asymptotic Responses

Equations (3.18) and (3.31) are used to analytically construct the frequency-response curves of the system for two different forcing amplitudes as depicted in Fig. 3.6. As shown earlier in the

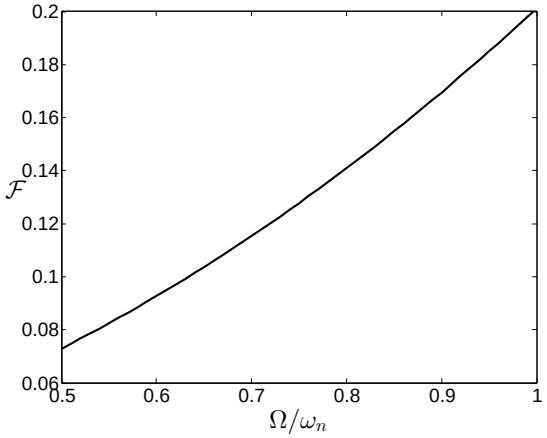

Figure 3.5: Locus of the cyclic-fold bifurcation of the inter-well oscillation branch in the force frequency parameter space. Results are obtained for $\zeta = 0.05$, $\delta = 0.5$, $r = 1.5$, $\kappa^2 = 0.01$, and $\alpha = 0.1$.

numerical simulations of Fig. 3.2, Fig. 3.6 captures the three critical frequencies pd, cfL, and cfA and their dependence on the excitation amplitude. A comparison between Fig. 3.6(a) and Fig. 3.6(b) reveals that both of the cyclic fold bifurcation, cfL and the period doubling bifurcation, pd, are shifted towards higher values of frequency as the magnitude of excitation is increased. On the other hand, the cyclic-fold bifurcation cfA occurs at a lower value of the frequency demonstrating the enhanced bandwidth of the harvester as the excitation amplitude is increased.

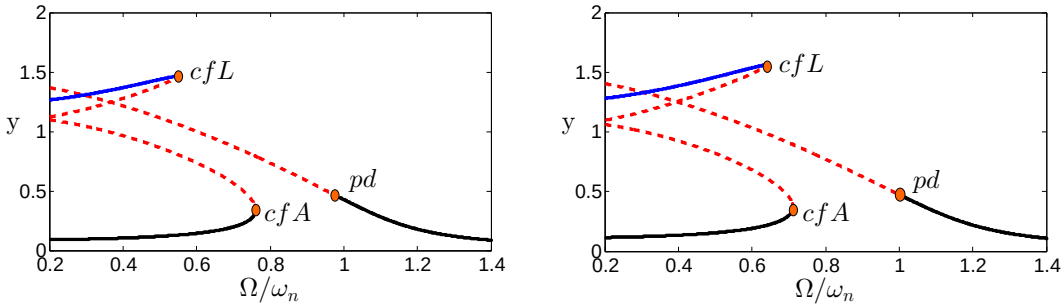

Figure 3.6: Analytical frequency-response curves for a bi-stable harvester at two different excitation levels. Dashed lines represent unstable solutions. Results are obtained for $\zeta = 0.05$, $\delta = 0.5$, $r = 1.5$, $\kappa^2 = 0.01$, $\alpha = 0.1$, and a base excitation of normalized amplitude (a) $\mathcal{F} = 0.08$, (b) $\mathcal{F} = 0.1$

The analytical results are also compared to the stroboscopic bifurcation map obtained numerically showing very good agreement and the ability of the analytical responses to predict the

bifurcation points with relative accuracy as depicted in Fig. 3.7. A comparison of the results reveal that the analytical solution overpredicts the frequency at which the period doubling bifurcation, *pd* occurs. This can be attributed to the fact that the method utilized to predict the period doubling bifurcation point involves approximating the loss of stability through variational equations that are linearized assuming small perturbations. Furthermore, since the period doubling bifurcation invariably precedes the onset of chaotic motions, the analytical predictions can be used as a threshold while designing bi-stable energy harvesters.

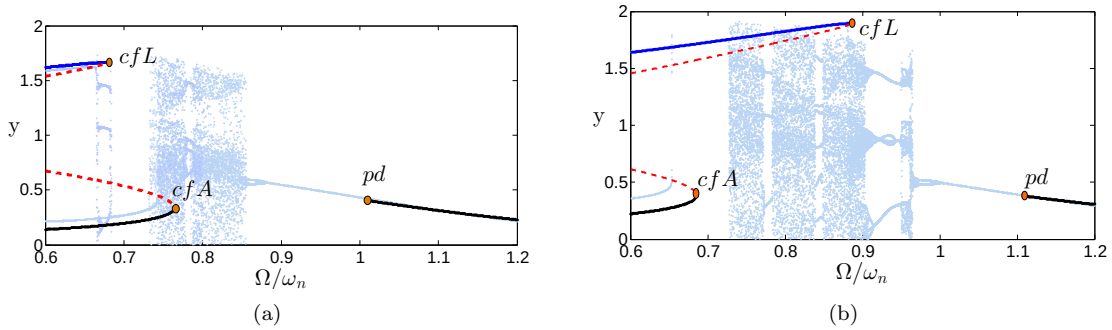

Figure 3.7: Comparison of numerical and analytical frequency responses. Light blue curves represent numerical solutions. Results are obtained for normalized base excitation amplitudes (a) $\mathcal{F} = 0.11$ and (b) $\mathcal{F} = 0.165$.

3.3.5 Influence of the Electric Parameters on the Bifurcation Points

In this section, we study the influence of the important electric parameters namely, the time constant ratio, α, and the electromechanical coupling, κ^2 on the critical bifurcations. The time constant ratio can be used as a measure of the influence of the electric load while κ^2 represents the strength of coupling between the mechanical and electrical subsystems. Figure 3.8 depicts the effect of varying the time constant ratio on the loci of the bifurcations of the intra- and inter-well oscillations in the forcing-frequency parameter space. A close inspection of the Figures. 3.8(a), 3.8(b) and 3.8(c) reveals that the locations of the bifurcation points cfB and cfA, pd and cfL are nearly the same for all values of α despite varying it by an order of magnitude from the nominal value of 0.1. As such, the time constant ratio has very little influence on the effective bandwidth of the harvester, but could influence the response amplitude. As a result, changing the electric load does not significantly alter the loci of the bifurcation points.

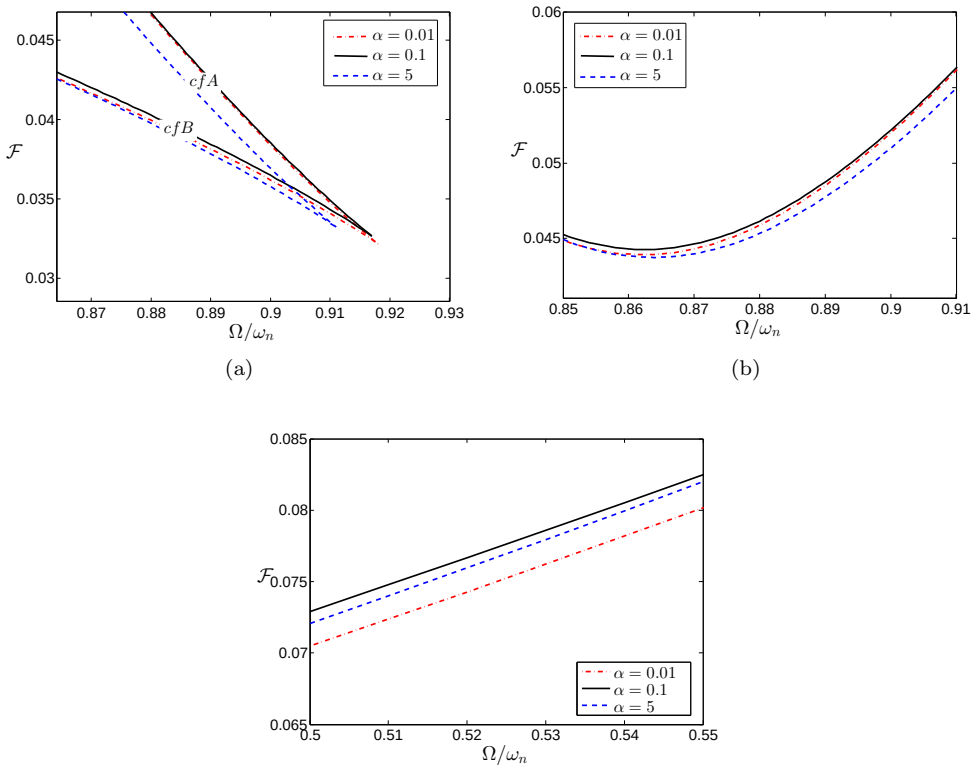

Figure 3.8: Effect of varying the time constant ratio, α on the loci of the (a) cyclic-fold bifurcation points of the intra-well oscillations, cfB and cfA, (b) period-doubling bifurcation point of the intra-well oscillations, *pd* and (c) cyclic-fold bifurcation point of the large-orbit inter-well oscillations, cfL. Results are obtained for $\zeta = 0.05$, $\delta = 0.5$, $r = 1.5$, and $\kappa^2 = 0.01$.

On the other hand, Fig. 3.9 shows that varying the coupling coefficient κ^2 has a notable impact on the critical forcing and frequency values at which the bifurcations of the oscillatory responses of a bi-stable harvester occur. Figure 3.9(a) shows that, for a given forcing, the cyclic-fold bifurcations of the resonant and non-resonant branch of intra-well oscillations, cfB and cfA respectively, occur at higher frequency ratios as κ^2 is increased from a nominal value of 0.01. This implies that the intra-well motions exist over a wider range of frequencies for higher electromechanical coupling due to the increase in the electric damping of the system. Figure 3.9(b) shows the effect of the electromechanical coupling on the period-doubling bifurcation of the resonant branch of intra-well oscillations, *pd*. Again, due to the increase in the electric damping, as κ^2 is increased, a higher forcing amplitude is required to initiate the period-doubling bifurcation. Figure 3.9(c) illustrates that the locus of the cyclic-fold bifurcation of the large-orbit inter-well oscillations, cfL, shifts up in the

forcing-frequency parameter space as the electromechanical coupling increases. As such, increasing the electromechanical coupling shrinks the frequency range over which the large-orbit solution exists.

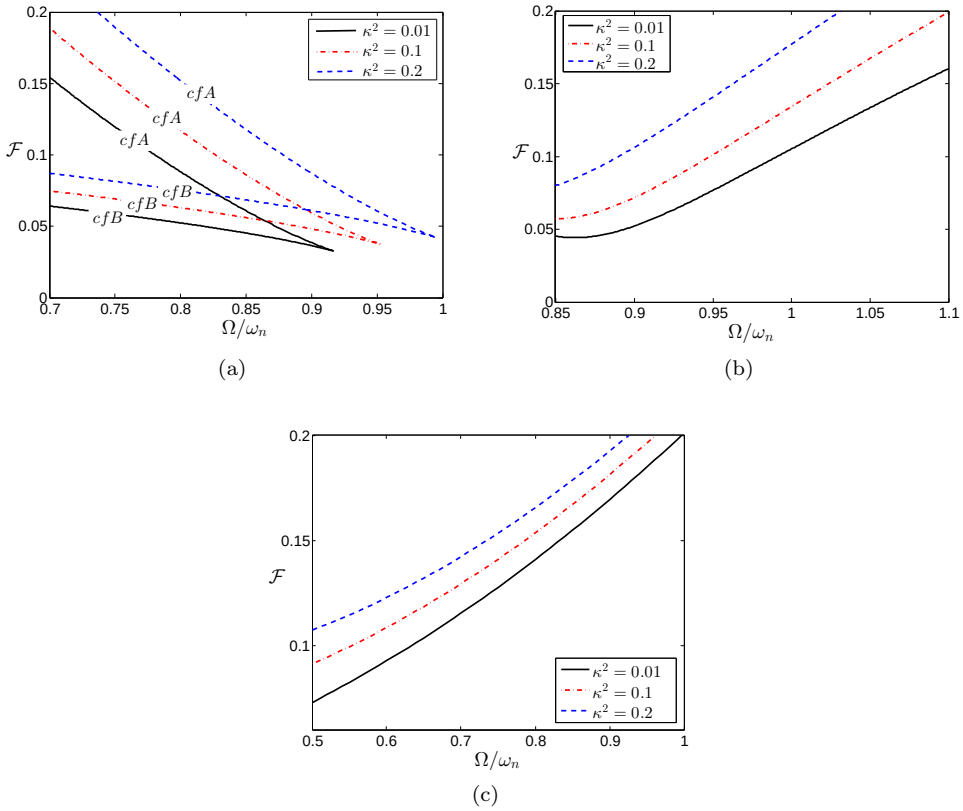

Figure 3.9: Effect of varying the electromechanical coupling coefficient, κ^2 on the loci of the (a) cyclic-fold bifurcation points of intra-well oscillations, cfB and cfA, (b) period-doubling bifurcation point of the intra-well oscillations, pd and (c) cyclic-fold bifurcation point of the large-orbit inter-well oscillations, cfL. Results are obtained for $\zeta = 0.05$, $\delta = 0.5$, $r = 1.5$, and $\alpha = 0.1$.

3.4 The Effective Bandwidth

We utilize the analytical expressions obtained in Section 3.3 to define an effective bandwidth for the bi-stable harvester by characterizing the different boundaries for intra- versus inter-well responses in the forcing-frequency parameters space. Figure 3.10 depicts a set of curves that demarcate three regions of particular importance. The first lies between three curves: the pd, the cfL, and the cfA curves and is denoted by CH on the figure. Force-frequency combinations in this region result

in either chaotic or n-period periodic motions where $n > 1$. The second region is located above the cfA and cfL curves and contains the desirable large-orbit inter-well motions, B_L. These motions can be unique or accompanied by chaotic or n-period periodic motions, where $n > 1$. Finally, the third region is located to the left of the cfA and cfL curves and contains the desirable large-orbit inter-well motions, B_L, always accompanied by the undesirable non-resonant intra-well motions, B_n. As such, depending on the initial conditions, the harvester can operate on either the large or small orbit branches of solution.

Figure 3.10 also shows three critical forcing levels. Any forcing magnitude below F_{cr1} only leads to the resonant branch of small-amplitude intra-well motions. Below this forcing level, no bifurcations occur and the voltage-frequency response exhibits the typical bell-shaped linear response within a single potential well. Above this critical forcing, the voltage response curve bends to the right as the bifurcations cfA and cfB appear. Above the critical forcing, F_{cr2}, the period-doubling bifurcation exists and more complex aperiodic responses begin to appear. Finally, above the critical forcing F_{cr3}, the large amplitude steady-state periodic inter-well motions begin to appear for the range of frequencies considered in the analysis.

With this understanding, the map shown in Fig. 3.10 can be used to provide a rough estimate of the effective bandwidth of the harvester. For a given set of design parameters it is possible to use this map to identify the forcing level and frequency bandwidth for which large-amplitude inter-well motions can be achieved either uniquely or with other less favorable motions.

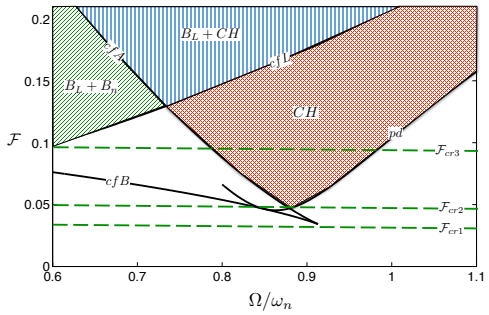

Figure 3.10: Bifurcation curves defining regions of intra- and inter-well responses. The curves are obtained for $\zeta = 0.05$, $\delta = 0.5$, $r = 1.5$, $\kappa^2 = 0.01$, $\alpha = 0.1$, and $\omega_n = 1$.

3.4.1 Influence of The Potential Shape

We use the understanding developed in this section to study the influence of the potential shape on the effective bandwidth of the harvester. The three different potential functions shown in Fig. 3.11 are considered. As shown in Fig. 3.12, in addition to the bifurcation curves obtained analytically, we superimpose a numerically obtained curve to define the region where the large amplitude inter-well periodic response, B_L is unique. By increasing r, the depth and separation distance between the potential wells increases requiring larger forcing magnitudes to initiate the inter-well oscillations. For $r = 1.1$, a minimum forcing of $\mathcal{F} = 0.022$ is necessary to achieve unique inter-well oscillations near $\Omega/\omega_n = 0.62$. When r is increased to $r = 1.5$, the minimum critical forcing increases dramatically to around 0.16 near $\Omega/\omega_n = 0.72$. Increasing r toward $r = 2$, further increases the critical forcing to around 0.375. In all cases, the bandwidth of frequencies over which the large inter-well oscillations branch uniquely exists increases as the forcing level is increased.

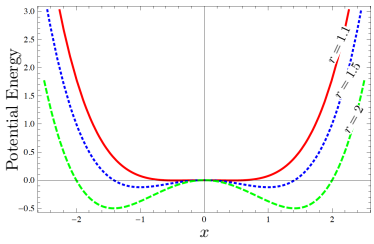

Figure 3.11: Potential function of the harvester for different values of r and $\delta = 0.5$.

By increasing the depth and separation distance between the potential wells, larger forcing levels become necessary to excite the desired periodic inter-well motions. Furthermore, the bandwidth of frequencies over which these solutions are unique shifts towards higher values making the potential energy function with the shallower wells more suitable for low-frequency excitations. Nevertheless, it should be borne in mind that, although the inter-well oscillations are activated at lower forcing values for shallower potential wells, the associated electric responses are generally much smaller relative to those obtained using deeper potential wells.

To illustrate this fact, the electric output obtained by operating the harvester on the large orbit branch of solutions, B_L, is compared for two different values of r, namely, $r = 1.1$ and $r = 1.5$ over the same range of forcing levels and frequency ratios. The comparison shown in Figures 3.13(a) and 3.13(b) reveals that, the overall amplitude of the response, y, is significantly lower when $r = 1.1$.

This result clearly demonstrates that, for a given forcing level, the improved bandwidth occurs at the expense of the amplitude of the electric output.

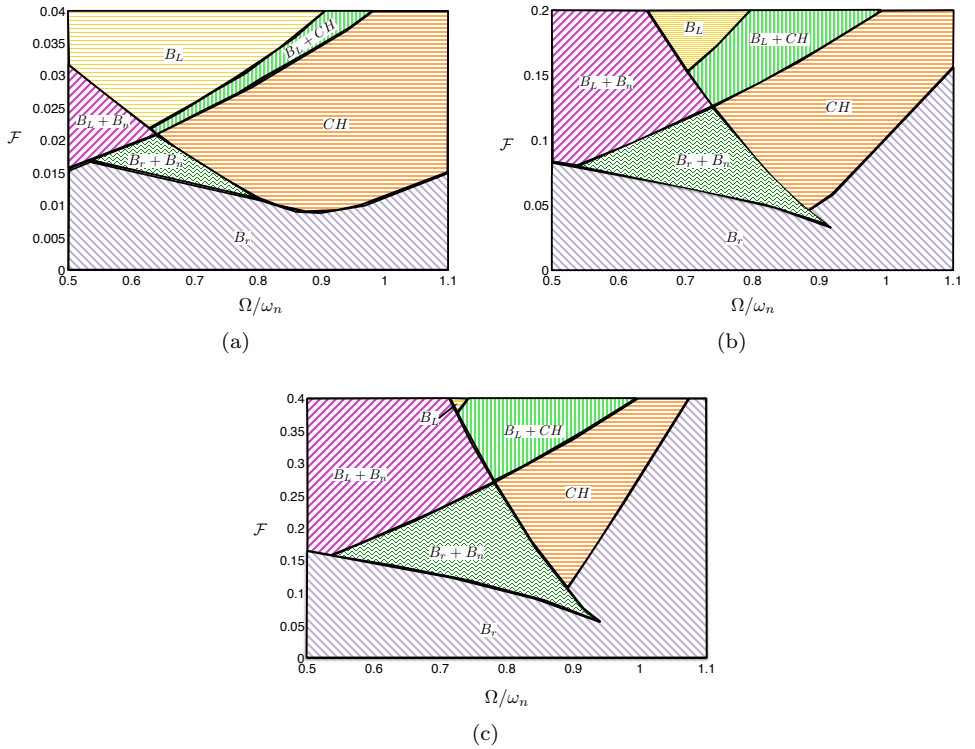

Figure 3.12: Comparison of bifurcation maps for different linear stiffness coefficients. B_L represents large orbit branch inter-well oscillations, B_n represents non-resonant intra-well oscillations, and CH represents chaotic solutions. Results are obtained for $\zeta = 0.05$, $\delta = 0.5$, $\kappa^2 = 0.01$, $\alpha = 0.1$ and (a) $r = 1.1$, (b) $r = 1.5$ and (c) $r = 2.0$.

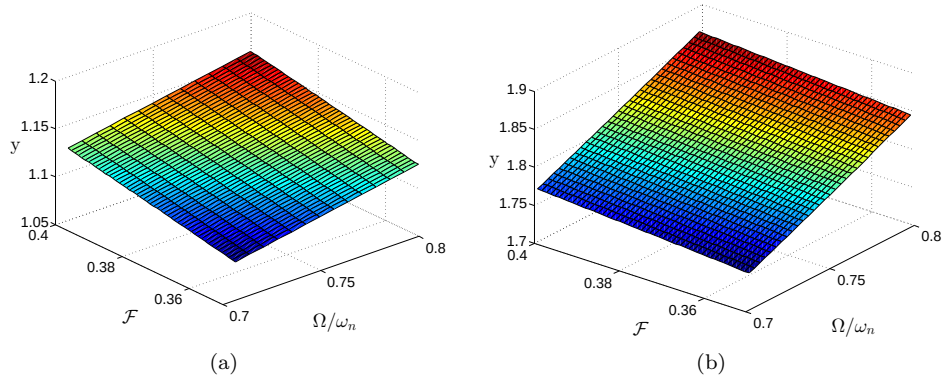

Figure 3.13: Comparison of electric outputs associated with the unique inter-well branch of solutions, B_L, for (a) $r = 1.1$ and (b) $r = 1.5$. Results are obtained for $\zeta = 0.05$, $\delta = 0.5$, $\kappa^2 = 0.01$ and $\alpha = 0.1$.

Chapter 4

Comparative Performance Analysis of Electrically-Optimized Mono- and Bi-stable Energy Harvesters

Unlike linear energy harvesters, where performance metrics have been established and are being easily implemented, the analysis of the performance of nonlinear energy harvesters is very difficult due to *i*) the presence of non-unique electric responses with competing basins of attractions, *ii*) the aperiodic nature of the output signals, and *iii*) the various qualitative variations of the dynamics, also knows as bifurcations, that can occur as one of the design parameters is varied as discussed in the previous chapter. As a result, a large number of research studies have been devoted to analyze the performance of these two classes of harvesters under various types of inputs including harmonic, non-stationary, and random excitations. A summary of these research findings can be found in [54].

Although many studies have characterized the response behavior of the mono- and bi-stable type of nonlinear VEHs separately, very few of them have actually compared their performance relative to one another. In one demonstration, Masana and Daqaq [7] considered a clamped-clamped axially-loaded beam type piezoelectric energy harvester capable of operating in both of the mono-stable (pre-buckling) and the bi-stable (post-buckling) configurations. They compared the output voltage in both configurations across an *arbitrarily* chosen electric load and found that the output

voltage has a complex dependence on the magnitude of base acceleration, the shape of the potential energy function, and the frequency of excitation. Such findings have been shown to facilitate the choice of the energy harvester configuration better suited for specific applications, especially when the frequency and magnitude of the excitation source are known.

The choice of an arbitrary electric load in the comparative performance analysis can yield inaccurate conclusions especially if the arbitrarily chosen load is close to the optimal load for some configuration but away from it for the other. As such, optimizing the electric load is an essential first step to deduce accurate conclusions about the relative performance. This can be very difficult for nonlinear VEHs especially those involving strong nonlinearities as in the case of the bi-stable harvester. Several studies have already addressed maximization of output power of VEHs by optimizing the electric load and/or the design parameters or by designing additional circuits [64, 65, 66, 67, 68]. For the most part, however, the models considered for the optimization problem are either linear, device specific, or do not draw a comparison of the relative power output of mono- and bi-stable VEHs.

This chapter compares the optimal power output of mono- and bi-stable energy harvesters in response to harmonic fixed-frequency excitations at the optimal electric load. Towards that end, a generic electromechanical model of a nonlinear VEH capable of operating in both configurations is considered. By utilizing the solutions from Chapter 3, analytical expressions that govern the steady-state periodic electric output responses for both configurations are obtained. Using these analytical expressions, the output power is optimized with respect to the time constant ratio between the mechanical and electrical subsystems. The resulting expressions are used to delineate the influence of the potential shape and the magnitude of excitation on the relative performance of the two configurations under optimal electric loading.

4.1 Basic Model

For the purpose of comparative performance analysis of mono- and bi-stable harvesters, we again consider the case when $\gamma = 0$ in Equation (2.4) to obtain,

$$\ddot{x} + 2\zeta\dot{x} + (1-r)x + \delta x^3 + \kappa^2 y = \mathcal{F}\cos(\Omega t), \tag{4.1a}$$

$$\dot{y} + \alpha y = \dot{x}, \tag{4.1b}$$

where the constant terms in Equation (4.1) are as described in Chapter 2. The harvester represented by Equation (4.1) can operate in the mono- and bi-stable configurations by simply altering the parameter r within the linear stiffness coefficient $1-r$. When $r < 1$, the harvester exhibits one stable equilibrium point given by the trivial solution, $x_s = 0$. In such a scenario, the harvester's oscillations are confined to a single global potential (*mono-stable configuration*) as shown in Fig. 4.1(a). On the other hand, as shown in Fig.4.1(b), when $r > 1$, the trivial solution ($x_s = 0$) becomes an unstable (saddle) and two nontrivial stable equilibria (nodes), $x_s = \pm\sqrt{\frac{(r-1)}{\delta}}$ are born causing the harvester to become of the bi-stable type.

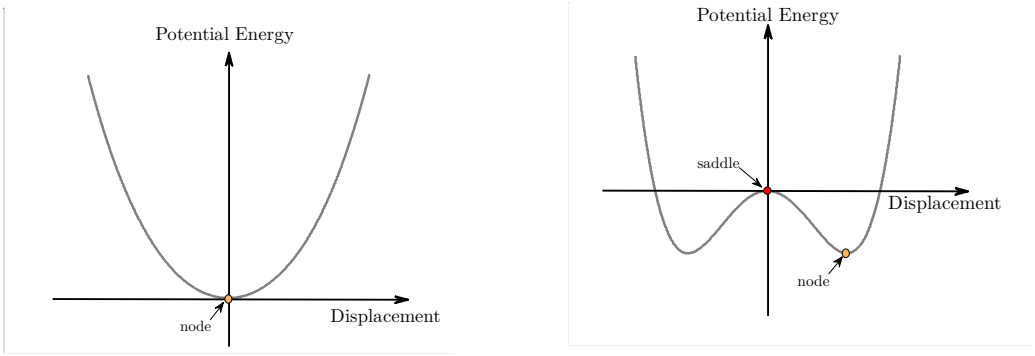

(a) (b)

Figure 4.1: Schematic of potential energy functions of the harvester in (a) mono-stable configuration and (b) bi-stable configuration.

The value of r not only affects the equilibrium solutions of the system but also influences the oscillation frequency around them. In order to obtain an expression for the local frequency of oscillation about a given equilibrium position, Equation (4.1) is linearized around the static equilibria (x_s, y_s). This yields

$$\ddot{x}_d + 2\zeta\dot{x}_d + \left[(1-r) + 3\delta x_s^2\right] x_d + \kappa^2 y_d = \mathcal{F}\cos(\Omega t), \tag{4.2a}$$

$$\dot{y}_d + \alpha y_d = \dot{x}_d, \tag{4.2b}$$

where $x_d = x - x_s$ and $y_d = y - y_s$. With that, the frequency of oscillations (short-circuit) around

a given equilibrium can be written as

$$\omega_n = \sqrt{(1-r) + 3\delta x_s^2}. \tag{4.3}$$

Figure 4.2 depicts how the (short-circuit) frequency of oscillation varies with the parameter r. As r is increased, the frequency decreases down to a theoretical value of 0 corresponding to the point at which the potential function transforms from mono- to the bi-stable configuration. For values of r beyond 1, the stiffness increases again, thereby increasing the frequency. This behavior permits tuning the harvester at equal frequencies for different configurations.

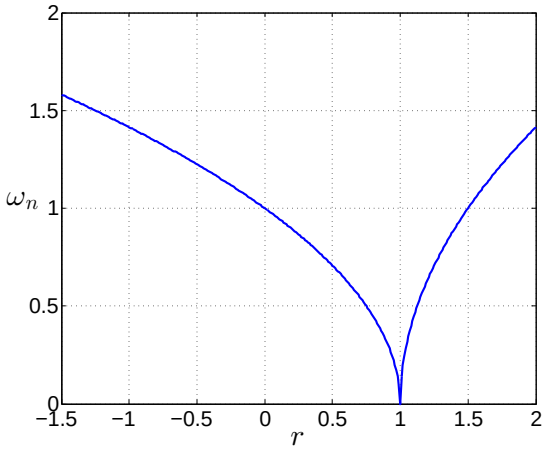

Figure 4.2: Variation of the (short circuit) oscillation frequency ω_n with the parameter r.

4.2 Analytical Solutions

As described earlier, mono-stable VEHs perform oscillations that are confined to a single potential well; while, bi-stable VEHs can perform intra-well (local) and inter-well (global) oscillations depending on the level of excitation. In this chapter, we are interested in the output power associated with the periodic responses of the harvester in both configurations. Towards that end, we use the solutions from Section 3.3.3 of Chapter 3 to analyze the periodic responses within the single potential well of the mono-stable configuration as well as the inter-well (global) oscillations of the bi-stable configuration. Next, we use the solutions obtained in Section 3.3.1 to approximate the intra-well (local) dynamics of the bi-stable configuration.

4.2.1 Global dynamics

As shown in Section 3.3.3 of the previous chapter, we implement the method of multiple scales on Equations (4.1)to obtain the second-order uniform approximate analytical solutions of the form

$$x(t) = a_0 \cos(\Omega t + \phi_0) + \tfrac{\delta a_0^3}{32\Omega^2} \cos(3\Omega t + 3\phi_0) + \mathcal{O}(\epsilon^2), \tag{4.4a}$$

$$y(t) = \tfrac{a_0\Omega}{\sqrt{\alpha^2+\Omega^2}} \cos(\Omega t + \phi_0 + \psi_1) + \tfrac{3\delta a_0^3}{32\Omega\sqrt{\alpha^2+9\Omega^2}} \cos(3\Omega t + 3\phi_0 + \psi_3) + \mathcal{O}(\epsilon^2) \tag{4.4b}$$

where the steady-state amplitude a_0 is governed by the following nonlinear frequency-response equation:

$$\zeta_{eff}^2 a_0^2 + \left[(\Omega^2 - (1-p) - \gamma_s)\frac{a_0}{2\Omega} - \frac{3\delta}{8\Omega} a_0^3\right]^2 = \frac{\mathcal{F}^2}{4\Omega^2}. \tag{4.5}$$

Here $\gamma_s = \kappa^2\Omega^2/(\alpha^2+\Omega^2)$, represents the linear shift in the system's natural frequency as a result of the electric coupling, $\zeta_{eff} = \zeta + \zeta_e$ represents the effective damping, $\zeta_e = \kappa^2\alpha/2(\alpha^2+\Omega^2)$ represents the electric damping, and

$$\phi_0 = \tan^{-1}\left(\frac{8\zeta_{eff}\Omega}{4(\Omega^2 - (1-r) - \gamma_s) - 3\delta a_0^2}\right), \qquad \psi_n = \tan^{-1}(\alpha/n\Omega). \tag{4.6}$$

Equation (4.5) can be solved analytically for the steady-state amplitude for any given forcing, $\mathcal{F}$, and frequency Ω. It is worth noting that the solutions obtained for $r < 1$ correspond to the harvester in the mono-stable configuration while those obtained for $r > 1$ represent the large amplitude inter-well oscillations in the bi-stable configuration.

4.2.2 Intra-well Dynamics

To study the responses within a single potential well of the bi-stable harvester ($r > 1$), we expand the dynamics about the stable nodes, $x_s = \pm\sqrt{\frac{(r-1)}{\delta}}$ and obtain Equations 3.3 as shown in the previous chapter. The solutions governing the steady-state periodic amplitude and electric responses are given by:

$$x_t(t) = a_0 \cos(\Omega t - \beta_0) + \tfrac{\tau}{2\omega_n^2}(-a_0^2 + \tfrac{1}{3}a_0^2\cos(2\Omega t - 2\beta_0)) + \ldots \tag{4.7a}$$

$$y(t) = \tfrac{\omega_n}{\sqrt{\alpha^2+\omega_n^2}} a_0 \cos(\Omega t - \beta_0 + \psi_1) + \tfrac{\tau}{3\omega_n\sqrt{\alpha^2+4\omega_n^2}} a_0^2 \cos(2\Omega t - 2\beta_0 + \psi_2) + \ldots, \tag{4.7b}$$

where the steady-state amplitude, a_0, is obtained by solving the following nonlinear frequency-response equation,

$$\zeta_{eff}^2 a_0^2 + \left[(\sigma - \gamma_s)a_0 - N_{eff}a_0^3\right]^2 = \frac{\mathcal{F}^2}{4\omega_n^2}. \tag{4.8}$$

Here, $\zeta_e = \frac{\kappa^2\alpha}{2(\alpha^2+\omega_n^2)}$ represents the electric damping, $N_{eff} = \frac{1}{\omega_n}\left[\frac{3}{8}\delta - \frac{5}{12}\frac{\tau^2}{\omega_n^2}\right]$ represents the effective nonlinearity coefficient, and $\gamma_s = \frac{\kappa^2\omega_n}{2(\alpha^2+\omega_n^2)}$ represents a linear shift in the system's natural frequency as a result of the electric coupling. The response phase can be written as

$$\beta_0 = \tan^{-1}\left(\frac{\zeta}{(\sigma-\gamma_s) - N_{eff}a_0^2}\right), \qquad \psi_n = \tan^{-1}\left(\frac{\alpha}{n\omega_n}\right). \tag{4.9}$$

4.2.3 Asymptotic Responses

Equations (4.5) and (4.8) are utilized to analytically construct the frequency-response curves of the harvester in the mono- and bi-stable configurations for two different forcing amplitudes. Figure 4.3 shows a comparison of the analytical results with the numerically obtained stroboscopic bifurcation maps for the mono-stable configuration. In general, results show very good agreement and also demonstrate the ability of the analytical solutions to predict the response amplitude and bifurcation points with relative accuracy.

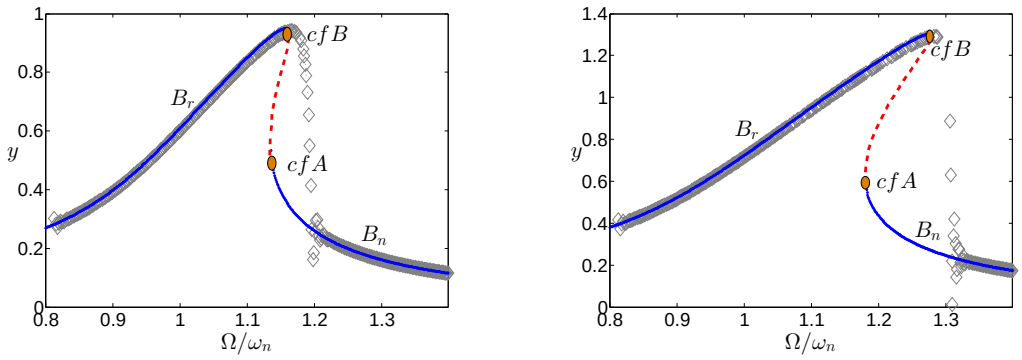

Figure 4.3: Comparison of numerical and analytical frequency responses of the mono-stable harvester. Gray curves represent numerical solutions and dashed lines represent unstable solutions. Results are obtained for $\zeta = 0.05$, $\delta = 0.5$, $r = 0.0$, $\kappa^2 = 0.01$, $\alpha = 0.1$, and normalized base excitation amplitudes (a) $\mathcal{F} = 0.11$, (b) $\mathcal{F} = 0.165$

Figure 4.3 further illustrates the traditional bending of the frequency-response curves (here

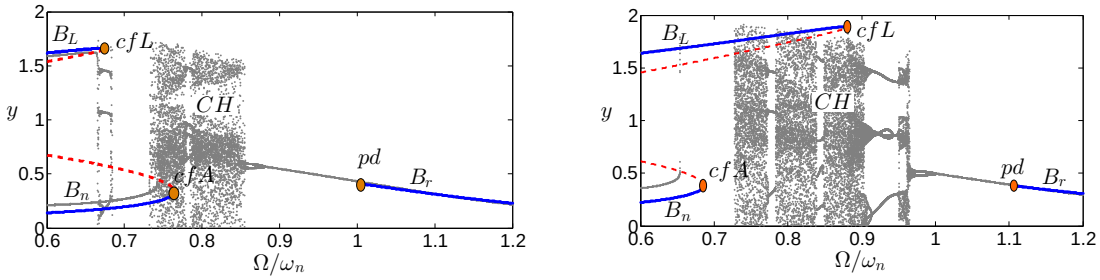

Figure 4.4: Comparison of numerical and analytical frequency responses of the bi-stable harvester. Gray curves represent numerical solutions and dashed lines represent unstable solutions. Results are obtained for $\zeta = 0.05$, $\delta = 0.5$, $r = 1.5$, $\kappa^2 = 0.01$, $\alpha = 0.1$, and normalized base excitation amplitudes (a) $\mathcal{F} = 0.11$, (b) $\mathcal{F} = 0.165$

to the right) because of the hardening type nonlinearity, $\delta > 0$. The response now contains three branches of solution: the resonant branch, B_r, the non-resonant branch, B_n, and the unstable branch (dashed lines). The resonant branch, B_r, which is desirable for energy harvesting because it provides larger amplitude voltages, is now accompanied by the non-resonant branch, B_n, for a portion of the frequency range considered. In this range, the final steady-state electric output of the harvester is determined by the initial conditions and the size of the competing basins of attraction for both solutions.

For the bi-stable case, Figs. 4.4(a) and 4.4(b) reveal much more complex intra- and inter-well responses. Here, in addition to the resonant and non-resonant branches of intra-well oscillations, B_r and B_n, respectively, a large-amplitude inter-well oscillations branch, denoted by B_L, appears in the lower range of frequencies. This branch, which is most desirable for energy harvesting, is accompanied by cross-well chaotic motion, (CH), and $n-$period periodic motions $(n > 1)$. By comparing Figs. 4.4(a) and 4.4(b) it becomes evident that when the forcing amplitude is increased, the desirable inter-well branch, B_L, extends over a wider range of frequencies while the intra-well branch, B_n, exists over a narrower band of frequencies. However, the B_L branch is still accompanied by less desirable responses over most of the frequency range considered.

4.3 Optimal Power

Using the expressions derived in the previous section, a general analytical expression for the output power associated with the periodic responses can be defined for both of the mono- and

bi-stable configurations as

$$P = \frac{\bar{P}}{P_0} = \alpha \left| y \right|^2 \tag{4.10}$$

where $|y|$ represents the steady-state amplitude of the electric output and $P_0 = k_1 \omega_n \kappa^2 l_c^2$. The power can then be optimized with respect to the time constant ratio, α, which is used as a measure of the influence of the electric load.

In the case of the global dynamics, the steady-state amplitude of the electric quantity y is given by Equation (3.35b). Substituting only the amplitude of the fundamental harmonic from Equation (3.35b) into Equation (4.10), the expression for the output power can be written as

$$P = \frac{\alpha \Omega^2}{\alpha^2 + \Omega^2} a_0^2, \tag{4.11}$$

where a_0 is the steady-state amplitude of the response obtained by solving Equation (3.31) analytically. Depending on the forcing and the excitation frequency, there exists one or three real valued solutions. The stability of these solutions can be determined by assessing the sign of the real part of the eigenvalues of the associated Jacobian matrix. It is evident from Equation (3.31) that, these solutions depend on the time constant ratio, α, through the electric damping, ζ_e, and the linear shift in the system's oscillation frequency, γ_s. Consequently, the output power can be expressed in terms of α by substituting the expression for a_0^2 into Equation (4.11). Using the resulting analytical expression, the optimal electric load, α_{opt}, can then be obtained by utilizing the conditions for the extremum, $\frac{dP}{d\alpha}|_{\alpha_{opt}} = 0$, $\frac{d^2P}{d\alpha^2}|_{\alpha_{opt}} < 0$. The corresponding theoretical maximum output power, P^*, is then given by

$$P^* = \frac{\alpha_{opt} \Omega^2}{\alpha_{opt}^2 + \Omega^2} a_{opt}^2. \tag{4.12}$$

where a_{opt}^2 is the steady-state amplitude at the optimal electric load, α_{opt}. It is worth reiterating that Equation (4.12) corresponds to the maximum power output associated with the oscillations within a single global potential well of a mono-stable harvester ($r < 1$) or the maximum power corresponding to the inter-well (global) oscillations of a bi-stable harvester ($r > 1$).

Next, we examine the maximum power attainable from the intra-well (local) oscillations within a single potential well of a bi-stable harvester. Towards that end, the amplitude of the electric quantity y from Equation (3.19b) is substituted into Equation (4.10) to obtain the expression of the

output power as

$$P = \frac{\alpha\omega_n^2}{\alpha^2 + \omega_n^2} a_0^2, \tag{4.13}$$

where a_0 is the steady-state amplitude obtained by solving Equation (3.18) analytically. Again, depending on the excitation level and frequency, Equation (3.18) may have one or three positive real valued solutions whose stability can be analyzed through the eigenvalues of the Jacobian matrix. The optimal electric load, α_{opt}, can be obtained by substituting the expression for a_0^2 into Equation (4.13) and finding the extremum of the resulting expression. This yields

$$P^* = \frac{\alpha_{opt}\omega_n^2}{\alpha_{opt}^2 + \omega_n^2} a_{opt}^2. \tag{4.14}$$

where a_{opt}^2 is the steady-state amplitude within a single potential well at the optimal electric load, α_{opt}.

4.4 Comparative Investigation

In this section, the analytical expressions for optimal power obtained previously are used to construct the optimal power versus frequency curves for both mono- and bi-stable configurations by including only the periodic responses. For the purpose of comparison, the linear stiffness is tuned by varying the parameter r such that the oscillation frequency in the mono-stable configuration is the same as that within a single potential well of the bi-stable configuration. One could argue that this is the ideal frequency to facilitate the transition of dynamic trajectories from a single well to inter-well motion in the bi-stable case.

In the mono-stable case ($r < 1$), increasing r results in the potential well becoming flatter and shallower. On the other hand, in the bi-stable case (values of $r > 1$), increasing r increases the depth and separation distance between the potential wells. We consider three different oscillation frequencies and their corresponding potential shapes for both configurations as shown in Fig. 4.5(a) and Fig. 4.5(b). Considering these cases permits studying the influence of the potential shape on the optimal output power, and, hence the relative performance in both configurations.

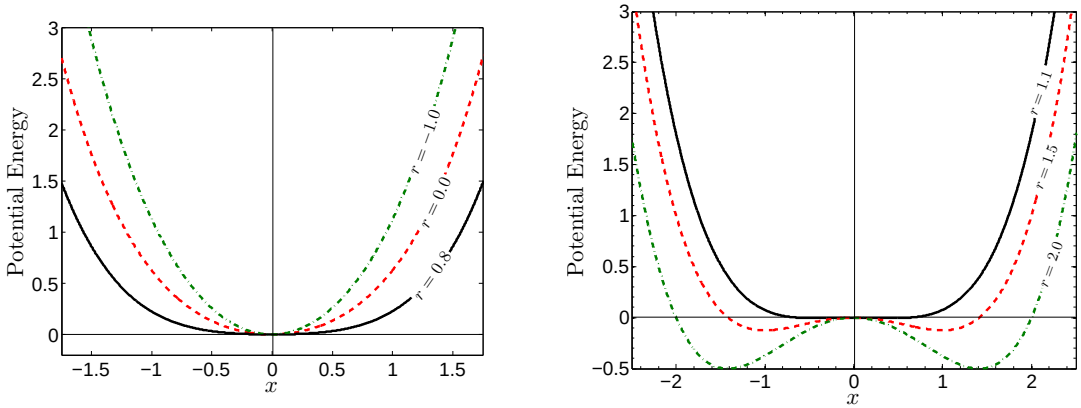

Figure 4.5: Shape of the potential functions for $\delta = 0.5$ and (a) $r < 1$ (mono-stable case) and (b) $r > 1$ (bi-stable case).

Optimal Power

Figure 4.6 depicts variation of the optimal power with the excitation frequency for the low stiffness scenario. Here, the values of the parameter r are chosen to be very close to the critical value of 1, i.e. $r = 0.8$ and $r = 1.1$ such that they result in the same non-dimensionalized oscillation frequency of 0.4472 for both configurations, see Fig. 4.2. For the purpose of comparison, the power curves are constructed for the same range of forcing in both configurations.

In the mono-stable case, the response curves exhibit the typical hardening-type characteristics with higher power levels occurring at frequency ratios larger than one. As the forcing is increased, the magnitude of the optimal power increases and is accompanied by a further extension of the resonant branch of solution towards higher frequency values. On the other hand, as shown in Fig. 4.6(b), in the bi-stable case, higher optimal output power levels occur at the lower end of the frequency range and extend up to the primary resonance region depending on the forcing level. These large-amplitude responses are always accompanied by the smaller-amplitude intra-well response branch which results in smaller output power level. However, as the forcing level is increased, the desirable large-amplitude branch extends over a wider range of frequencies while the less desirable intra-well branch shrinks.

A comparison between Figs. 4.6(a) and (b) illustrates that the power curves in both configurations are fairly similar as a result of the potential wells being similar in shape near the instability point ($r = 0.8$ versus $r = 1.1$). The optimal power levels are fairly similar with the notable dif-

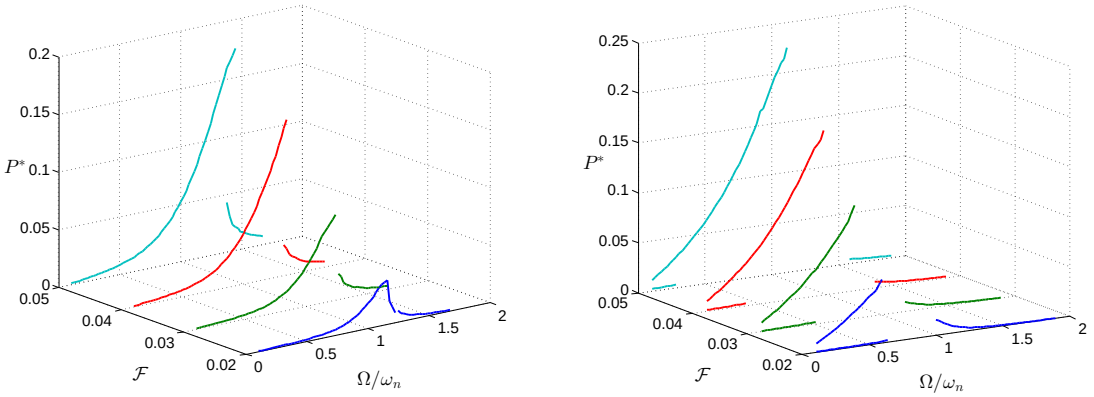

Figure 4.6: Optimal power-frequency response curves when the oscillation frequency is tuned to a non-dimensional value, $\omega_n = 0.4472$. Results are obtained for $\zeta = 0.05$, $\delta = 0.5$, $\kappa^2 = 0.01$, and (a) $r = 0.8$ (mono-stable), (b) $r = 1.1$ (bi-stable)

ference between the two configurations being in the slope of the power curves. As the frequency is increased, the mono-stable optimal power curves show a more dramatic increase in amplitude in the vicinity of the primary resonance while the bi-stable curves show relatively higher amplitudes at low frequencies that steadily increase with an increase in frequency. It is also worth noting that the forcing levels needed to activate large-amplitude inter-well responses in the bi-stable case are relatively small owing to the shallow potential wells as shown in Fig. 4.5(b).

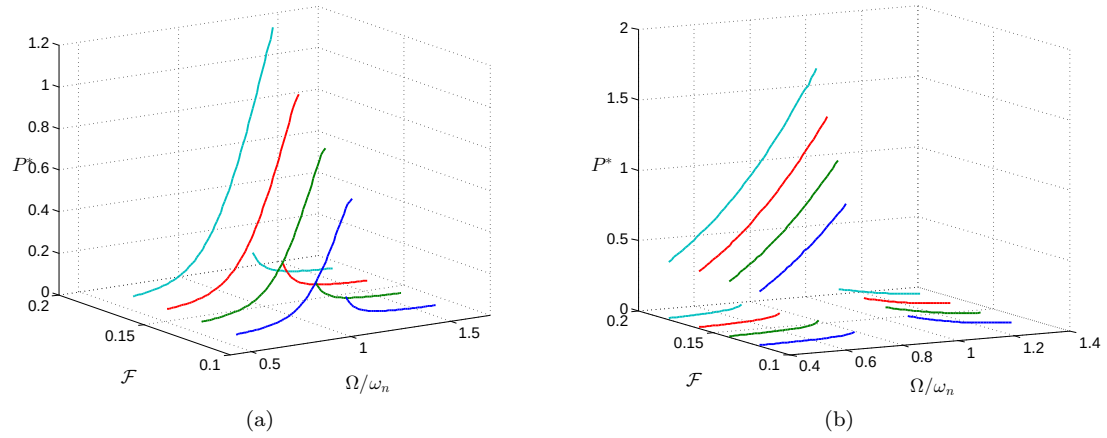

Figure 4.7: Optimal power-frequency response curves when the oscillation frequency is tuned to a non-dimensional value, $\omega_n = 1$. Results are obtained for $\zeta = 0.05$, $\delta = 0.5$, $\kappa^2 = 0.01$, and (a) $r = 0.0$ (mono-stable), (b) $r = 1.5$ (bi-stable)

When the value of r is changed to $r = 0.0$ and $r = 1.5$ for the mono- and bi-stable configurations, respectively, there is an increase in stiffness and a resulting increase in the oscillation frequency of the harvester. As shown in Fig. 4.7(a) and Fig. 4.7(b), this increase in stiffness results in an increase in the magnitude of the optimal output power. The behavior of the power curves in the mono-stable case remains the same with the power increasing sharply around the frequency ratio close to resonance ($\Omega/\omega_n = 1$) and reaching its maximum magnitude slightly above resonance. In comparison, the optimal power in the bi-stable configuration is larger in magnitude and the response curves again indicate that maximum power levels occur near the lower end of the frequency range considered ($\Omega/\omega_n \approx 0.4$). However, these desirable large-amplitude responses are always accompanied by the small-amplitude intra-well power curves.

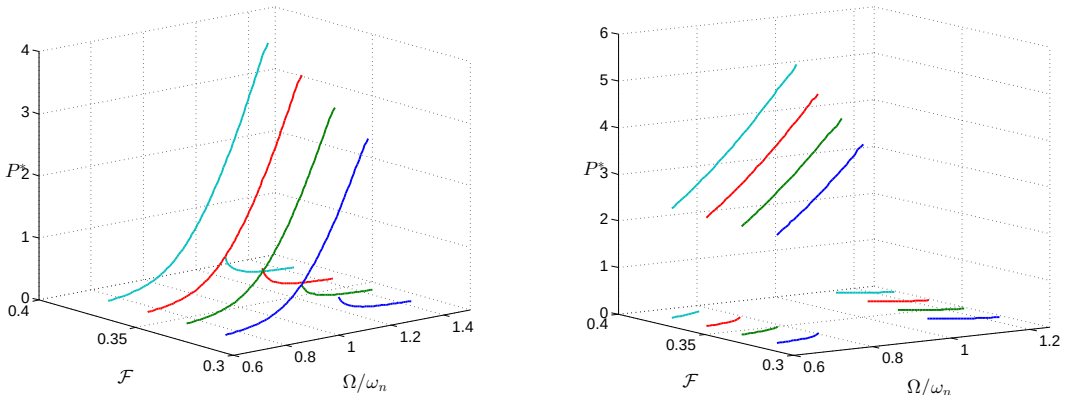

Figure 4.8: Optimal power-frequency response curves when the oscillation frequency is tuned to a non-dimensional value, $\omega_n = 1.4142$. Results are obtained for $\zeta = 0.05$, $\delta = 0.5$, $\kappa^2 = 0.01$, and (a) $r = -1.0$ (mono-stable), (b) $r = 2.0$ (bi-stable)

Figures 4.8(a) and (b) depict the optimal power curves when the stiffness is increased further by using $r = -1.0$ for the mono-stable configuration and $r = 2.0$ for the bi-stable case. The response behavior in both configurations remains largely the same with the only notable difference being in the magnitude of the output power. Again, the bi-stable harvester shows significantly higher magnitudes of power in the low frequency range when compared to the mono-stable one and this extends to the region of the primary resonance depending on the forcing amplitude. On the other hand, the mono-stable harvester exhibits the largest magnitude of optimal power at frequency ratios much higher than the primary resonance owing to the hardening-type nonlinearity.

The aforedescribed comparison suggests that, when optimized, the harvester in the bi-stable configuration provides larger periodic steady-state voltages as compared to the mono-stable one for the three different potential shapes considered. The optimal power output is relatively higher over a wider range of frequencies in the bi-stable case as compared to the mono-stable one for the same range of frequencies and forcing amplitudes. This can be attributed to the activation of the large-amplitude inter-well responses in the bi-stable configuration and the optimization of the electric load which results in higher power output in all cases. Nevertheless, it should be borne in mind that the these inter-well responses are not unique and can coexist with the small-amplitude intra-well responses and other aperiodic or chaotic oscillations not shown here. Depending on initial conditions, the responses in the bi-stable configuration may be of the small-amplitude periodic, aperiodic or chaotic type which can cause the output power to drop ([7]). It is observed that the dimensional power versus frequency response curves in both configurations follow trends similar to those discussed in this section for all cases of the potential shapes considered. This permits comparison of the power output of mono- and bi-stable harvesters based on the trends of the non-dimensional power curves.

It is worth mentioning that the results presented here are valid for a constant value of the electromechanical coupling coefficient ($\kappa^2 = 0.01$). In general, for nonlinear VEHs, increasing the coupling coefficient increases the electrically induced damping in these devices which reduces the maximum amplitude of the response, thereby reducing their output power [54]. There exists an optimal value of κ beyond which the electrical damping becomes too large and the power output of the harvester drops. In this work, we limit the analysis to optimization of the power with respect to the electrical load. Consequently, the effect of variation in the electromechanical coupling on the output power is not considered.

Optimal Electric Load

Unlike linear energy harvesters that have a constant optimal electric load, the problem of optimizing nonlinear energy harvesters yields an electric load which varies with the excitation frequency. In this section, we study variation of the optimal load embedded within, α_{opt}, at each frequency for both of the mono- and bi-stable configurations. This permits drawing conclusions regarding the magnitude of α_{opt} and the feasibility of tuning the load more easily in one configuration versus the other.

Figures 4.9(a) and 4.9(b) depict variation of α_{opt} with the frequency of excitation for different

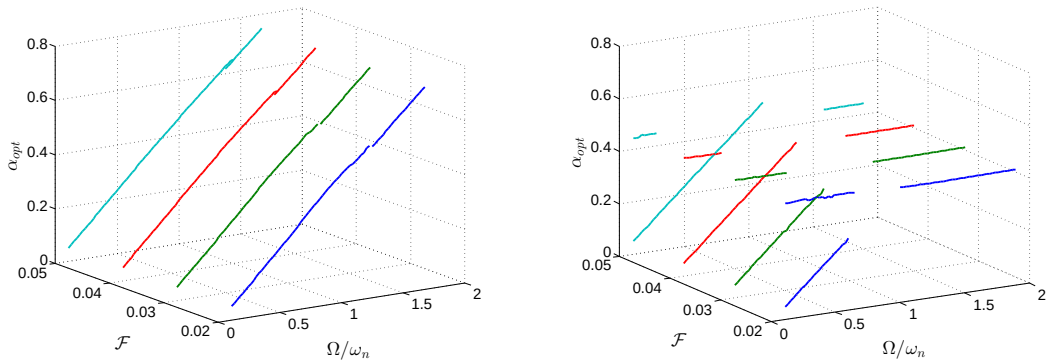

Figure 4.9: Variation of the optimum electric load, α_{opt}, with the ratio between the excitation frequency and linear natural frequency, Ω/ω_n. Results are obtained for $\zeta = 0.05$, $\delta = 0.5$, $\kappa^2 = 0.01$, and (a) $r = 0.8$ (mono-stable), (b) $r = 1.1$ (bi-stable)

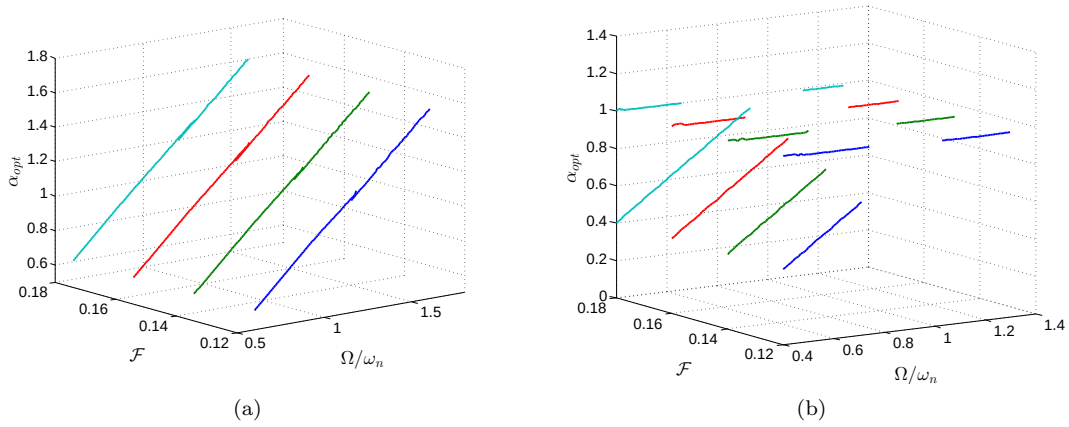

Figure 4.10: Variation of the optimum electric load, α_{opt}, with the ratio between the excitation frequency and linear natural frequency, Ω/ω_n. Results are obtained for $\zeta = 0.05$, $\delta = 0.5$, $\kappa^2 = 0.01$, and (a) $r = 0.0$ (mono-stable), (b) $r = 1.5$ (bi-stable)

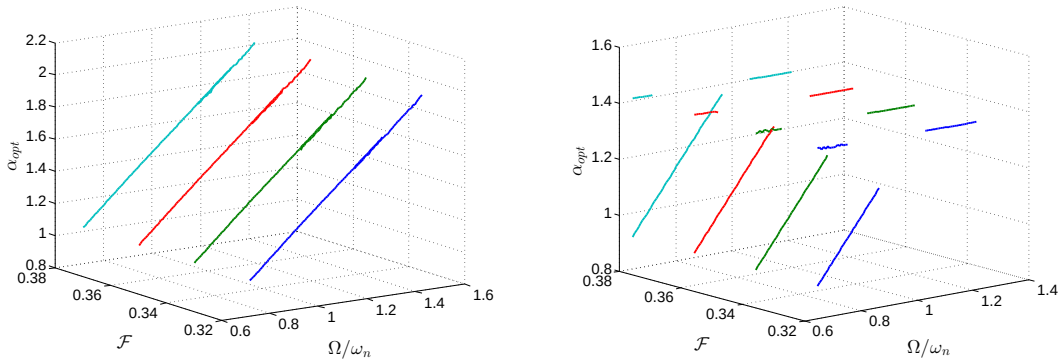

(a) (b)

Figure 4.11: Variation of the optimum electric load, α_{opt}, with the ratio between the excitation frequency and linear natural frequency, Ω/ω_n. Results are obtained for $\zeta = 0.05$, $\delta = 0.5$, $\kappa^2 = 0.01$, and (a) $r = -1.0$ (mono-stable), (b) $r = 2.0$ (bi-stable)

forcing amplitudes. These curves correspond to the optimal power curves shown in Fig. 4.6, when the harvester is tuned to have a relatively low oscillation frequency. For the mono-stable case, Fig. 4.9(a), it can be seen that the optimal value of electric load increases linearly with the excitation frequency for the resonant and the non-resonant branches of output power. Similarly, as shown in Fig. 4.9(b) for the bi-stable case, the values of α_{opt} corresponding to the large output power (due to inter-well responses) also increase linearly with the frequency. As such, α_{opt} associated with the optimal power from the global oscillations of the harvester is equal to the excitation frequency, Ω. However, the values of α_{opt} corresponding to the intra-well branch do not vary appreciably with the excitation frequency. This can be attributed to the fact that the value of the optimal electric load for the intra-well branch is determined by utilizing Equation (4.13). This approximate analytical expression is obtained considering the excitation frequency, Ω, to be very close to the local oscillation frequency, ω_n, which erroneously predicts that the maximum value of the power occurs when α_{opt} is tuned to the natural frequency. However, since from an energy harvesting perspective, it is more desirable to operate on the inter-well branch of solutions, it is preferable to tune α_{opt} to the excitation frequency. Furthermore, it is evident from the figures that the forcing amplitude has very little influence on the optimal value of the electric load in both cases.

Similar trends are observed for the two instances when the harvester is tuned to have higher stiffness and, thereby, higher oscillation frequencies as seen in Figs. 4.10 and 4.11. Again, the optimal electric load associated with the global dynamics increases linearly with frequency while

that corresponding to the local dynamics is constant.

A comparative analysis of the α_{opt} curves for of the both mono- and bi-stable configurations does not indicate a clear advantage in the ability to tune the optimal electric load more easily in one configuration versus the other. As such, for both configurations, the optimal time constant ratio should be tuned such that it is close to the excitation frequency.

Chapter 5

Investigation of a Tri-stable Oscillator for Energy Harvesting Under Harmonic Excitations

Although vibratory energy harvesting has taken significant strides in the last couple of years, there are some limitations and issues particularly related to the performance of nonlinear VEHs. It has been shown in the literature that nonlinear bi-stable VEHs can produce large output voltages over a wide range of frequencies owing to the activation of the large-orbit inter-well oscillations [3, 5, 7, 48]. However, as demonstrated in Chapter 3, depending on the shape of the potential function, there is a threshold value of the excitation level below which is it is not possible to activate the desirable inter-well dynamics. If the harvester is designed such that it possesses shallow potential wells, there is a decrease in the excitation level necessary to activate oscillations desirable for energy harvesting. Nevertheless, the associated electric output responses of the harvester are generally small in amplitude. This poses a challenge in designing these devices, especially when the magnitude and nature of excitation are unknown.

This has driven researchers to explore newer designs of nonlinear VEHs that are capable of producing sustained large-amplitude electric responses. In one demonstration, Zhou et. al [8, 53, 72] consider a tri-stable piezolectric energy harvester which consists of a cantilever beam with a tip magnet oscillating between two stationary magnets much like the earlier designs of the bi-stable VEHs

adopted in [3, 5, 40]. However, they show that for a certain orientation and separation distance between the two stationary magnets, the harvester exhibits a tri-stable configuration. The preliminary experiments and numerical simulations presented in their work illustrate that the tri-stable harvester produces higher voltage outputs as compared to the bi-stable one over a wider frequency range even for low-amplitude base excitations. However, their study is limited to numerical and experimental investigations and does not include the effect of design parameters on the response of such devices. Further, their study does not analyze the qualitative variations in the dynamic response characteristics of tri-stable VEHs. In this chapter, the generic electromechanical model presented in Chapter 2 is used to model the dynamics of a tri-stable nonlinear VEH. Using perturbation techniques, namely, the method of multiple scales, analytical expressions describing the steady-state periodic responses of the tri-stable harvester to harmonic excitations are derived. These expressions are then used to construct frequency-response curves that are validated against numerical findings. The analytical solutions are also used to study key bifurcations that directly affect the effective frequency bandwidth of tri-stable VEHs. An experimental study is carried out to investigate the validity of the model in predicting the dynamic responses of the tri-stable system.

5.1 Basic Mathematical Model

To model the dynamics of a tri-stable VEH, we consider the case when $\gamma > 0$ in the generic nonlinear electromechanical model given by Equation (2.4) to obtain,

$$\ddot{x} + 2\zeta\dot{x} + (1-r)x + \delta x^3 + \gamma x^5 + \kappa^2 y = \mathcal{F}\cos(\Omega t), \tag{5.1a}$$

$$\dot{y} + \alpha y = \dot{x}, \tag{5.1b}$$

where the constant terms are as described in Chapter 2. Since this analysis is focused on tri-stable VEHs, we limit our attention to the case when $r < 1$, $\delta < 0$ and $\gamma > 0$. In this scenario, the potential energy function is tri-stable and exhibits the following equilibria as shown in Fig. 5.1

$$x_s = 0, \qquad x_s = \pm\sqrt{\frac{-\delta \pm \sqrt{\delta^2 - 4(1-r)\gamma}}{2\gamma}}. \tag{5.2}$$

When $\delta^2 - 4(1-r)\gamma < 0$ in Equation (5.2), only the trivial solution, $x_s = 0$, exists and the system is mono-stable. On the other hand, when $\delta^2 - 4(1-r)\gamma > 0$, four non-trivial solutions are born. Of the four solutions, two of them at $x_s = \pm\sqrt{\frac{-\delta+\sqrt{\delta^2-4(1-r)\gamma}}{2\gamma}}$ represent stable equilibrium solutions (nodes) while the other two at $x_s = \pm\sqrt{\frac{-\delta-\sqrt{\delta^2-4(1-r)\gamma}}{2\gamma}}$, represent unstable saddles.

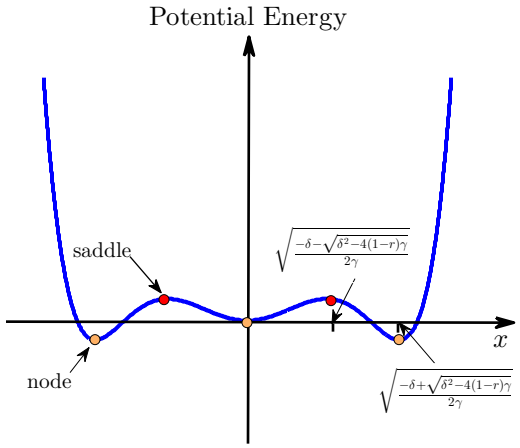

Figure 5.1: Tri-stable potential energy function.

It can be seen from Fig. 5.1 that, the two potential wells associated with the equilibria at $x_s = \pm\sqrt{\frac{-\delta+\sqrt{\delta^2-4(1-r)\gamma}}{2\gamma}}$ are symmetric and separated by the potential well associated with the trivial equilibrium, $x_s = 0$. The depth and separation distance between the two symmetric potential wells and the depth of the middle potential well can be varied by varying the linear and nonlinear stiffness coefficients, namely, r, δ and γ. These coefficients not only affect the system's equilibria but also influence the frequency of oscillations around them.

In order to obtain an expression of the local oscillation frequency of the harvester around a given equilibrium, Equation (5.1) is linearized around the static equilibria, (x_s, y_s), to obtain

$$\ddot{x}_d + 2\zeta\dot{x}_d + \left[(1-r) + 3\delta x_s^2 + 5\gamma x_s^4\right] x_d + \kappa^2 y_d = \mathcal{F}\cos(\Omega t), \tag{5.3a}$$

$$\dot{y}_d + \alpha y_d = \dot{x}_d, \tag{5.3b}$$

where $x_d = x - x_s$ and $y_d = y - y_s$. The frequency of oscillations (short-circuit) around a given equilibrium can then be written as

$$\omega_n = \sqrt{(1-r) + 3\delta x_s^2 + 5\gamma x_s^4}. \tag{5.4}$$

When $x_s = 0$, the above expression represents the oscillation frequency within the central potential well. On the other hand, for the non-trivial solutions, Equation (5.4) represents the oscillation frequency within one of the symmetric outer potential wells. As such, there are two local oscillation frequencies for a symmetric tri-stable harvester associated with each of the trivial and non-trivial equilibrium solutions.

5.2 Response to Harmonic Excitations

Nonlinear VEHs, particularly of the bi-stable type, exhibit large amplitude (inter-well) responses under harmonic inputs depending on the frequency and amplitude of excitation [3, 6]. However, it is illustrated that these responses which are favorable for energy harvesting, cannot be uniquely realized over a wide range of frequencies and are often accompanied by less desirable small amplitude (intra-well), $n-$period, and chaotic responses [73]. In the case of a tri-stable VEH, the higher-order nonlinearities result in more complex dynamic responses further exacerbating the problem of uniquely realizing large-amplitude responses. To further illustrate this issue, Equations (5.1a) and (5.1b) are numerically integrated to construct bifurcation diagrams of the frequency-response of the electric output for different excitation amplitudes as depicted in Fig. 5.2. As shown in Fig. 5.2(a), for a small excitation amplitude, $\mathcal{F} = 0.025$, depending on the initial conditions and the direction of the frequency sweep, the dynamic trajectories remain confined to either one of the symmetric outer potential wells or to the middle potential well because the excitation is not large enough for them to overcome the potential barriers. There are four branches of solutions, namely B_{r1}, B_{n1}, B_{r2} and B_{n2}. The branches B_{r1} and B_{n1} represent the resonant and the non-resonant branches of solution within the middle potential well, respectively. Within this potential well, the frequency response is of the softening nature with the large-amplitude resonant branch of oscillations, B_{r1}, occurring at frequencies smaller than the local resonance frequency, $\omega_1 = 0.7071$. The other two branches of solutions, B_{r2} and B_{n2}, represent respectively, the resonant and non-resonant branches of solution within one of the outer potential wells. Again, it is observed that the frequency response is of the softening nature with large-amplitude responses occurring at lower frequencies than the local resonance frequency, $\omega_2 = 1.1412$.

Figure 5.2(a) also illustrates that, the response curves undergo four bifurcations: the first occurs as the frequency is increased and the non-resonant branch associated with the middle potential

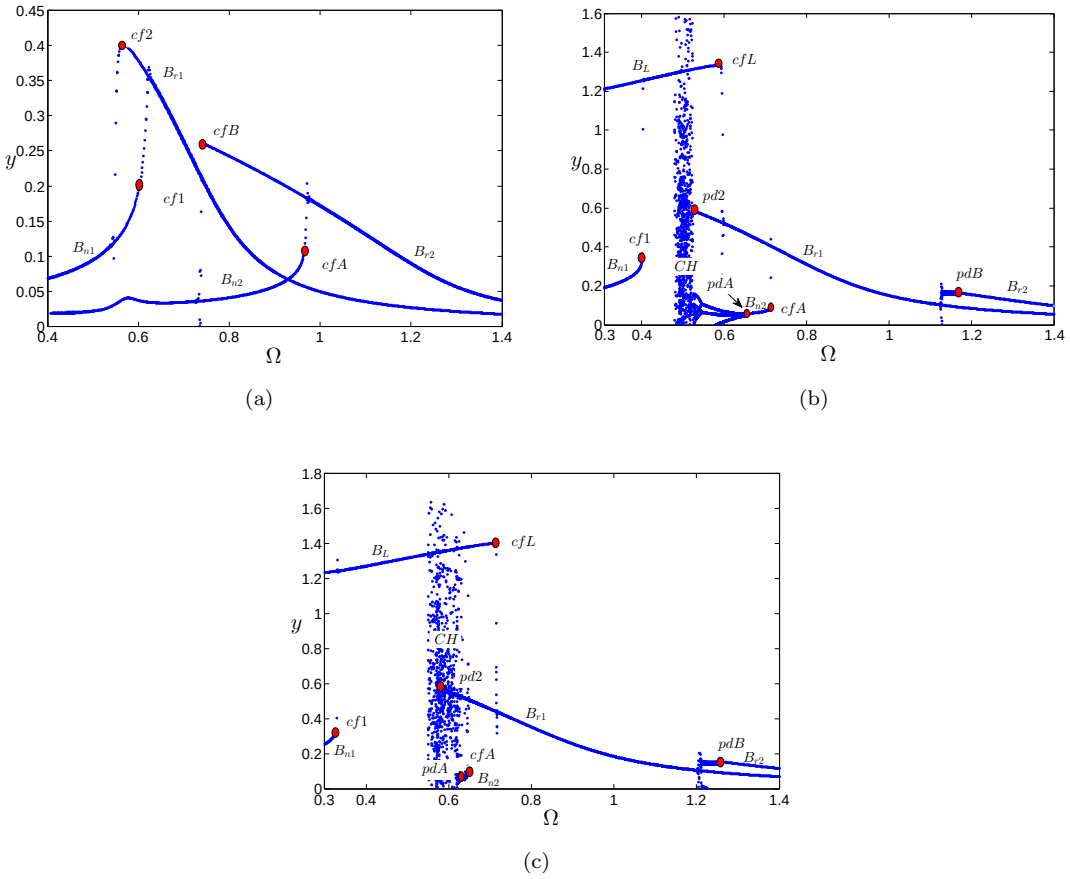

Figure 5.2: Frequency-response curves for a tri-stable harvester at three different excitation levels. Results are obtained using Equation (5.1) with $\zeta = 0.05$, $r = 0.5$, $\delta = -1.5$, $\gamma = 0.95$, $\kappa^2 = 0.01$, $\alpha = 0.1$, $\omega_1 = 0.7071$, $\omega_2 = 1.1412$ and base excitations of normalized amplitudes (a) $\mathcal{F} = 0.025$, (b) $\mathcal{F} = 0.08$ and (c) $\mathcal{F} = 0.1$

well, B_{n1}, loses stability through a cyclic-fold bifurcation, $cf1$, giving way to the resonant branch, B_{r1}. The second also occurs as the frequency is increased and branch B_{n2} undergoes a cyclic-fold bifurcation, cfA, giving way to the resonant branch of intra-well oscillations, B_{r2}. The third bifurcation occurs as the frequency is decreased and the resonant branch B_{r1} loses stability through a cyclic-fold bifurcation $cf2$, giving way to either of the non-resonant branch of solutions, B_{n1} or B_{n2}. The final bifurcation occurs on the resonant branch of solution associated with the outer potential well, B_{r2}. As the frequency is decreased, this branch undergoes a cyclic-fold bifurcation, cfB, giving way to either resonant solutions on branch, B_{r1}, or to non-resonant solutions on branch, B_{n2}. It is worth emphasizing that, depending on the initial conditions and the direction of sweep, the harvester can exhibit any of the aforementioned periodic responses for a given frequency.

As shown in Fig. 5.2(b), when the excitation amplitude is increased to $\mathcal{F} = 0.08$, a large-amplitude branch of solutions, B_L, now appears at the lower end of the frequency range considered. This branch represents the large-amplitude periodic inter-well responses that occur between the two outer potential wells. As the frequency is increased, this large amplitude branch disappears in a cyclic-fold bifurcation, cfL, and gives way to either the resonant branch within the middle potential well, B_{r1} or the non-resonant branch of solution in the symmetric outer potential well, B_{n2}. It can be clearly seen that, as with the bi-stable harvester, the B_L branch of solution is not unique and coexists with smaller (non-resonant) branches (B_{n1} and B_{n2}) and a mixture of intra- and inter-well chaotic motions CH at certain frequency values.

As the frequency is decreased from higher to lower values, the harvester exhibits periodic responses that correspond to the resonant branches of solution, B_{r1} or B_{r2}, again depending on the initial conditions. It is noted that the cyclic fold bifurcation, cfB, occurring on the resonant intra-well branch, B_{r2}, disappears and is replaced by the period doubling bifurcation, pdB. As the frequency is decreased, the period doubling causes the B_{r2} branch of solution to give way to the the solution B_{r1}. It is also noted that, the cyclic-fold bifurcation $cf2$ occurring on the resonant branch B_{r1}, is now replaced by a period-doubling bifurcation, $pd2$. Furthermore, the non-resonant branch of solutions associated with the outer potential well, B_{n2}, undergoes a period doubling bifurcation, pdA and when the frequency is decreased further, a cascade of period-doubling bifurcations occurs resulting in a window of intra- and inter-well chaotic responses, CH, which disappears in a boundary crisis.

When the amplitude of excitation is increased further to $\mathcal{F} = 0.1$, as observed in Fig. 5.2(c), several distinct behaviors are noted in the frequency response. It is observed that, *i*) The cfL bifurcation occurs at a higher value of the excitation frequency implying that the desired large-amplitude inter-well branch of oscillations extends over a wider frequency range; *ii*) the cyclic-fold bifurcation, $cf1$ of the non-resonant branch, B_{n1}, occurs at a lower value of the frequency meaning that the jump from the non-resonant branch to the desired large-amplitude oscillations can now occur at lower frequency values, *iii*) the cyclic-fold bifurcation, cfA, and the period-doubling bifurcation, pdA, of the non-resonant intra-well branch of oscillations, B_{n2}, occur at lower frequencies and at values that are very close to each other. This implies that the range of frequencies over which the non-resonant branch, B_{n2}, exists, shrinks, and *iv*) the period-doubling bifurcations, $pd2$ and pdB, of the resonant branches of intra-well oscillations occur at higher frequency values, meaning that

complex intra- and inter-well responses can now be initiated at larger excitation frequencies.

As in the case of bi-stable harvesters, the numerical analysis indicates that there are four critical bifurcations in the frequency-response curves shown above, that can be used to approximate the bandwidth of tri-stable energy harvesters for a given forcing. These bifurcations are,

1. The cyclic-fold bifurcation, cfL. As in the case of bi-stable VEHs, this bifurcation defines how far the large amplitude inter-well branch of oscillations extends in the frequency domain. The larger the value of the frequency at which cfL occurs, the larger the range of frequencies over which this branch of solution extends. If the frequency at which cfL occurs is smaller than that associated with $cf1$, the large amplitude inter-well responses can never be unique in the frequency domain. Furthermore, if the frequency at which cfL occurs is larger than either one of the period doubling bifurcations, pdA or $pd2$, there is a larger chance that the desired large-amplitude inter-well oscillations are accompanied by aperiodic oscillations.

2. The cyclic-fold bifurcation, $cf1$. This bifurcation defines the range of frequencies over which the non-resonant branch of intra-well oscillations (*oscillations within the central potential well*), B_{n1}, exists in the frequency domain. The lower the frequency value at which $cf1$ occurs, the better.

3. The period-doubling bifurcations, $pd2$ and pdA. The bifurcation $pd2$ represents the minimum value of the excitation frequency for which the resonant branch of intra-well solutions (*oscillations within the central potential well*), B_{r1}, is periodic. On the other hand, pdA represents the value of frequency for which the non-resonant branch of intra-well solutions (*oscillations within the outer potential wells*), B_{n2}. At excitation frequencies below these values, more complex intra- and inter-well dynamic responses can be initiated. The larger the value of frequencies at which the aforedescribed period-doubling bifurcations occur, the larger the bandwidth over which the large-amplitude responses can be realized.

The numerical analysis also shows the cyclic-fold bifurcations, cfA and cfB, and the period-doubling bifurcation pdB that define how far the resonant and non-resonant branch of oscillations, B_{r2} and B_{n2}, extend in the frequency domain. These bifurcations also provide further insights into the response behavior of the harvester, thereby facilitating efficient designs for a given forcing level. In what follows, we obtain approximate solutions that govern the steady-state periodic responses of

the tri-stable VEH described by Equation (5.1). Using these solutions, we derive expressions for the aforementioned bifurcations and study how their loci vary in the force-frequency parameter space.

5.3 Approximate Analytical Solutions

We first derive analytical expressions for the steady-state periodic responses of the displacement and electric output associated with the intra-well oscillations within the symmetric outer potential wells. Subsequently, we obtain expressions that approximate the periodic responses associated with the large-orbit inter-well oscillations between the outer potential wells. Finally, we obtain solutions to approximate the intra-well dynamics around the trivial equilibrium solution (oscillations in the middle potential well).

5.3.1 Dynamics around the non-trivial equilibria

In this section, we are interested in finding expressions that govern the dynamics around the non-trivial equilibria. To this end, we expand the dynamics about the stable nodes by introducing $x_t = x - x_s$ in Equations (5.1a) and (5.1b) and expanding up to quintic terms to obtain

$$\ddot{x}_t + 2\zeta\dot{x}_t + \omega_2^2 x_t + \tau x_t^2 + \beta x_t^3 + \eta x_t^4 + \gamma x_t^5 + \kappa^2 y = \mathcal{F}\cos(\Omega t), \tag{5.5a}$$

$$\dot{y} + \alpha y = \dot{x}_t, \tag{5.5b}$$

where, $\omega_2 = \sqrt{(1-r) + 3\delta x_s^2 + 5\gamma x_s^4}$ represents the linearized oscillation frequency within a single outer potential well, $\tau = 3\delta x_s + 10\gamma x_s^3$ is the coefficient of quadratic nonlinearity, $\beta = \delta + 10\gamma x_s^2$ is the coefficient of cubic nonlinearity, and $\eta = 5\gamma x_s$ is the coefficient of quartic nonlinearity. It is worth noting that the expanded equations now include the quadratic and quartic terms to capture the asymmetric nature of the response within either one of the outer potential wells.

Again, we use the method of multiple scales to obtain uniform approximate analytical solutions of Equations (5.5a) and (5.5b). Towards that end, the time dependence is expanded into multiple time scales in the form:

$$T_n = \epsilon^n t, \tag{5.6}$$

where ϵ is a book keeping parameter. With this definition of the time scales, the time derivative can

be expressed as:

$$\frac{d}{dt} = \sum_{n=0}^{m} \epsilon^n D_n, \tag{5.7}$$

where $D_n = \frac{\partial}{\partial T_n}$. Furthermore, x_t and y can be expanded in the following form:

$$x_t(t,\epsilon) = \sum_{n=0}^{m} \epsilon^n x_n(T_0, T_1, \ldots, T_n), \qquad y(t,\epsilon) = \sum_{n=0}^{m} \epsilon^n y_n(T_0, T_1, \ldots, T_n) \tag{5.8}$$

The constant parameters in the equations are scaled such that the effect of viscous damping appears at the same order of the perturbation problem as the nonlinearities, electromechanical coupling, and the forcing. In other words, we let

$$\zeta = \epsilon^2\zeta, \quad \tau = \epsilon\tau, \quad \beta = \epsilon^2\beta, \quad \eta = \epsilon^2\eta, \quad \gamma = \epsilon^2\gamma, \quad \kappa^2 = \epsilon^2\kappa^2, \quad \mathcal{F} = \epsilon^2\mathcal{F}. \tag{5.9}$$

To express the nearness of the excitation frequency, Ω, to the resonance frequency within a single outer potential well, we let

$$\Omega = \omega_2 + \epsilon^2\sigma, \tag{5.10}$$

where σ is a small detuning parameter. Substituting Equations (5.7)-(5.10) back into Equations (5.5a) and (5.5b), truncating at order ϵ^2 and collecting terms of equal powers of ϵ yields

$O(\epsilon^0)$:

$$D_0^2 x_0 + \omega_2^2 x_0 = 0, \tag{5.11a}$$

$$D_0 y_0 + \alpha y_0 = D_0 x_0, \tag{5.11b}$$

$O(\epsilon^1)$:

$$D_0^2 x_1 + \omega_2^2 x_1 = -2D_0 D_1 x_0 - \tau x_0^2, \tag{5.12a}$$

$$D_0 y_1 + \alpha y_1 = D_0 x_1 + D_1 x_0 - D_1 y_0, \tag{5.12b}$$

$O(\epsilon^2)$:

$$D_0^2 x_2 + \omega_2^2 x_2 = -2D_0 D_1 x_1 - D_1^2 x_0 - 2D_0 D_2 x_0 - 2\zeta D_0 x_0 - 2\tau x_0 x_1 - \beta x_0^3 - \eta x_0^4 - \gamma x_0^5 - \kappa^2 y_0 + \mathcal{F}\cos(\Omega t), \tag{5.13a}$$

$$D_0 y_2 + \alpha y_2 = D_0 x_2 + D_1 x_1 + D_2 x_0 - D_1 y_1 - D_2 y_0. \tag{5.13b}$$

The solution of the zeroth-order perturbation problem, Equations (5.11a) and (5.11b), can be written as:

$$x_0 = A(T_1, T_2)e^{i\omega_2 T_0} + cc, \tag{5.14a}$$

$$y_0 = Z_0 A(T_1, T_2)e^{i\omega_2 T_0} + cc, \tag{5.14b}$$

where cc is the complex conjugate of the preceding term, $A(T_1, T_2)$ is a complex-valued function to be determined at a later stage of the analysis, and $Z_0 = \frac{\omega_2^2 + i\omega_2\alpha}{\alpha^2 + \omega_2^2}$. Substituting Equations (5.14a) and (5.14b) into Equations (5.12a) and (5.12b), and eliminating the secular terms, terms that have the coefficient $e^{\pm i\omega_2 T_0}$, yields,

$$D_1 A(T_1, T_2) = 0 \Longrightarrow A = A(T_2). \tag{5.15}$$

With this result, the solution of the first-order Equations (5.12a) and (5.12b) can be written as:

$$x_1 = \frac{\tau}{\omega_2^2}\left(\frac{1}{3}A^2 e^{i2\omega_2 T_0} - 2A\bar{A}\right) + cc, \tag{5.16a}$$

$$y_1 = Z_1 \frac{\tau}{3\omega_2^2} A^2 e^{i2\omega_2 T_0} + cc, \tag{5.16b}$$

where $\bar{A}$ is the complex conjugate of A and $Z_1 = \frac{4\omega_2^2 + 2i\omega_2\alpha}{\alpha^2 + 4\omega_2^2}$. Now, to obtain the unknown function A, we substitute Equations (5.14a), (5.14b), and (5.16a) into Equation (5.13a), then eliminate the secular terms to obtain the following nonlinear first order differential equation for the unknown A:

$$-2i\omega_2 D_2 A - 2i\omega_2\zeta A + \left[\frac{10}{3}\left(\frac{\tau}{\omega_2}\right)^2 - 3\beta\right]A^2\bar{A} - 10\gamma A^3\bar{A}^2 - \kappa^2 Z_0 A + \frac{\mathcal{F}}{2}e^{i\sigma T_2} = 0. \tag{5.17}$$

To find the solution of Equation (5.17), we express the complex-valued function, A, in the polar

form

$$A(T_2) = \frac{1}{2}a(T_2)e^{i\psi(T_2)}, \qquad \bar{A}(T_2) = \frac{1}{2}a(T_2)e^{-i\psi(T_2)}. \tag{5.18}$$

Substituting Equation (5.18) into Equation (5.17), and separating the real and imaginary parts of the outcome, we obtain

$$D_2 a = -\Big(\zeta + \zeta_e\Big)a + \tfrac{\mathcal{F}}{2\omega_2}\sin\phi, \tag{5.19a}$$

$$aD_2\beta = (\sigma - \gamma_s)a - N_{eff}a^3 - \tfrac{5}{16}\tfrac{\gamma a_0^5}{\omega_2} + \tfrac{\mathcal{F}}{2\omega_2}\cos\phi, \tag{5.19b}$$

where $\phi = \sigma T_2 - \psi$, $\zeta_e = \frac{\kappa^2\alpha}{2(\alpha^2+\omega_2^2)}$ represents the electric damping, $N_{eff} = \frac{1}{\omega_2}\left[\frac{3}{8}\beta - \frac{5}{12}\frac{\tau^2}{\omega_2^2}\right]$ represents the effective cubic nonlinearity coefficient, and $\gamma_s = \frac{\kappa^2\omega_2}{2(\alpha^2+\omega_2^2)}$ represents a linear shift in the local natural frequency due to the electric coupling.

For energy harvesting, we are interested in investigating the steady-state response. To that end, we set the time derivatives in Equations (5.19a) and (5.19b) to zero, square and add the resulting equations to obtain

$$\zeta_{eff}^2 a_0^2 + \left[(\sigma - \gamma_s)a_0 - N_{eff}a_0^3 - \frac{5}{16}\frac{\gamma}{\omega_2}a_0^5\right]^2 = \frac{\mathcal{F}^2}{4\omega_2^2}. \tag{5.20}$$

where $\zeta_{eff} = \zeta + \zeta_e$ represents the effective damping and a_0 represents the steady-state amplitude. Similar to bi-stable VEHs, Equation (5.20) represents a nonlinear frequency-response equation, which can be solved analytically for the steady-state amplitude of a tri-stable VEH under harmonic inputs for any given forcing amplitude, $\mathcal{F}$. Depending on the forcing and the excitation frequency, there exists one or three positive real valued solutions. The stability of these equilibria can be determined by assessing the eigenvalues of the associated Jacobian matrix. The steady-state solutions for the

deflection as well as the electric quantity can then be expressed in the following form:

$$x_t(t) = \tfrac{1}{\omega_2^2}\left(-\tfrac{\tau a_0^2}{2} - \tfrac{3\eta a_0^4}{8}\right) + a_0\cos(\Omega t - \phi_0) + \tfrac{1}{6\omega_2^2}(\tau a_0^2 + \eta a_0^4)\cos(2\Omega t - 2\phi_0)$$
$$+\tfrac{a_0^3}{32\omega_2^2}\left(\tfrac{2\tau^2}{3\omega_2^2} + \beta - \tfrac{5}{4}\gamma a_0^2\right)\cos(3\Omega t - 3\phi_0) + \tfrac{\eta a_0^4}{120\omega_2^2}\cos(4\Omega t - 4\phi_0)$$
$$+\tfrac{\gamma a_0^5}{384\omega_2^2}\cos(5\Omega t - 5\phi_0), \tag{5.21a}$$

$$y(t) = \tfrac{\omega_2}{\sqrt{\alpha^2+\omega_2^2}}a_0\cos(\Omega t - \phi_0 + \psi_1) + \tfrac{\tau + a_0^3\eta}{6\omega_2\sqrt{\alpha^2+4\omega_2^2}}a_0\cos(2\Omega t - 2\phi_0 + \psi_2)$$
$$+\tfrac{3a_0^3}{64\omega_2\sqrt{\alpha^2+9\omega_2^2}}\left(\tfrac{2\tau^2}{3\omega_2^2} + \beta + \tfrac{5\gamma a_0}{4}\right)\cos(3\Omega t - 3\phi_0 + \psi_3)$$
$$+\tfrac{a_0^4\eta}{60\omega_2\sqrt{\alpha^2+16\omega_2^2}}\cos(4\Omega t - 4\phi_0 + \psi_4) + \tfrac{5a_0^5\gamma}{768\omega_2\sqrt{\alpha^2+25\omega_2^2}}\cos(5\Omega t - 5\phi_0 + \psi_5). \tag{5.21b}$$

where

$$\beta_0 = \tan^{-1}\left(\frac{\zeta_{eff}}{\Gamma a_0^2 - (\sigma - \gamma_s)}\right), \qquad \psi_n = \tan^{-1}\left(\frac{\alpha}{n\omega_2}\right), \qquad \Gamma = N_{eff} + \frac{5\gamma a_0^2}{16\omega_2}. \tag{5.22}$$

5.3.2 Solutions for symmetric oscillations

In this section, we derive expressions for the dynamics that govern the global inter-well responses as well as the oscillations around the trivial equilibrium ($x_s = 0$). Towards that end, we express the deviation of the excitation frequency, Ω, from the resonance frequency in the middle potential well, ω_1, using a detuning parameter, σ, for the primary resonance case using [74]

$$\Omega^2 = \omega_1^2 + \epsilon\sigma \tag{5.23}$$

where ϵ is a small book-keeping parameter and $\omega_1 = \sqrt{1-r}$ is obtained by substituting $x_s = 0$ into Equation (5.4). Next, we scale the constants in Equation (5.1a) such that the effect of the viscous damping appears in the same order of the perturbation problem as the nonlinearities, electromechanical coupling, and the forcing. To that end, we let,

$$\zeta = \epsilon\zeta, \quad \delta = \epsilon\delta, \quad \gamma = \epsilon\gamma, \quad \kappa^2 = \epsilon\kappa^2, \quad \mathcal{F} = \epsilon\mathcal{F} \tag{5.24}$$

Upon substituting Equations (5.23) and (5.24) into Equation (5.1a), we obtain

$$\ddot{x} + \Omega^2 x - \epsilon\sigma + \epsilon\left[2\zeta\dot{x} + \delta x^3 + \gamma x^5 + \kappa^2 y\right] = \epsilon\mathcal{F}\cos(\Omega t) \tag{5.25}$$

As shown in the previous section, we substitute the expansions for x and y from Equation (5.8) along with the expansions for the time scales and derivatives into Equations (5.25) and (5.1b), truncate the resulting equations at order ϵ, and collect terms of equal powers of ϵ to obtain,

$O(\epsilon^0)$:

$$D_0^2 x_0 + \Omega^2 x_0 = 0, \tag{5.26a}$$

$$D_0 y_0 + \alpha y_0 = D_0 x_0, \tag{5.26b}$$

$O(\epsilon^1)$:

$$D_0^2 x_1 + \Omega^2 x_1 = -2D_0 D_1 x_0 - 2\zeta D_0 x_0 - \delta x_0^3 - \gamma x_0^5 + \sigma x_0 - \kappa^2 y_0 + \mathcal{F}\cos(\Omega T_0), \tag{5.27a}$$

$$D_0 y_1 + \alpha y_1 = D_0 x_1 + D_1 x_0 - D_1 y_0. \tag{5.27b}$$

The solutions of the zeroth-order perturbation problem, Equations (5.26a) and (5.26b), can be written as:

$$\begin{aligned} x_0 &= A(T_1)e^{i\Omega T_0} + cc, \\ y_0 &= Z_0 A(T_1)e^{i\Omega T_0} + cc, \quad \text{where} \quad Z_0 = \frac{\Omega^2 + i\alpha\Omega}{\alpha^2 + \Omega^2} \end{aligned} \tag{5.28}$$

Similar to the method used in Section (5.3.1), we substitute the solutions of the zeroth-order perturbation problem given by Equation (5.28) into Equation (5.27a), eliminate the secular terms, and express the complex-valued function, A, in the polar form. This results in the modulation equations for the response amplitude and phase. The modulation equations are then used to obtain the following nonlinear frequency-response equation:

$$\zeta_{eff}^2 a_0^2 + \left[\frac{a_0}{2\Omega}(\sigma - \gamma_s) - \frac{3\delta}{8\Omega}a_0^3 - \frac{5\gamma}{16\Omega}a_0^5\right]^2 = \frac{\mathcal{F}^2}{4\Omega^2}. \tag{5.29}$$

where, $\zeta_{eff} = (\zeta + \zeta_e)$, $\zeta_e = \kappa^2\alpha/2(\alpha^2 + \Omega^2)$, and $\gamma_s = \kappa^2\Omega^2/(\alpha^2 + \Omega^2)$ represent, respectively, the effective damping, electric damping, and the linear shift in the natural frequency due to the electric

coupling. Upon eliminating secular terms from Equation (5.27a), we have

$$D_0^2 x_1 + \Omega^2 x_1 = -\left(\frac{\delta a_0^3}{8} + \frac{5\gamma a_0^5}{32}\right) e^{3i(\Omega T_0+\phi)} - \frac{\gamma a_0^5}{32} e^{5i(\Omega T_0+\phi)} + cc, \tag{5.30}$$

for which the particular solutions can be written as

$$x_1 = \left(\frac{\delta a_0^3}{64\Omega^2} + \frac{5\gamma a_0^5}{256\Omega^2}\right) e^{3i(\Omega T_0+\phi)} + \frac{\gamma a_0^5}{768\Omega^2} e^{5i(\Omega T_0+\phi)} + cc, \tag{5.31}$$

and

$$y_1 = Z_1\left(\frac{\delta a_0^3}{64\Omega^2} + \frac{5\gamma a_0^5}{256\Omega^2}\right) e^{3i(\Omega T_0+\phi)} + Z_2\frac{\gamma a_0^5}{768\Omega^2} e^{5i(\Omega T_0+\phi)} + cc, \tag{5.32}$$

where $Z_1 = \frac{9\Omega^2+3i\alpha\Omega}{\alpha^2+9\Omega^2}$ and $Z_2 = \frac{25\Omega^2+5i\alpha\Omega}{\alpha^2+25\Omega^2}$. Substituting the zeroth and first-order solutions back into the assumed expansion, the analytical solutions describing the deflections and electric outputs associated with the large-amplitude inter-well oscillations as well as the intra-well oscillations around the trivial equilibrium of a tri-stable harvester can be written as,

$$x(t) = a_0\cos(\Omega t + \phi_0) + \left(\tfrac{\delta a_0^3}{32\Omega^2} + \tfrac{5\gamma a_0^5}{128\Omega^2}\right)\cos(3\Omega t + 3\phi_0) + \tfrac{\gamma a_0^5}{384\Omega^2}\cos(5\Omega t + 5\phi_0), \tag{5.33a}$$

$$\begin{aligned} y(t) = {} & \tfrac{a_0\Omega}{\sqrt{\alpha^2+\Omega^2}}\cos(\Omega t + \phi_0 + \psi_1) + \tfrac{3a_0^3}{32\Omega\sqrt{\alpha^2+9\Omega^2}}\left(\delta + \tfrac{5\gamma a_0^2}{4}\right)\cos(3\Omega t + 3\phi_0 + \psi_3) \\ & + \tfrac{5\gamma a_0^5}{384\Omega\sqrt{\alpha^2+25\Omega^2}}\cos(5\Omega t + 5\phi_0 + \psi_5). \end{aligned} \tag{5.33b}$$

where

$$\phi_0 = \tan^{-1}\left(\frac{16\zeta_{eff}\Omega}{8(\sigma-\gamma_s) - 6\delta a_0^2 - 5\gamma a_0^4}\right), \qquad \psi_n = \tan^{-1}(\alpha/n\Omega). \tag{5.34}$$

5.3.3 Bifurcation points

As shown in Chapter 3, we utilize the analytical expressions for the global as well as intra-well periodic responses to analyze their stability and obtain approximate expressions for the key bifurcations discussed in Section 5.2. Towards that end, we first analyze the cyclic-fold bifurcations and then discuss the period-doubling bifurcations of a tri-stable VEH.

5.3.3.1 Cyclic-Fold Bifurcations

There are two critical cyclic-fold bifurcations, cfL and $cf1$, that are of particular importance in approximating the range of frequencies over which large-amplitude responses can be uniquely realized. It is worth reiterating that the bifurcation cfL indicates how far the large-amplitude (global) inter-well oscillations extend in the frequency domain while $cf1$ indicates the frequency at which the non-resonant branch of intra-well oscillations associated with the central potential well ceases to exist. In order to obtain the expressions that approximate these two bifurcations, we seek the value of frequencies at which the slope of the frequency-response curves tend to infinity. Towards this end, we set $\frac{d\Omega}{da_0}\big|_{a_b,\Omega_b} = 0$ in Equation (5.29) to obtain,

$$125\gamma^2 a_b^8 + 240\delta\gamma a_b^6 + \left[108\delta^2 - 240\gamma(\sigma - \gamma_s)\right] a_b^4 - 192\delta(\sigma - \gamma_s)a_b^2 + (\sigma - \gamma_s)^2 + 256\Omega_b^2\zeta_{eff}^2 = 0, \quad (5.35)$$

where a_b and Ω_b represent the amplitude and frequency of the response at the bifurcation point. Depending on the value of Ω_b, Equation (5.35) has four positive real-valued solutions, two of which represent the amplitudes at which the bifurcations, cfL and $cf1$, occur. The third solution represents the amplitude at which the resonant intra-well branch of solution, B_{r1}, loses stability through the cyclic-fold bifurcation, $cf2$. The loci of these cyclic-fold bifurcations in the $\mathcal{F}$ - Ω space are then obtained by substituting these solutions and the corresponding values of Ω_b into Equation (5.29) and solving the resulting equations for the critical forcing, $\mathcal{F}$.

Figure 5.3 depicts the loci of the cyclic-fold bifurcations of the solution branches within the central potential well and that of the inter-well solution branch in the force-frequency parameter space. It can be seen from the figure that the frequency at which the cfL occurs increases as the magnitude of the forcing increases, thereby extending the desirable responses over a larger frequency range. On the other hand, for the intra-well solutions, the figure illustrates that, below a critical forcing amplitude, $\mathcal{F}_{cr}$, the cyclic-fold bifurcations $cf1$ and $cf2$ collide and disappear. In this scenario, the harvester performs linear oscillations that are confined to the middle potential well. As the forcing is increased, there is a separation between the frequencies at which the bifurcations $cf1$ and $cf2$ occur owing to the softening nonlinearity. As shown in the numerical analysis, the resonant and non-resonant branches of intra-well oscillations associated with the symmetric outer potential wells also undergo cyclic-fold bifurcations, cfA and cfB. In order to obtain the loci of these bifurcations in the force-frequency domain, we follow the procedure outlined above and obtain

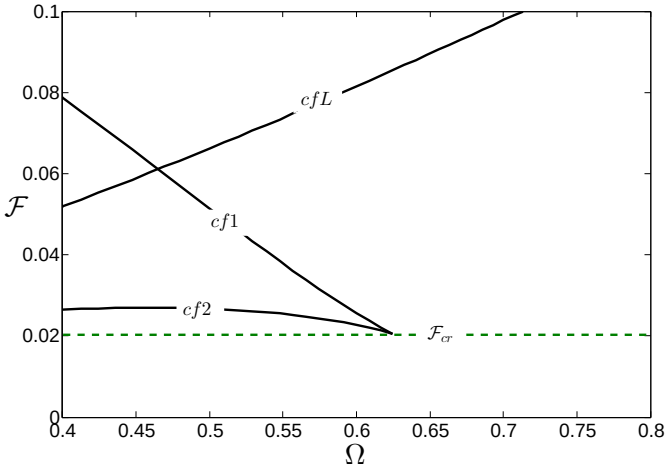

Figure 5.3: Loci of the cyclic-fold bifurcations of the intra- and inter-well oscillations in the force-frequency parameter space. Results are obtained for $\zeta = 0.05$, $r = 0.5$, $\delta = -1.5$, $\gamma = 0.95$, $\kappa^2 = 0.01$, and $\alpha = 0.1$.

the value of frequencies at which the slope of the frequency-response curves associated with the intra-well responses in the outer potential well using Equation (5.20). Figure 5.4 illustrates how the loci of the bifurcations cfA and cfB are similar to the cyclic-fold bifurcations in the middle potential well, $cf1$ and $cf2$, but occur at higher frequency values compared to them. Again, there is a critical value of forcing below which the oscillations are linear and remain confined to the outer potential well and the loci illustrate the softening nature of the nonlinearity.

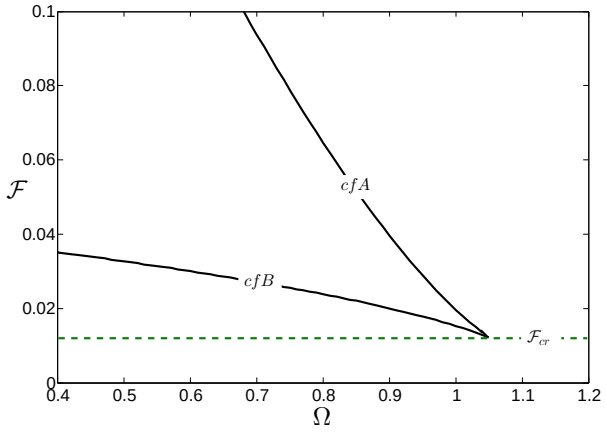

Figure 5.4: Loci of the cyclic-fold bifurcations of the intra-well oscillations in the force-frequency parameter space. Results are obtained for $\zeta = 0.05$, $r = 0.5$, $\delta = -1.5$, $\gamma = 0.95$, $\kappa^2 = 0.01$, and $\alpha = 0.1$.

5.3.3.2 Period-Doubling Bifurcations

As described earlier, there are three period doubling bifurcations namely, $pd2$, pdA, and pdB associated with the intra-well oscillations in the middle as well as the outer potential wells. From the numerical analysis described earlier, it was shown that the bifurcations $pd2$ and pdA lead to a window of aperiodic motions that coexist with the desired large amplitude motions. As such, it is essential to determine the frequencies at which these bifurcations occur in order to identify regions in the frequency domain where the harvester can uniquely produce large electric outputs. To obtain analytical approximations of these bifurcations, we analyze the stability of steady-state periodic solutions for the amplitude and electric quantity associated with the intra-well oscillations. Towards that end, we introduce small time-dependent perturbations $\nu_1(t)$ and $\nu_2(t)$ to the solutions given by Equations (5.21) and (5.33) in the form $\tilde{x} = x_t(t) + \nu_1(t)$ and $\tilde{y} = y(t) + \nu_2(t)$ as shown in Section 3.3.2.2 of Chapter 3. The resulting equations are linearized for small perturbations to obtain variational equations of the form Equation (3.22). The method outlined in Section 3.3.2.2 is used to solve the variational equations and obtain expressions that predict the values of frequency and amplitude at the period doubling bifurcations. The loci of the bifurcations, pdB and pdA, of the resonant and non-resonant branches of solution within the outer potential wells, are shown in Fig. 5.5(a). The figure illustrates that, as the forcing level increases, the period-doubling bifurcation, pdA, occurs at lower excitation frequencies, whereas the bifurcation pdB occurs at higher excitation frequencies. The locus of the period-doubling bifurcation of the resonant intra-well oscillations associated with the central potential well, $pd2$, in the $\mathcal{F} - \Omega$ domain, is shown in Fig. 5.5(b). The figure clearly illustrates how the frequency at which the $pd2$ bifurcation occurs, increases with the forcing level.

5.3.4 Asymptotic Responses

Equations (5.20) and (5.29) are used to analytically construct the frequency-response curves of the tri-stable VEH for three different forcing levels as depicted in Fig. 5.6. The figure captures the amplitude of oscillation and the frequencies at which the cyclic-fold bifurcations cfL, $cf1$, $cf2$, cfA and cfB and the period-doubling bifurcations pdA, $pd2$ and pdB occur in addition to outlining their dependence on the excitation amplitude.

A comparison between the analytical results and the stroboscopic bifurcation maps obtained

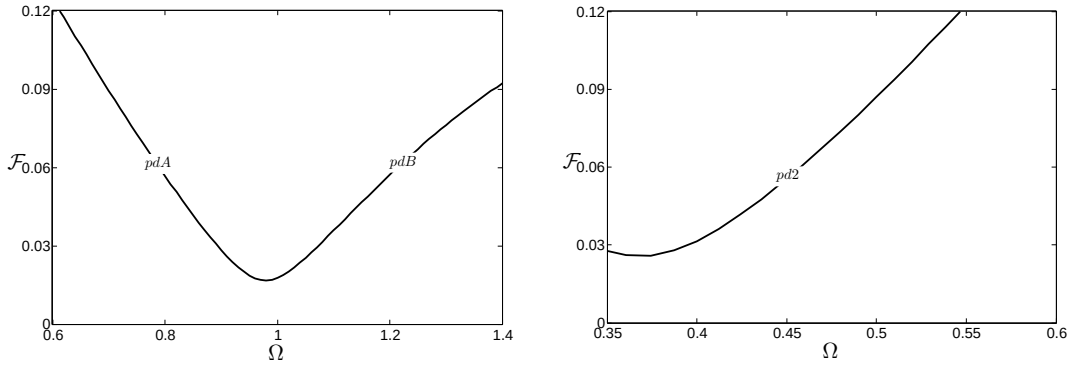

Figure 5.5: (a) Loci of the bifurcations pdA and pdB in the force-frequency parameter space (b) Loci of the bifurcation $pd2$ in the force-frequency parameter space. Results are obtained for $\zeta = 0.05$, $r = 0.5$, $\delta = -1.5$, $\gamma = 0.95$, $\kappa^2 = 0.01$, and $\alpha = 0.1$.

numerically show good agreement and the ability of the analytical responses to predict the bifurcation points with relative accuracy as depicted in Fig. 5.7. A close inspection of the results reveal that the analytical solutions over predict the frequencies at which the period-doubling bifurcations, pdB and pdA, occur and under predict the frequencies at which the bifurcation $pd2$ occurs. This can be explained by knowing that the method utilized to predict these bifurcation points involves assessing stability of the periodic solutions with time-varying perturbations that are considered to be small, thereby invoking linear assumptions while obtaining the regions of instability in the frequency domain.

5.3.5 Influence of the Electric Parameters on the Bifurcation Points

In this section, we study the influence of the electric parameters namely, the time constant ratio, α, and the electromechanical coupling, κ^2 on the bifurcations of the tri-stable VEH. The time constant ratio can be considered as a measure of the influence of the electric load while κ^2 represents the strength of coupling between the mechanical and electrical subsystems. Figure 5.8 depicts the effect of varying the time constant ratio on the loci of the bifurcations discussed in Section 5.3.3, in the forcing-frequency domain. A close inspection of the Figs. 5.8(a), 5.8(c), 5.8(b), and 5.8(d) reveals that the locations of the cyclic-fold bifurcation points cfL, $cf1$, $cf2$, cfA, and cBA and the period-doubling bifurcations pdA, pdB, and $pd2$ are nearly the same for all values of α despite varying it by an order of magnitude from the nominal value of 0.1. As such, the time constant

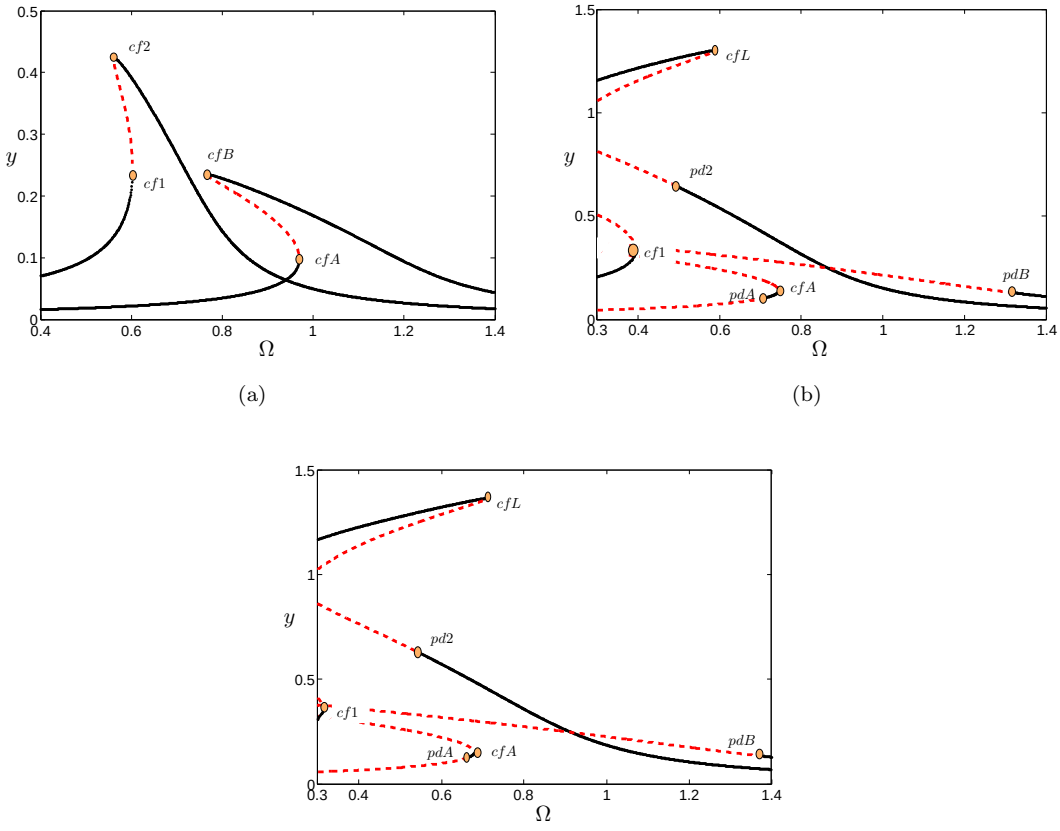

Figure 5.6: Analytical frequency-response curves for a tri-stable harvester at three different excitation levels. Dashed lines represent unstable solutions. Results are obtained for $\zeta = 0.05$, $r = 0.5$, $\delta = -1.5$, $\gamma = 0.95$, $\kappa^2 = 0.01$, $\alpha = 0.1$ and normalized base excitation amplitudes (a) $\mathcal{F} = 0.025$, (b) $\mathcal{F} = 0.08$, and (c) $\mathcal{F} = 0.1$

ratio has little to no influence on the bandwidth of tri-stable VEHs, which was observed in the bi-stable case. However, this could influence the amplitude of the electric response. Consequently, changing the electric load does not significantly alter the loci of the bifurcation points. On the other hand, varying the electromechanical coupling, κ^2, has a noticeable impact on the loci of the intra- and inter-well bifurcation points as seen in Fig. 5.9. Figure 5.9(a) shows that the locus of the cyclic-fold bifurcation of the large-orbit inter-well oscillations, cfL, shifts up in the force-frequency parameter space with small increments in κ^2, meaning that these desirable oscillations exist over lower frequency range for the same forcing. Figure 5.9(a) also shows that, for a given forcing, the cyclic-fold bifurcations of the resonant and non-resonant branches of oscillation associated with the middle potential well, $cf1$ and $cf2$, respectively, occur at higher excitation frequencies as κ^2 is

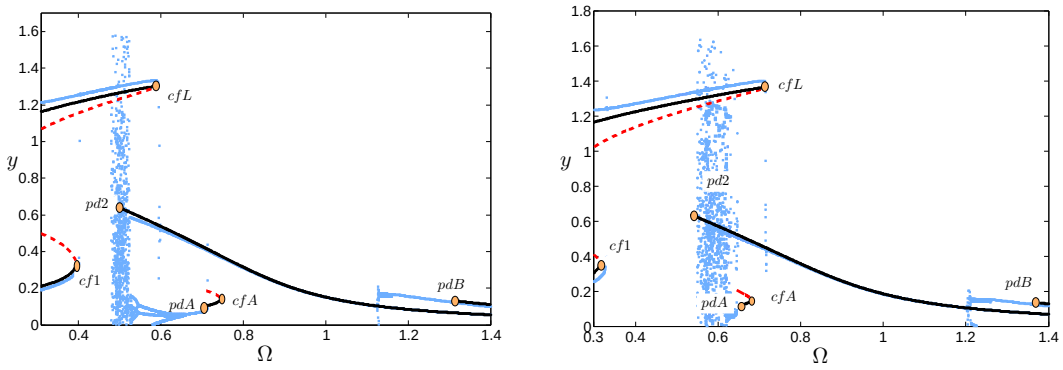

Figure 5.7: Comparison of numerical and analytical frequency responses. Light blue curves represent numerical solutions. Results are obtained for normalized base excitation amplitudes (a) $\mathcal{F} = 0.08$ and (b) $\mathcal{F} = 0.1$.

increased. This implies that the intra-well motions extend over a wider range of frequencies for higher electromechanical coupling due to the increase in the electric damping of the system.

Figure 5.9(b) depicts the effect of the electromechanical coupling on the period-doubling bifurcation of the resonant branch of oscillations in the middle potential well, $pd2$. Again, due to an increase in the electric damping with small increments in κ^2, the $pd2$ bifurcation occurs at higher frequencies for a given forcing, implying that aperiodic responses caused by the $pd2$ bifurcation exist over a larger frequency range. Figure 5.9(c) illustrates that the loci of the cyclic-fold bifurcations, cfA and cfB, occur at higher frequencies as κ^2 is increased. A similar trend is observed in Fig. 5.9(d) with the locus of the period-doubling bifurcation, pdB, of the resonant branch of oscillations. It can be seen that, while the locus of the pdA bifurcation does not vary significantly, the frequency at which pdb occurs increases with an increase in κ^2. As such, increasing the electromechanical coupling shrinks the frequency range over which the large-orbit solution exists and increases the frequency range over which the small-amplitude solutions exist for the tri-stable VEH. This trend is very similar to that observed in the case of bi-stable VEHs.

5.4 Effective Bandwidth

By utilizing the analytical framework developed in this chapter, and following the analysis outlined in Chapter 3, it is possible to identify and characterize boundaries for intra- versus inter-

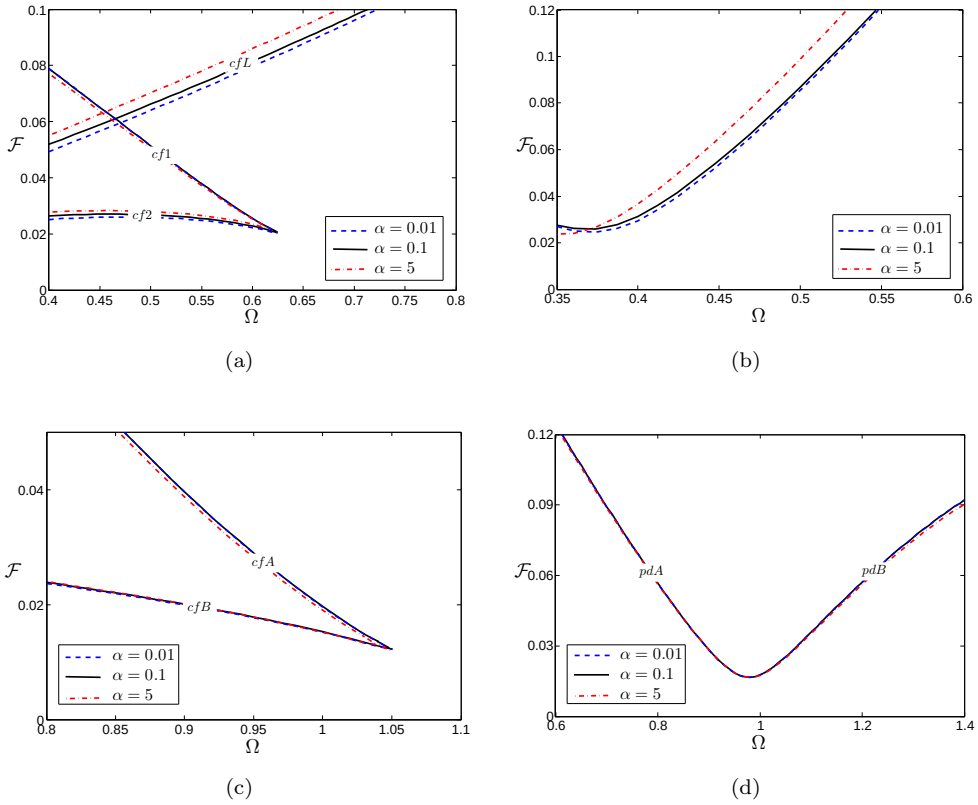

Figure 5.8: Effect of varying the time constant ratio, α, on the loci of the (a) cyclic-fold bifurcation points, cfL, $cf1$ and $cf2$, (b) period-doubling bifurcation point of the intra-well oscillations in the middle potential well, $pd2$, (c) intra-well cyclic-fold bifurcation points, cfA and cfB, and (d) period-doubling bifurcation points of the intra-well oscillations in the outer potential wells, pdA and pdB. Results are obtained for $\zeta = 0.05$, $r = 0.5$, $\delta = -1.5$, $\gamma = 0.95$, and $\kappa^2 = 0.01$.

well responses in the force-frequency parameter space for a tri-stable VEH. Figure 5.10 depicts a bifurcation map that delineates several regions, four of which are of particular importance and are used to describe the response behavior of tri-stable VEHs for a given force-frequency combination. The first lies between three curves cfL, cfA and pdB and is denoted by B_{r1}. In this region, the harvester exhibits small-amplitude intra-well responses that are confined to the middle potential well. The second region is located between the cfL and $pd2$ curves and contains the large-amplitude inter-well responses, B_L. However, these responses are accompanied by the B_{r1} and by chaotic (CH) or $n-$period periodic responses ($n > 1$) resulting from the period-doubling bifurcations, pdA. The third region lies in the low frequency range, between the $pd2$ and $cf1$ curves and represents the force-frequency combinations for which the harvester performs the large-orbit inter-well motions,

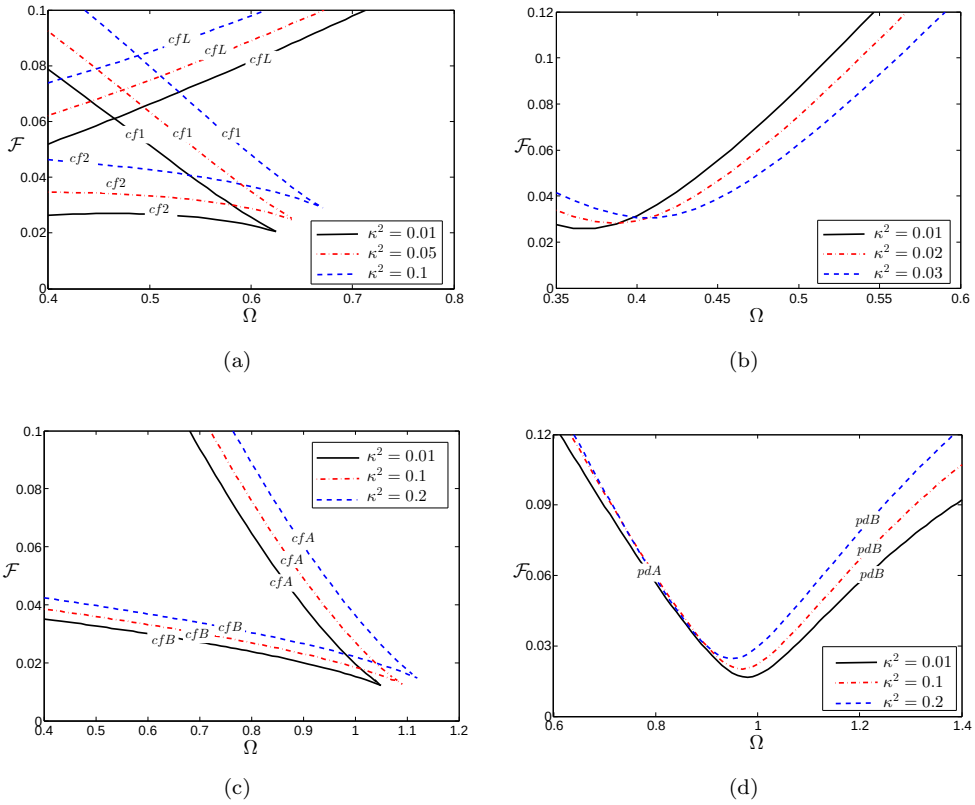

Figure 5.9: Effect of varying the electromechanical coupling coefficient, κ^2, on the loci of the (a) cyclic-fold bifurcation points cfL, $cf1$ and $cf2$, (b) period-doubling bifurcation point of the intra-well oscillations in the middle potential well, $pd2$, (c) intra-well cyclic-fold bifurcation points, cfA and cfB, and (d) period-doubling bifurcation points of the intra-well oscillations in the outer potential wells, pdA and pdB. Results are obtained for $\zeta = 0.05$, $r = 0.5$, $\delta = -1.5$, $\gamma = 0.95$, and $\alpha = 0.1$.

B_L. These motions can either be uniquely realized or can be accompanied by the complex CH-type motions that result from the period-doubling bifurcations, $pd2$. Finally, the fourth region lies to the left of the $cf1$ and cfL curves and depicts the range of frequencies wherein the inter-well responses, B_L, are always accompanied by the less desirable non-resonant branch of intra-well responses, B_{n1}. As such, depending on the initial conditions, the harvester can operate on either the large or small orbit branches of solution.

The map represented in Fig. 5.10 also permits identifying four critical forcing levels that define the nature of the dynamic responses of the tri-stable VEH. Any forcing magnitude below F_{cr1} only leads to small-amplitude intra-well motions. Below this forcing level, no bifurcations occur and the voltage-frequency response is a nearly bell-shaped linear curve and represents oscillations that

are confined to the middle potential well or either one of the outer potential wells. Above this critical forcing, if the dynamic trajectories are confined to the outer potential wells, the voltage response curve bends to the left and the bifurcations cfA and cfB appear.

Above the critical forcing, F_{cr2}, the period-doubling bifurcations, pdA and pdB, exist and more complex aperiodic responses begin to appear. The critical forcing, F_{cr3}, indicates the threshold value of forcing required to initiate the bifurcations $cf1$ and $cf2$ which represent the cyclic-fold bifurcations within the middle potential well. It is worth noting that, the critical forcing values required to initiate the bending of the frequency response curves are different for the middle potential well and either of the two outer wells. This is due to the difference in depths between the central and outer potential wells. Finally, above the critical forcing F_{cr4}, the large-amplitude steady-state periodic inter-well motions cfL begin to appear for the range of frequencies considered in the analysis.

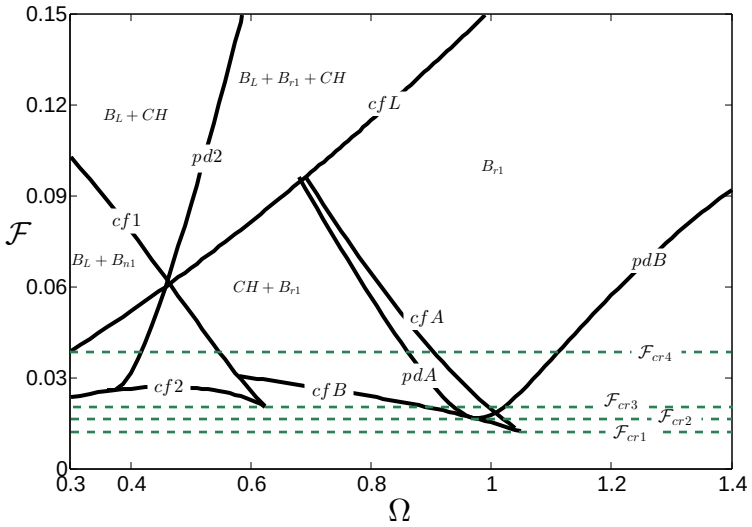

Figure 5.10: Bifurcation map defining regions of intra- and inter-well responses. The map is obtained for $\zeta = 0.05$, $r = 0.5$, $\delta = -1.5$, $\gamma = 0.95$, $\kappa^2 = 0.01$, and $\alpha = 0.1$.

With this understanding, the map shown in Fig. 5.10 can be used to provide a rough estimate of the effective bandwidth of the tri-stable VEH. For a given set of design parameters, it is possible to use this map to identify the forcing level and frequency bandwidth for which large-amplitude inter-well motions can be achieved either uniquely or with other less favorable motions.

5.5 Experimental Investigation

To demonstrate the ability of the model and the analytical solutions to accurately capture the qualitative behavior, we consider the piezoelectric tri-stable VEH depicted in Fig. 5.11. The harvester consists of a beam clamped at one end and free to oscillate at the other. A piezoelectric Micro Fiber Composite (MFC) patch is attached at the fixed end of the beam and two cylindrical tip magnets are attached at the free end. Two stationary magnets separated by a distance, d, are aligned parallel to the plane of the beam and mounted on brackets such that the tip magnets are at a height, h, from them. By varying d and h, the linear and nonlinear components of the restoring force can be varied. Accordingly, the shape of the potential energy function of the system can be altered such that it exhibits three minima (potential wells). Furthermore, the oscillation frequencies within these potential wells can be tuned by varying d and h.

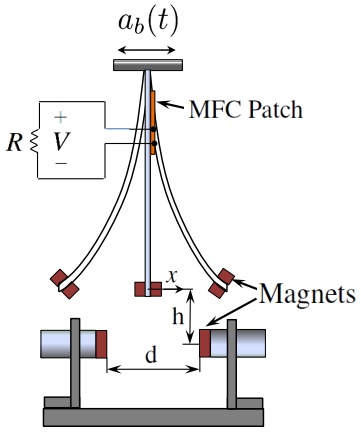

Figure 5.11: Schematic diagram of the tri-stable VEH used in the experiments.

The associated experimental setup, which is very similar to the one adopted by Zhou et. al [8, 53], is shown in Fig. 5.12. It consists of a cantilever beam mounted on an L-shaped structure such that its free end can oscillate in the horizontal direction. To create the tri-stable potential, two cylindrical Neodymium (NdFeB) magnets are attached to the tip of the beam and allowed to oscillate near two stationary NdFeB magnets mounted on brackets. The entire setup is placed on an electrodynamic shaker which generates a harmonic excitation signal whose magnitude is monitored using an accelerometer mounted on its base. For energy conversion, a piezoelectric MFC layer is laminated near the fixed end of the beam. The mass of the magnets at the tip of the beam is

measured to be 6 grams. The rest of the geometric and material properties of the structure are listed in Table 5.1. We choose the distance between the stationary magnets, $d = 11$ mm and the distance between the stationary and tip magnets, $h = 18$ mm. This results in the beam having three stable static equilibria which are located at $x_{s1} = 0$ and $x_{s2,3} = \pm 16.7$ mm. The local oscillation frequency around the trivial equilibrium, x_{s1}, is found to be $\omega_1 = 10.9$ Hz, while the oscillation frequency around the non-trivial equilibria, $x_{s2,3}$, is found to be $\omega_2 = 15.3$ Hz.

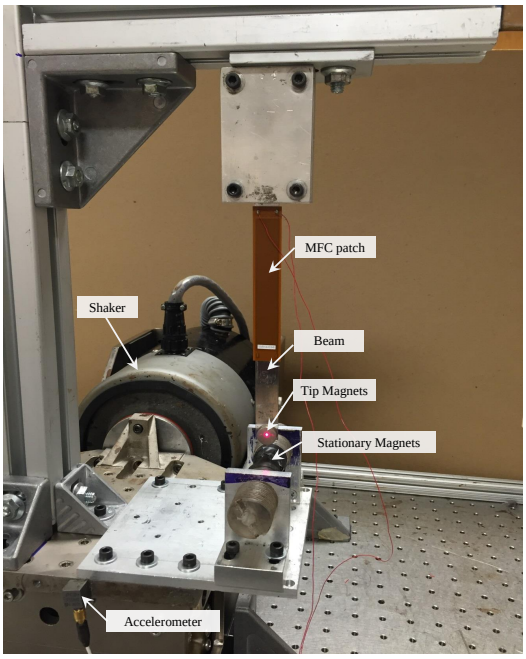

Figure 5.12: Experimental setup of a tri-stable VEH.

5.5.1 Static Analysis

We first perform a static experimental test to obtain the linear and nonlinear coefficients of the restoring force and thereby establish the potential energy function for the tri-stable VEH considered. Towards that end, we measure the force at the tip of the beam using a digital force gauge at different known displacements. Figure 5.13(a) depicts how the restoring force varies with the displacement of the beam tip. The figure also depicts a curve that is obtained by fitting a constrained polynomial to the data. As shown, the data is best approximated by the following

Table 5.1: Geometric and material properties of the tri-stable harvester.

Parameter (symbol)	Value
Structural member	
Young's Modulus (E_s)	200 GPa
Mass Density (ρ_s)	7500 Kg/m^3
Length (L_s)	15.60 x 10^{-2} m
Width (b_s)	1.42 x 10^{-2} m
Thickness (t_s)	5.08 x 10^{-4} m
Piezoelectric member	
Young's Modulus (E_p)	15.86 GPa
Mass Density (ρ_p)	5440 Kg/m^3
Length (L_p)	8.50 x 10^{-2} m
Width (b_s)	1.40 x 10^{-2} m
Thickness (t_s)	3.00 x 10^{-4} m
Piezoelectric constant (e_{31})	-3.33 C/m^2

polynomial approximation,

$$F_r = 26.2983\ x - 5.2277 \text{ x } 10^5\ x^3 + 1.6212 \text{ x } 10^9 x^5, \tag{5.36}$$

where F_r represents the restoring force, x is the tip deflection of the beam and the coefficients of x, x^3, and, x^5 represent, respectively, the linear, cubic, and quintic nonlinear stiffness coefficients. Using this expression, the potential energy of the system is obtained as shown in Fig. 5.13(b). The figure clearly illustrates that the potential energy is symmetric about zero and exhibits minima corresponding to the system's stable equilibria at x_{s1}, x_{s2}, and x_{s3}. It is clear that the outer potential wells associated with the non-trivial equilibria are deeper than the one in the center. This results in the local oscillation frequency, ω_2, being higher than ω_1.

5.5.2 Dynamic Analysis

In this section, we investigate the response behavior of the tri-stable VEH such that the excitation frequency encompasses both of the local oscillation frequencies, $\omega_1 = 10.9$ Hz and $\omega_2 = 15.3$ Hz. Since the system is nonlinear and can exhibit a hysteretic behavior, the excitation frequency is swept in the forward (low to high) and reverse (high to low) directions. Three different base

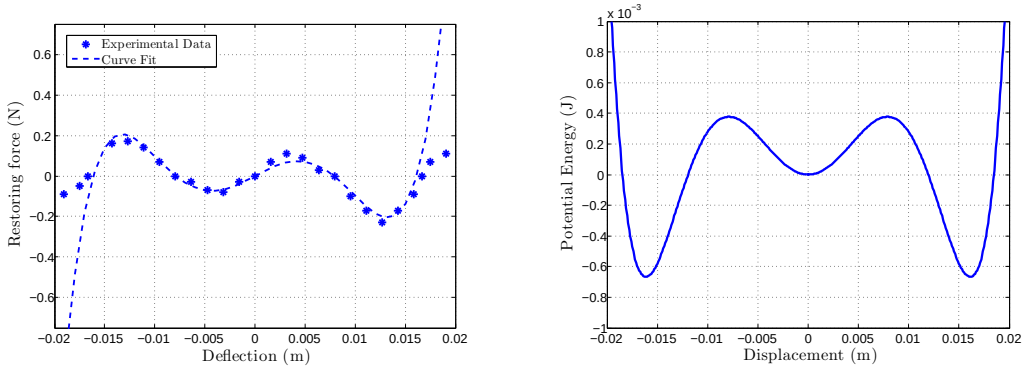

(a) (b)

Figure 5.13: (a) Variation of the restoring force with deflection. (b) Potential energy function of the experimental system.

accelerations are considered, namely 2, 6, and 8 m/s^2. Variation of the frequency was carried out at a slow enough rate such that the resulting response curves can be considered to represent steady-state behavior of the system. The harmonic excitation signal is generated at a workstation and fed to the harvester via the electrodynamic shaker. The amplitude is of oscillation at the tip of the beam is recorded using a laser vibrometer. The output voltage from the piezoelectric layer is measured across a 300 kΩ purely resistive load. These two measurements along with the acceleration signal are fed into the workstation via a data acquisition system.

Figure 5.14 depicts variation of the tip deflection and the output voltage with the frequency for both the forward and reverse sweeps at a base acceleration of 2.5 m/s^2 with the initial state of the system being the trivial equilibrium, $x_{s1} = 0$. It can be observed that oscillations remain, for the most part, confined within either the middle or the outer potential wells, implying that the base acceleration is not large enough to activate large amplitude inter-well oscillations. However, in the forward frequency sweep, in the vicinity of the local oscillation frequency, $\omega_1 = 10$ Hz, associated with the central potential well, the dynamic trajectories overcome the potential barrier and escape to the outer potential well associated with the static equilibrium $x_{s3} = -0.0167$ m as shown in Fig. 5.14(a). We can also note that, as the frequency is increased further, an intra-well resonant branch of oscillations appears at a frequency value of ≈ 13.5 Hz which is in the vicinity of the local oscillation frequency, $\omega_2 = 15.3$ Hz, of the outer potential well (see Fig. 5.14(a)). In the reverse frequency sweep, however, the oscillations remain centered around the initial displacement of zero

and exhibit a steady increase in amplitude until a frequency value of about 9 Hz, where a jump occurs to the outer potential well as seen in Fig.5.14(b). The figures clearly highlight the softening nature of the response with the peak deflection/voltage amplitude occurring at a frequency value lower than the resonant frequency.

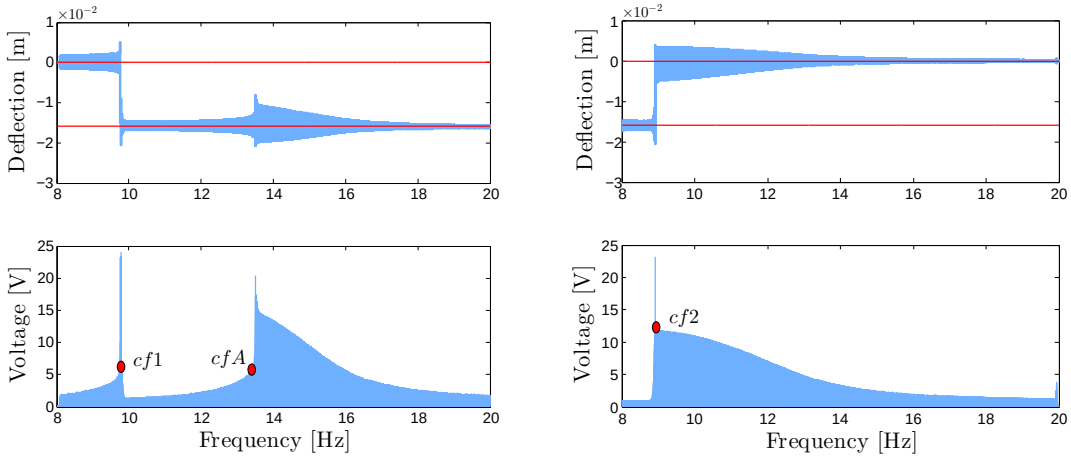

Figure 5.14: Experimental frequency-response curves for a base excitation of 2 m/s^2 with zero initial displacement: (a) forward sweep, and (b) reverse sweep. The solid horizontal (red) lines represent the stable equilibria.

Similar behavior is observed with the forward and reverse frequency sweeps when the initial position of the harvester is set to the non-trivial equilibrium, x_{s3}, for the same base acceleration (2 m/s^2) as seen in Fig. 5.15. In this scenario, the oscillations remain confined to the outer potential well for the entire range of frequencies and cannot overcome the potential barrier owing to the low base excitation level. A similar bend in the frequency-response curves is observed with the jump from the intra-well resonant branch to the small-amplitude non-resonant branch occurring at a smaller value of the excitation frequency $\approx$ 10 Hz as seen in Fig. 5.15(b). The frequency response curves also capture the asymmetric nature of oscillations within the outer potential well with larger deflections occuring on one side of the static equilibrium. These experimental trends emphasize the fact that, at low base excitation levels, the harvester exhibits small-amplitude intra-well periodic responses within the middle or the outer potential well depending on the direction of frequency sweep and initial conditions. This qualitative behavior agrees well with our theoretical analysis from

Fig. 5.2(a) in Section 5.2. Furthermore, it is worth mentioning that the jump phenomena observed experimentally correspond to the cyclic fold bifurcations highlighted in Section 5.2.

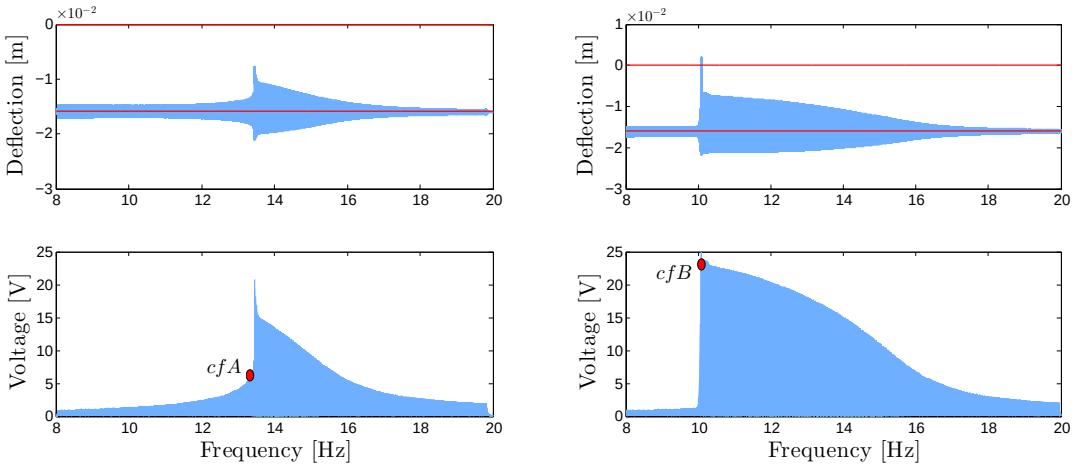

Figure 5.15: Experimental frequency-response curves for a base excitation of 2 m/s^2 with a nonzero static initial displacment: (a) forward sweep, and (b) reverse sweep. The solid horizontal (red) lines represent the stable equilibria.

As shown in Fig. 5.16(a), when the amplitude of input acceleration is increased to 6 m/s^2, a forward frequency sweep now excites the periodic large-amplitude inter-well oscillations in the lower end of the frequency range considered (6.2 - 10 Hz). These large-amplitude oscillations produce large output voltages with the peak value reaching close to a 100V. As the frequency is increased, this large-amplitude branch of oscillations ceases to exist and gives way to the small-amplitude intra-well branch of periodic oscillations around the non-trivial equilibrium $x_{s2} = 0.0167$ m. As seen in Fig. 5.16(a), further increase in the excitation frequency, results in a window of intra- and inter-well chaotic responses causing an increase in the output voltage (between 13 and 14 Hz). These chaotic responses quickly disappear to giving way to the intra-well oscillations around the trivial equilibrium.

In the reverse sweep shown in Fig. 5.16(b), we observe that the region over which the large-amplitude inter-well oscillations are activated is much smaller (between 6 and 7 Hz) and the oscillations are mostly confined to either the middle or outer potential well. This experimental behavior is in qualitative agreement with our theoretical observations depicted in Fig. 5.2(b) where

it was shown that the desired large-amplitude branch of periodic solutions coexist with the small-amplitude branches. The trend observed reiterates that, although higher base accelerations can activate the desirable large-amplitude inter-well responses, they cannot be uniquely realized over a wide range of frequencies.

When the harvester is subjected to the same base acceleration level with a non-trivial initial displacement, the response of the harvester remains generally the same in the forward and reverse sweeps as shown in Fig. 5.17. The only notable difference is shown in Fig. 5.17(b) for the reverse sweep. Specifically, the amplitude of deflection and thereby the output voltage is larger in the higher end of the frequency range (12-16 Hz) due to the harvester performing intra-well oscillations on the resonant branch associated with the outer potential well.

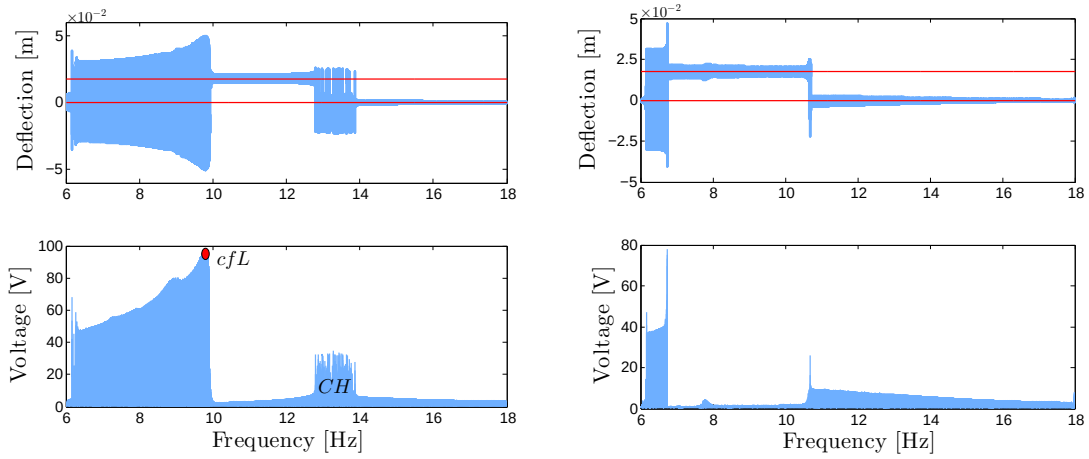

Figure 5.16: Experimental frequency-response curves for a base excitation of 6 m/s^2 with zero initial displacement: (a) forward sweep, and (b) reverse sweep. The solid horizontal (red) lines represent the stable equilibria.

When the base acceleration amplitude is increased to 8 m/s^2 and the initial displacement is zero, the forward frequency sweep illustrates an increase in the amplitude of the deflection and output voltage resulting from the large-amplitude periodic oscillations. The peak voltage exceeds 100 V near an excitation frequency of 10 Hz (see Fig. 5.18(a)). We also observe that, there is no significant increase in the range of frequencies over which the large-amplitude oscillations extend as compared to the case when the base acceleration is 6 m/s^2. However, one notable difference, as

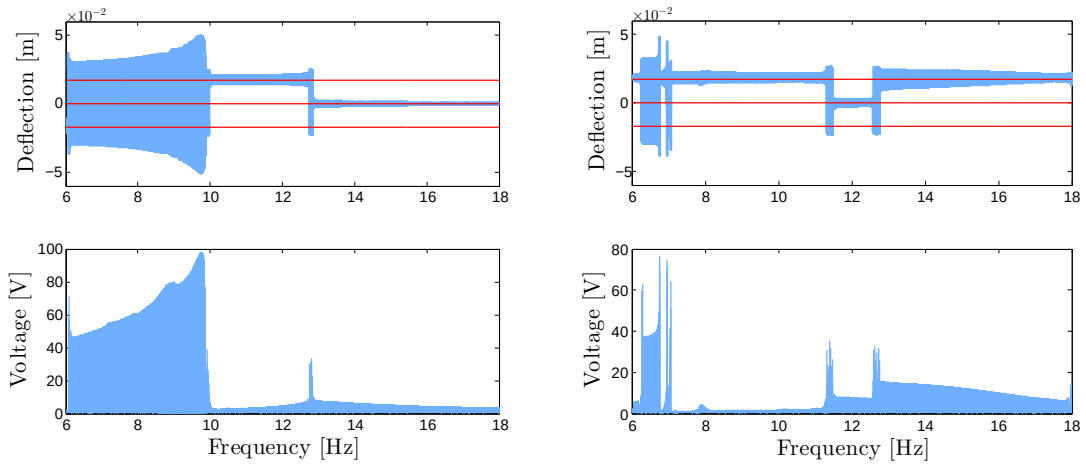

Figure 5.17: Experimental frequency-response curves for a base excitation of 6 m/s^2 with a nonzero static initial displacment: (a) forward sweep, and (b) reverse sweep. The solid horizontal (red) lines represent the stable equilibria.

shown in Fig. 5.18(b) is that, for the reverse sweep, the inter-well branch of oscillations exists over a wider range of frequencies (6-8 Hz). Again, this experimental behavior corroborates our theoretical findings which indicated that, as the forcing level is increased, the less desirable small-amplitude intra-well branch of solutions exist over a smaller range of frequencies.

As seen in Fig. 5.19, no notable differences in the response are observed when the initial condition is shifted to coincide with the non-trivial static equilibrium. The only exception is that the intra- and inter-well chaotic oscillations extend over a slightly larger frequency range as shown in Fig. 5.19(a) and 5.19(b).

The experimental results presented in this section capture the complex dynamic (periodic and aperiodic) responses associated with a tri-stable VEH. It is shown that, tri-stable VEHs can produce large output voltages owing to the excitation of the inter-well oscillations but they are sensitive to the direction of frequency sweeps and initial conditions. This poses a challenge in efficiently designing these devices such that they can produce the desired large output voltages uniquely over a broadband frequency range when subjected to harmonic base excitations. Consequently, this necessitates the theoretical (numerical and analytical) analysis presented in this work to obtain a better qualitative understanding of their response for a given set of design parameters.

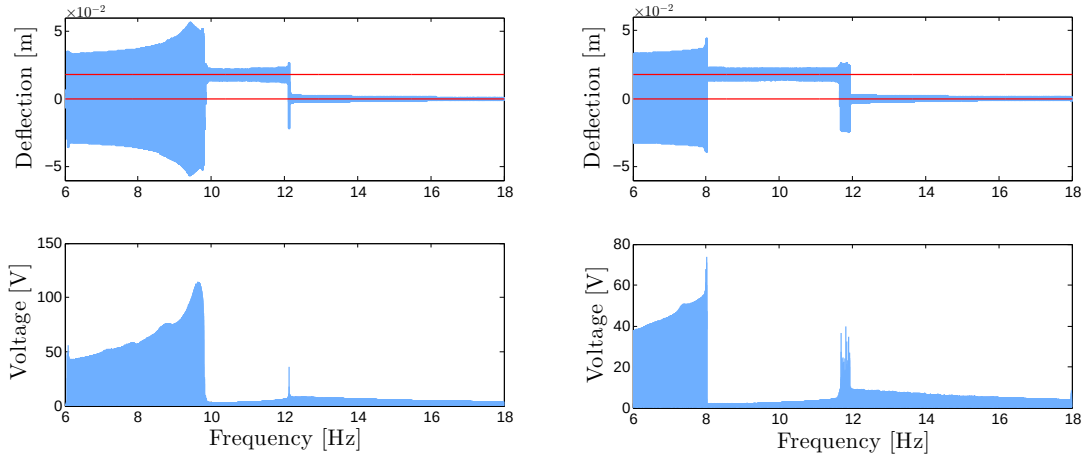

Figure 5.18: Experimental frequency-response curves for a base excitation of 8 m/s^2 with zero initial displacement: (a) forward sweep, and (b) reverse sweep. The solid horizontal (red) lines represent the stable equilibria.

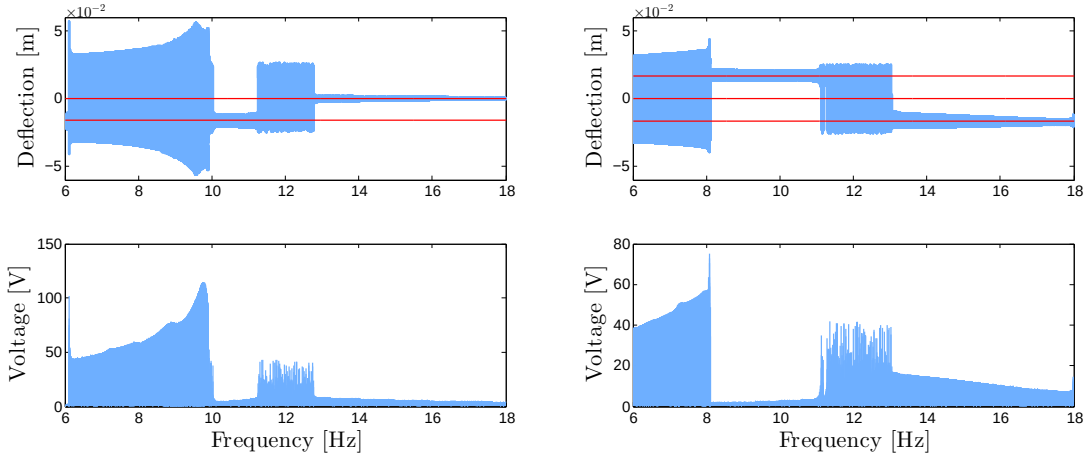

Figure 5.19: Experimental frequency-response curves for a base excitation of 8 m/s^2 with a nonzero static initial displacment: (a) forward sweep, and (b) reverse sweep. The solid horizontal (red) lines represent the stable equilibria.

Chapter 6

Discussions and Conclusions

This chapter presents the main conclusions for this dissertation and briefly discusses potential future research. In general, the research presented in this dissertation is focused on developing an analytical framework to better understand the influence of nonlinearities on the performance and particularly, the effective bandwidth of nonlinear VEHs under harmonic excitations. Towards achieving the dissertation objectives, three categories of nonlinear VEHs are considered namely, the mono-, bi- and tri-stable. In the first part of the dissertation, analytical solutions approximating the response characteristics and the bandwidth of bi-stable VEHs are developed. In the next part, the analysis is extended to compare the performance of mono- and bi-stable harvesters under optimal electric loading conditions. In the final part of this work, the dynamic responses of tri-stable VEHs under harmonic inputs are studied through a numerical, analytical, and experimental investigation and a framework for defining the effective bandwidth of these devices is discussed. The following sections summarize the tasks accomplished and conclusions drawn from each case.

6.1 Effective Bandwidth of Bi-stable Harvesters

For this task, we used analytical techniques to predict the oscillatory response characteristics of bi-stable VEHs that possess a symmetric quartic potential function. A canonical model describing the dynamics of a typical bi-stable VEH which consists of a mechanical oscillator coupled to an electric circuit was considered. Using the method of multiple scales, analytical solutions characterizing the steady-state intra- and inter-well vibratory responses of the harvester were obtained.

These solutions were utilized to identify the critical bifurcations in the parameter's space. The loci of these bifurcations were used to define an effective frequency bandwidth over which it is possible to obtain oscillations desirable for energy harvesting. The influence of three critical design parameters, namely, the time constant ratio, the electromechanical coupling, and the potential shape on the effective bandwidth were analyzed and the following observations were made:

- Although numerical analyses suggest that the effective frequency bandwidth can be increased by simply increasing the amplitude of excitation, the analytical methods adopted in this work elucidate that the design parameters play a significant role in defining the effective bandwidth of bi-stable VEHs.

- Varying the time constant ratio (ratio between the period of the mechanical system and the time constant of the harvesting circuit) has very little influence on the effective bandwidth, but influences the amplitude of the electric response of a bi-stable VEH.

- The electromechanical coupling plays a significant role in defining the effective bandwidth of a bi-stable harvester as it directly influences the electric damping in the system. As such, increasing the electromechanical coupling results in the narrowing of the effective frequency bandwidth of the harvester.

- Decreasing the depth of the potential wells associated with a bi-stable VEH, increases the effective frequency bandwidth and decreases the excitation level necessary to activate oscillations desirable for energy harvesting. Nevertheless, the associated electric output responses are generally small in amplitude. On the other hand, increasing the depth of the potential wells serves to shrink the effective frequency bandwidth, but it is accompanied by an increase in the electric output of the harvester.

With these observations, it is possible to conclude that an appropriate choice of parameters, specifically the potential shape and the electromechanical coupling along with the forcing level are essential towards optimizing the design and enhancing performance of bi-stable VEHs.

6.2 Comparative Performance Analysis of Electrically-Optimized Mono- and Bi-stable Energy Harvesters

In this chapter, we compared the optimal power output of mono- and bi-stable energy harvesters subjected to harmonic excitations of similar magnitudes and frequencies. A canonical model of a VEH which can operate in both of the mono- and bi-stable configurations was considered. Analytical expressions characterizing the steady-state output power associated with the global and the local periodic responses of the VEH were obtained. These solutions were then used to optimize the output power with respect to the time constant ratio (ratio between the period of the mechanical system and the time constant of the harvesting circuit) which represents a measure of the electric load. The resulting expressions were used to obtain the optimal output power in both configurations for different potential shapes and excitation levels resulting in the following observations:

- When the harvester is tuned such that the natural frequency is relatively low, the bi-stable configuration outperforms the mono-stable one over most of the frequency range under optimal electric loading conditions. In this scenario, the bi-stable configuration possesses relatively shallow potential wells which permits the activation of the large-amplitude inter-well responses at relatively lower forcing levels, thereby resulting in larger output power. Although the enhancement is more pronounced in the lower end of the frequency range, it can be extended to the region of primary resonance (tuned-frequency) with sufficient forcing levels.

- When the harvester is tuned such that it has a relatively higher natural frequency, the bi-stable configuration again exhibits higher output power when compared to the mono-stable one over most of the frequency range. However, another branch of solution which results in small power levels always accompanies the desired higher power branch. This highlights the dependence of the bi-stable harvester response on the initial conditions. Similar trends are observed as the natural frequency is increased further.

- The optimal time constant ratio associated with the large-amplitude power in both of the mono- and bi-stable configurations varies linearly with the excitation frequency and is close to the value of the frequency itself.

With these observations, it is possible to conclude that the relative magnitude of output power in mono- and bi-stable harvesters exhibits complex dependence on the shape of the potential

function, level of excitation, and the value of electric load. Bi-stable harvesters produce higher power levels under their optimal loading conditions for all shapes of the potential functions considered. Even when the excitation levels are not very high, as long as an optimal electric load is chosen, it is possible to design a bi-stable harvester with shallow enough potential wells to produce higher power levels as compared to a mono-stable one albeit at lower frequencies.

6.3 Investigation of a Tri-stable Nonlinear Oscillator for Energy Harvesting Under Harmonic Excitations

In this chapter, we considered a lumped-parameter electromechanical model of a tri-stable VEH which includes a restoring force with cubic and quintic nonlinearities. An initial numerical investigation of the harvester response to harmonic quasi-statically varied frequency excitations revealed complex dynamic responses including large-amplitude (inter-well), small-amplitude (intra-well) and aperiodic responses. The numerical analysis also served to help identify key bifurcations that govern the loss of stability of the various branches of periodic solutions. Again, using the method of multiple scales, analytical expressions for the steady-state periodic deflections and electric quantities associated with the intra- and inter-well oscillations of the harvester were derived. These expressions were utilized to obtain approximations for the loci of the various bifurcations in the force-frequency parameter space. The loci of these bifurcations were then used to construct a map which outlines the regions of qualitatively different responses in the parameters' space, thereby providing a rough estimate of the effective frequency bandwidth of tri-stable VEHs. The influence of the time constant ratio and electromechanical coupling on the bandwidth of the harvester are studied. An experimental case study is carried out and the following observations were made:

- Similar to their bi-stable counterparts, tri-stable VEHs perform large-amplitude inter-well oscillations at low-frequencies making them a viable option for harvesting energy from low frequency excitations, especially when the nature of excitation is known.

- Owing to the presence of three potential wells, it can be surmised that there is an improvement in the response bandwidth of tri-stable VEHs as compared to bi-stable ones, even when the excitation amplitude is not large enough to initiate large-amplitude inter-well oscillations. This can be attributed to the fact that the harvester has two resonant frequencies: one around the

trivial equilibrium and the second, around the static equilibrium. Consequently, the harvester can perform resonant oscillations when the excitation frequency is close to either of these local oscillation frequencies, thereby producing large electric outputs over a wider range of frequencies. An experimental investigation reinforced this hypothesis by clearly showing that resonant intra-well oscillations can be realized over a wider range of frequencies.

- Similar to the trends observed in bi-stable VEHs, the time constant ratio (ratio between the period of the mechanical system and the time constant of the harvesting circuit) has negligible influence on the effective bandwidth of tri-stable VEHs. However, it significantly influences the amplitude of the electric responses.

- Increasing the electromechanical coupling results in the shrinking of the effective frequency bandwidth of a tri-stable VEH. This can be attributed to an increase in the electric damping in the system due to increased energy dissipation.

  With these observations, it can be concluded that tri-stable VEHs can provide improvement in bandwidth over bi-stable counterparts. However, the analysis in this study reiterates the fact that a careful choice of parameters is essential towards designing efficient tri-stable VEHs that can provide significant improvements in bandwidth.

6.4 Directions for future research

The research in this dissertation focused on the importance of using analytical tools towards understanding the influence of nonlinearities and design parameters on the effective frequency bandwidth of nonlinear VEHs namely mono-, bi- and tri-stable ones when subjected to harmonic inputs. It was established that, bi-stable and tri-stable VEHs exhibit similar qualitative performance enhancement characteristics since both of these harvesters can produce large electric responses at low frequencies. Nevertheless, tri-stable VEHs exhibit additional complexities which make it difficult to fully characterize their benefits. For instance, bi-stable harvesters have potential wells, the shape of which can be altered by simply changing the linear stiffness coefficient. Tri-stable VEHs, on the other hand, have three potential wells whose shape depends on a combination of the linear and nonlinear stiffness coefficients. Hence, investigating the relative performance of these two classes of nonlinear VEHS presents an interesting topic for future research. This can be achieved by comparing the

output power of both harvesters under optimal electric loading conditions similar to the comparison performed in this dissertation between mono- and bi-stable harvesters. The work can be extended to a comprehensive relative performance study which compares all three classes of nonlinear VEHs under similar loading conditions.

Throughout this research, we established an analytical framework to delineate the combination of design parameters that would not only result in large electric outputs but also improve the bandwidth of three types of nonlinear VEHs subjected to fixed-frequency excitations. The results presented can be used as effective guidelines in the efficient design of these VEHs, especially when the nature of excitation is known to be harmonic. Unfortunately, most ambient sources of excitation have time-varying frequency characteristics or are random in nature. Although several studies have been directed towards studying the response characteristics of mono- and bi-stable VEHs under random inputs, characterizing responses of tri-stable VEHs subject to random excitations represents an interesting topic of future research.

Most of the previous research efforts, including ours, have mainly focused characterizing performance of VEHS that incorporate nonlinearities in the mechanical subsystem while using simple linear circuit models. Incorporating nonlinear energy harvesting circuits that resonate internally with the mechanical subsystem might provide effective mechanisms for broadband and improved transduction. Such concepts have been effectively utilized for vibration absorption and might be adapted to vibratory energy harvesting [75]. Inclusion of more complex conditioning circuits that involve nonlinear circuit elements and battery models could provide new insights into the design of VEHs. This might permit reaping the full benefits of the nonlinearities.

Bibliography

[1] D.A.W. Barton, S.G. Burrow, and L.R. Clare. Energy Harvesting From Vibrations with a Nonlinear Oscillator. *ASME Journal of Vibration and Acoustics*, 132(2), 2010.

[2] B.P. Mann and N. D. Sims. Energy Harvesting from The Nonlinear Oscillations of Magnetic Levitation. *Journal of Sound and Vibration*, 319:515–530, 2008.

[3] A. Erturk, J. Hoffmann, and D. J. Inman. A Piezomagnetoelastic Structure for Broadband Vibration Energy Harvesting. *Applied Physics Letters*, 94(25):254102, 2009.

[4] C. McInnes, D. Gorman, and M. Cartmell. Enhanced Vibrational Energy Harvesting Using Nonlinear Stochastic Resonance. *Journal of Sound and Vibration*, 318:655–662, 2008.

[5] S. C. Stanton, C. C. McGehee, and B. P. Mann. Nonlinear Dynamics for Broadband Energy Harvesting: Investigation of a Bistable Piezoelectric Inertial Generator. *Physica D: Nonlinear Phenomena*, 239:640–653, 2010.

[6] R. Masana and M. F. Daqaq. Electromechanical Modeling and Nonlinear Analysis of Axially Loaded Energy Harvesters. *Journal of Vibration and Acoustics*, 133(1):011007, 2011.

[7] R. Masana and M. F. Daqaq. Relative Performance of a Vibratory Energy Harvester in Mono- and Bi-stable Potentials. *Journal of Sound and Vibration*, 330(24):6036 – 6052, 2011.

[8] S. Zhou, J. Cao, D.J. Inman, J. Lin, S. Liu, and Z. Wang. Broadband Tristable Energy Harvester: Modeling and Experiment Verification. *Applied Energy*, 133(0):33 – 39, 2014.

[9] A. J. duPlessis, M. J. Huigsloot, and F. D. Discenzo. Resonant Packaged Piezoelectric Power Harvester for Machinery Health Monitoring. In *Proceedings of Smart Structures and Materials Conference, SPIE*, page 5762, San Diego, CA, 2005.

[10] D. J. Inman and B. L. Grisso. Towards Autonomous Sensing. In *Proceedings of Smart Structures and Materials Conference, SPIE*, page 61740T, San Diego, CA, 2006.

[11] R. S. Sanders and M. T. Lee. Implantable Pacemakers. *Proceedings of the IEEE*, 84(3), 1995.

[12] I. D. Capel, H. M. Dorrell, E. P. Spencer, and M. W. Davis. The Amelioration of the Suffering Associated with Spinal Cord Injury with Subperception Transcranial Electrical Stimulation. *Spinal Cord*, 41:109–117, 2003.

[13] G. Renzenbrink and M. J Jzerman. Percutaneous Neuromuscular Electrical Stimulation for Treating Shoulder Pain in Chronic Hemiplegia. Effects on Shoulder Pain and Quality of Life. *Clinical Rehabilitation*, 18:359–365, 2004.

[14] S. Roundy, P. K. Wright, and J. Rabaey. A Study of Low Level Vibrations as a Power Source for Wireless Sensor Nodes. *Computer Communciations*, 26:1131–1144, 2003.

[15] S. Roundy and P. K. Wright. A Piezoelectric Vibration-Based Generator for Wireless Electronics. *Journal of Intelligent Materials and Structures*, 16:809–823, 2005.

[16] S. W. Arms, C. P. Townsend, D. L. Churchill, G. H. Galbreath, and S. W. Mundell. Power Management for Energy Harvesting Wireless Sensors. In *Proceedings of the Smart Structures and Materials Conference, SPIE*, pages 5763 267–75, San Diego, CA, 2005.

[17] S. P. Gurav, A. Kasyap, M. Sheplak, L. Cattafesta, R. T. Haftka, J. F. L. Goosen, and F. Van Keulen. Uncertainty-based Design Optimization of a Micro Piezoelectric Composite Energy Reclamtation Device. In *Proceedings of the 10th AIAA/ISSSMO Multidisciplinary Analysis and Optimization Conference*, pages 3559–70, 2004.

[18] W. Zhou, W. H. Liao, and W. J. Li. Analysis and Design of a Self-powered Piezoelectric Microaccelerometer. In *Proceedings of the Smart Structures and Materials Conference, SPIE*, pages 5763 233–240, San Diego, CA, 2005.

[19] G. Asada, M. Dong, T. S. Lin, F. Newberg, G. Pottie, W.J. Kaiser, and H.O. Marcy. Wireless Integrated Network Sensors: Low Power Systems on a Chip. In *Solid-State Circuits Conference, 1998. ESSCIRC '98. Proceedings of the 24th European*, pages 9–16, Sept 1998.

[20] J. W. Kim, H. Takao, K. Sawada, and M. Ishida. Integrated Inductors for RF Transmitters in CMOS/MEMS Smart Microsensor Systems. *Sensors 7*, pages 1387–1398, 2007.

[21] S. Gregori, Y. Li, H. Li, J. Liu, and F. Maloberti. 2.45 GHz Power and Data Transmission for a Low-Power Autonomous Sensors Platform. In *International Symposium on Low Power Electronics and Design, ISLPED 04*, pages 269–273, 2004.

[22] J. A. Paradiso and Starner T. Energy Scavenging for Mobile and Wireless Electronics. *IEEE Pervasive Computing*, 4:18–27, 2005.

[23] X. Jiang, J. Polastre, and D. E. Culler. Perpetual Environmentally Powered Sensor Networks. In *Information Processing in Sensor Networks, IPSN 2005*, pages 463–468, 2005.

[24] N. Joachim. Thermoelectric Thin Film Power Generators - Self-sustaining power supply for smart systems. In *Proceedings of the SPIE - The International Society for Optical Engineering,Smart Sensors, Actuators, and MEMS IV*, 2009.

[25] S. Saggini and P. Mattavelli. Power management in Multi-source Multi-load Energy Harvesting Systems. In *Power Electronics and Applications, 2009. EPE '09. 13th European Conference on*, pages 1 –10, sept. 2009.

[26] A. Hande, P. Shah, J. N. Falasco, and D. Weiner. Autonomous Energy Harvesting Embedded Sensors for Border Security Applications. In *SPIE - The International Society for Optical Engineering*, volume 7666, pages 24–35, 2010.

[27] S. Roundy. On the Effectiveness of Vibration-based Energy Harvesting. *Journal of Intelligent Materials and Structures*, 16:809–823, 2005.

[28] H. Sodano, D. J. Inman, and G.Park. A Review of Power Harvesting from Vibration Using Piezoelectric Materials. *The Shock and Vibration Digest*, 36:197–205, 2004.

[29] H. Sodano, D. J. Inman, and G.Park. Generation and Storage of Electricity from Power Harvesting Devices. *Journal of Intelligent Material Systems and Structures*, 16:67–75, 2005.

[30] N. Elvin, N. Lajnef, and A. Elvin. Feasibility of Structural Monitoring with Vibration Powered Sensors. *Smart Materials and Structures*, 15:977–986, 2006.

[31] T. Galchev, J. McCullagh, R. L. Peterson, and K. Najafi. Harvesting Traffic-Induced Bridge Vibrations. In *International Solid-State Sensors, Actuators and Microsystems*, pages 1661–1664, 2011.

[32] G. De Pasquale, A. Som, and F. Fraccarollo. Piezoelectric Energy Harvesting for Autonomous Sensors Network on Safety-Improved Railway Vehicles. *Proceedings of the Institution of Mechanical Engineers, Part C: Journal of Mechanical Engineering Science*, 226(4):1107–1117, 2012.

[33] G. De Pasquale, A. Somà, and N. Zampieri. Design, Simulation, and Testing of Energy Harvesters with Magnetic Suspensions for the Generation of Electricity from Freight Train Vibrations. *Journal of Computational and Nonlinear Dynamics*, 7(4):041011, 2012.

[34] S. Roundy and Y. Zhang. Toward Self-Tuning Adaptive Vibration-Based Micro-Generators. In *Smart Materials, Nano- and Micro-Smart Systems*, Sydney, Australia, 2005.

[35] W. Wu, Y. Chen, B. Lee, J. He, and Y. Peng. Tunable Resonant Frequency Power Harvesting Devices. In *Proceedings of Smart Structures and Materials Conference, SPIE*, page 61690A, San Diego, CA, 2006.

[36] V. Challa, M. Prasad, Y. Shi, and F. Fisher. A Vibration Energy Harvesting Device with Bidirectional Resonance Frequency Tunability. *Smart Materials and Structures*, 75:1–10, 2008.

[37] S. M. Shahruz. Design of Mechanical Band-Pass Filters for Energy Scavenging. *Journal of Sound and Vibrations*, 292:987–998, 2006.

[38] S. C. Stanton, C. C. McGehee, and B. P. Mann. Reversible Hysteresis for Broadband Magnetopiezoelastic Energy Harvesting. *Applied Physics Letters*, 95:174103, 2009.

[39] M. F. Daqaq. Response of Uni-Modal Duffing Type Harvesters to Random Forced Excitations. *Journal of Sound and Vibration*, 329:3621–3631, 2010.

[40] F. Cottone, H. Vocca, and L. Gammaitoni. Nonlinear Energy Harvesting. *Physical Review Letters*, 102:080601, 2009.

[41] B. P. Mann and B. A. M. Owens. Investigations of A Nonlinear Energy Harvester with A Bistable Potential Well. *Journal of Sound and Vibration*, 329:1215–1226, 2010.

[42] M. F. Daqaq. Transduction of a Bistable Inductive Generator Driven By White and Exponentially Correlated Gaussian Noise. *Journal of Sound and Vibration*, 330(11):2554 – 2564, 2011.

[43] A.F. Arrieta, P. Hagedorn, A. Erturk, and D.J. Inman. A Piezoelectric Bistable Plate for Nonlinear Broadband Energy Harvesting. *Applied Physics Letters*, 97(10):104102, 2010.

[44] M. Ferrari, V. Ferrari, M. Guizzetti, B. And, S. Baglio, and C. Trigona. Improved Energy Harvesting from Wideband Vibrations by Nonlinear Piezoelectric Converters. *Sensors and Actuators A: Physical*, 162(2):425 – 431, 2010.

[45] M. Ferrari, M. Baù, M. Guizzetti, and V. Ferrari. A Single-Magnet Nonlinear Piezoelectric Converter for Enhanced Energy Harvesting from Random Vibrations. *Sensors and Actuators A: Physical*, 172(1):287 – 292, 2011.

[46] G. Litak, M. I. Friswell, and S. Adhikari. Magnetopiezoelastic Energy Harvesting Driven by Random Excitations. *Applied Physics Letters*, 96(21):214103, 2010.

[47] J. Lin, B. Lee, and B. Alphenaar. The Magnetic Coupling of a Piezoelectric Cantilever for Enhanced Energy Harvesting Efficiency. *Smart Materials and Structures*, 19(4):045012.

[48] R. Masana and M. F. Daqaq. Energy Harvesting in the Super-harmonic Frequency Region of a Twin-well Oscillator. *Journal of Applied Physics*, 111(4):044501, 2012.

[49] A. Cammarano, S. G. Burrow, and D. A. W. Barton. Modelling and Experimental Characterization of an Energy harvester with Bi-stable Compliance Characteristics. *Proceedings of the Institution of Mechanical Engineers, Part I: Journal of Systems and Control Engineering*, 225(4):475–484, 2011.

[50] L. Gammaitoni, I. Neri, and H. Vocca. Nonlinear Oscillators for Vibration Energy Harvesting. *Applied Physics Letters*, 94(16):164102, 2009.

[51] A. M. Wickenheiser and E. Garcia. Broadband Vibration-based Energy Harvesting Improvement Through Frequency Up-conversion by Magnetic Excitation. *Smart Materials and Structures*, 19(6):065020, 2010.

[52] F. C. Moon and P. J. Holmes. A Magnetoelastic Strange Attractor. *Journal of Sound and Vibration*, 65:275–296, 1979.

[53] S. Zhou, J. Cao, J. Lin, and Z. Wang. Exploitation of a Tristable Nonlinear Oscillator for Improving Broadband Vibration Energy Harvesting. *The European Physical Journal Applied Physics*, 67(30902), 2014.

[54] M.F. Daqaq, R. Masana, A. Erturk, and D. D. Quinn. On the Role of Nonlinearities in Vibratory Energy Harvesting: A Critical Review and Discussion. *Applied Mechanics Reviews*, 66(4):040801, 2014.

[55] A. Erturk and D.J. Inman. Broadband Piezoelectric Power Generation on High-energy Orbits of the Bistable Duffing Oscillator with Electromechanical Coupling. *Journal of Sound and Vibration*, 330(10):2339 – 2353, 2011.

[56] W. Szemplińska-Stupnicka and J. Rudowski. Local Methods in Predicting Occurrence of Chaos in Two-Well Potential Systems: Superharmonic Frequency Region. *Journal of Sound and Vibration*, 152(57-72), 1992.

[57] W. Szemplińska-Stupnicka and J. Rudowski. Steady States in the Twin-Well Potential Oscillator: Computer Simulations and Approximate Analytical Studies. *Chaos: An Interdisciplinary Journal of Nonlinear Science*, 3(3), 1993.

[58] W. Szemplińska-Stupnicka and J. Rudowski. Bifurcations Phenomena in a Nonlinear Oscillator: Approximate Analytical Studies Versus Computer Simulation Results. *Physica D: Nonlinear Phenomena*, 66(34):368 – 380, 1993.

[59] W. Szemplińska-Stupnicka. The Analytical Predictive Criteria for Chaos and Escape in Nonlinear Oscillators: A Survey. *Nonlinear Dynamics*, 7(2):129–147, 1995.

[60] S. C. Stanton, B. A. M. Owens, and B. P. Mann. Harmonic Balance Analysis of the Bistable Piezoelectric Inertial Generator. *Journal of Sound and Vibration*, 331(15):3617–3627, 2012.

[61] S. C. Stanton, B. P. Mann, and B. A. M. Owens. Melnikov Theoretic Methods for Characterizing the Dynamics of the Bistable Piezoelectric Inertial Generator in Complex Spectral Environments. *Physica D: Nonlinear Phenomena*, 241(6):711–720, 2012.

[62] R. L. Harne, M. Thota, and K. W. Wang. Concise and High-fidelity Predictive Criteria for Maximizing Performance and Robustness of Bistable Energy Harvesters. *Applied Physics Letters*, 102(5):053903, 2013.

[63] R. L. Harne and K. W. Wang. On the Fundamental and Superharmonic Effects in Bistable Energy Harvesting. *Journal of Intelligent Material Systems and Structures*, 2013.

[64] Y. C. Shu and I. C. Lien. Analysis of Power Output for Piezoelectric Energy Harvesting Systems. *Smart Materials and Structures*, 15(6):1499, 2006.

[65] Y. Liao and H. A. Sodano. Model of a Single Mode Energy Harvester and Properties for Optimal Power Generation. *Smart Materials and Structures*, 17(6):065026, 2008.

[66] J. M. Renno, M. F. Daqaq, and D. J. Inman. On the Optimal Energy Harvesting from a Vibration Source. *Journal of Sound and Vibration*.

[67] A. M. Wickenheiser and E. Garcia. Power Optimization of Vibration Energy Harvesters Utilizing Passive and Active Circuits. *Journal of Intelligent Material Systems and Structures*, 21(13):1343–1361, 2010.

[68] M. W. Shafer, M. Bryant, and E. Garcia. Designing Maximum Power Output into Piezoelectric Energy Harvesters. *Smart Materials and Structures*, 21(8):085008, 2012.

[69] A. Erturk and D. Inman. A Distributed Parameter Electromechanical Model for Cantilevered Piezoelectric Energy Harvesters. *Journal of Vibration and Acoustics, Transaction of ASME*, 130:1–14, 2008.

[70] A. H. Nayfeh and D. T. Mook. *Nonlinear Oscillations*. Wiley-Interscience, New York, 1979.

[71] C. Hayashi. *Nonlinear Oscillations in Physical Systems*. McGraw Hill, 1964.

[72] J. Cao, S. Zhou, W. Wang, and J. Lin. Influence of the Potential Well Depth on Nonlinear Tristable Energy Harvesting. *Applied Physics Letters*, 106(173903), 2015.

[73] M. Panyam, R. Masana, and M. F. Daqaq. On Approximating the Effective Bandwidth of Bi-stable Energy Harvesters. *International Journal of Non-Linear Mechanics*, 67(0):153–163, 2014.

[74] A. H. Nayfeh and A. A. Khdeir. Nonlinear Rolling of Ships in Regular Beam Seas. *International Shipbuilding Progress*, 33:40 – 49, 1986.

[75] S. S. Oueini, C. Chin, and A. H. Nayfeh. Dynamics of a Cubic Nonlinear Vibration Absorber. *Nonlinear Dynamics*, 20(3):283 – 295, 1999.